

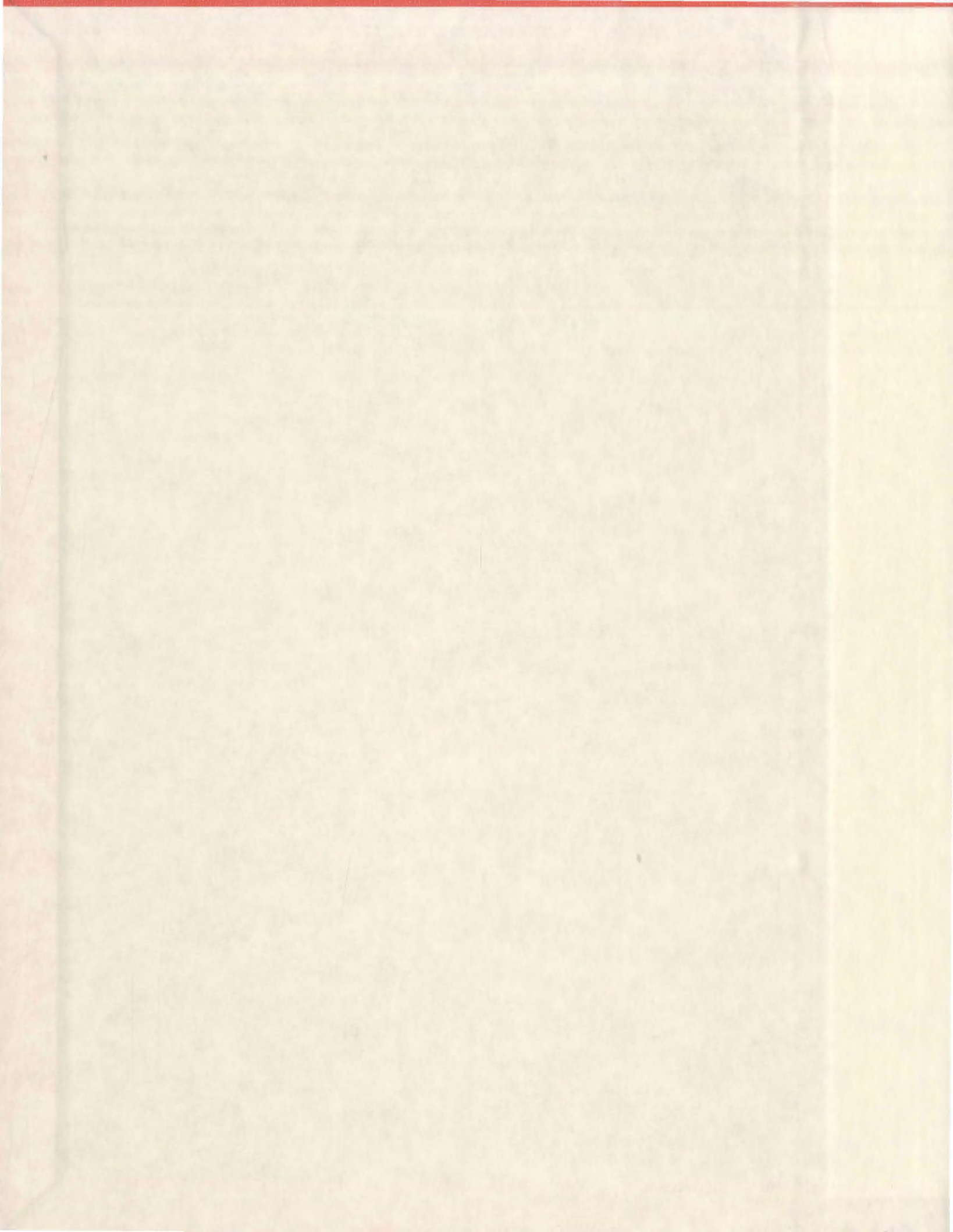
EVALUATION OF THE CORROSION PERFORMANCE
OF 316 L STAINLESS STEEL FOR HYDROMETALLURGICAL
PROCESSING OF VOISEY'S BAY NICKEL CONCENTRATE

CENTRE FOR NEWFOUNDLAND STUDIES

**TOTAL OF 10 PAGES ONLY
MAY BE XEROXED**

(Without Author's Permission)

GERALD P. SNOW



EVALUATION OF THE TENSILE PROPERTIES
OF 304 STAINLESS STEEL FOR A DESIGNER'S GUIDE
IN THE DESIGN OF VEHICLE BODY COMPONENTS

C. Gerald Soper, B. Eng.

A thesis submitted to the
Faculty of Graduate Studies
in partial fulfillment of the
requirements for the degree of
Master of Engineering

School of Engineering and Applied Science
Victoria University of Wellington

August 1987



New Zealand

EVALUATION OF THE CORROSION PERFORMANCE
OF 316 L STAINLESS STEEL FOR HYDROMETALLURGICAL
PROCESSING OF VOISEY'S BAY NICKEL CONCENTRATE

by

© Gerald P. Snow, B. Eng.

A thesis submitted to the
School of Graduate Studies
in partial fulfillment of the
requirements for the degree of
Master of Engineering

Faculty of Engineering and Applied Science
Memorial University of Newfoundland

August 2005

St. Johns



Newfoundland

ABSTRACT

The susceptibility of 316 L stainless steel to pitting corrosion in a solutions of sulfuric acid has been investigated using both potentiodynamic and potentiostatic polarization techniques. The effects of Cl^- , SO_4^{2-} , Ni^{2+} , Fe^{3+} and aeration were studied and the results are presented in terms of pitting potential, free corrosion potential and pit morphology.

It was determined that the potentiostatic polarization techniques resulted in pitting potentials closer to the true pitting potential when compared to values obtained using potentiodynamic polarization. Validation of the pitting potential was done by comparing the data from the respective polarization tests to the surface of the test sample in question. Solutions containing chloride ions resulted in the lowest pitting potentials and highest amount of anodic dissolution. It was found that etch pits developed at lower potentials closer to the pitting potential, whereas polished pits developed at higher potentials.

A scanning electron microscope (SEM) was used to analyze micro-pits on the surface of the polarized samples. From the analysis it was clear that pits developed with a cover which served as a diffusion barrier promoting stable pit growth. A profile of stable pits were examined by cross sectioning the polarized samples and it was concluded that the morphology of developed pits are not hemispherical in shape but rather saucer shaped with an average width-to-depth ratio of about 6.

Key Words: pitting potential, free corrosion potential, pit, sulfuric acid, nickel chloride, nickel sulfide, ferric sulfide, oxygen, argon, potentiodynamic, potentiostatic, austenitic stainless steel

ACKNOWLEDGEMENTS

This thesis was completed at the Faculty of Engineering and Applied Science, Memorial University of Newfoundland. Funding for the research was provided by

A special thank you to Dr. John Shirokoff, who acted as supervisor and to Dr. John Molgaard who acted as co-supervisor for the project for providing invaluable advice and guidance throughout the study.

Many thanks to Tom Pike, Sheldon Mercer and Bernie Healy for their technical support and helpful suggestions throughout the project. I would also like to thank Michael Shaffer for his assistance with using the scanning electron microscope as well as Technical Services for their work in machining test samples.

NOMENCLATURE

Cl⁻ - Chloride ion

Ni²⁺ - Nickel ion

Fe³⁺ - Ferric ion

Fe²⁺ - Ferrous ion

SO₄²⁻ - Sulfate ion

H⁺ - Hydrogen ions

Ni – Nickel

Cr - Chrome

N – Nitrogen

Mo - Molybdenum

Mn – Manganese

Ag – Silver

H₂SO₄ – Sulfuric Acid

FeS – Ferric Sulfide

NiS – Nickel Sulfide

MnS – Manganese Sulfide

HNO₃ – Nitric Acid

HF – Hydrofluoric Acid

Cr₂O₃ – Chromium Oxide

Fe₂O₃ – Ferric Oxide

FeCl₂ – Ferrous Chloride

CrCl₃ – Chromium Chloride

AgCl – Silver Chloride

KCl – Potassium Chloride

KNO₃ – Potassium Nitrate

SEM – Scanning Electron Microscope

EDS – Energy Dispersive x-ray Spectroscopy
XPS – x-ray photoelectron spectroscopy
VBNC – Voisey’s Bay Nickel Company
 i_{corr} – Corrosion current density
 i – Pit current density
 i_o – Exchange Current Density
 E_{inh} – Potential associated with inhibitors and buffers
 Φ - Electrical Potential
 E_{pit} – Pitting Potential
 E_o – Standard Reduction Potential
 E_{corr} – Corrosion Potential
 V_{SHE} – Potential relative to the Standard Hydrogen Electrode
SHE – Standard Hydrogen Electrode
 n – Number of moles of electrons per mole of metal involved in the reaction
F – Faraday Constant
M – Molar
 ΔC – Critical concentration of metal ions
 z – Average oxidation state of cations
D – Diffusion coefficient of metal ions in solution
 a –Pit radius or Depth
 x – Diffusion Length
PRE – Pitting Resistance Equivalent
Ra – Surface Average Roughness
H – Enthalpy
S – Entropy
T – Temperature
E – Driving Potential
G – Gibbs Energy
 t – Time

k – Reaction constant

A – Constant

E_a – Apparent activation energy of the corrosion process

R – Universal gas constant

CPT – Critical Pitting Temperature

η - Over-Potential

ix – Pit Stability Product

AISI – American Iron and Steel Institute

EN – Electrochemical Noise

Vol. – Volume of metal dissolved during the test period

Q – Total charge passed during the test period

M – Molar Mass

ρ - Density

β - Tafel Slope

TABLE OF CONTENTS

ABSTRACT.....	ii
ACKNOWLEDGEMENTS.....	iv
NOMENCLATURE	v
TABLE OF CONTENTS.....	viii
LIST OF TABLES.....	xi
LIST OF FIGURES	xiii
1.0 INTRODUCTION	1
2.0 OBJECTIVES	4
3.0 LOCALIZED CORROSION.....	5
3.1 Stages of Pitting.....	6
3.1.1 Pit Nucleation.....	6
3.1.2 Pit Propagation.....	11
3.1.2.1 Metastable Pitting	11
3.1.2.2 Stable Pitting.....	13
3.1.3 Pit Repassivation.....	15
3.2 Factors Affecting Pitting.....	16
3.2.1 Metallurgical Factors	16
3.2.2 Metal Composition.....	17
3.2.2.1 Microstructure.....	19
3.2.2.2 Surface Treatment.....	20
3.2.2.2.1 Mechanical.....	20
3.2.2.2.2 Chemical/Electrochemical	22
3.2.2.3 Pit Morphology	23
3.2.2.4 Precipitates and Metallic Inclusions	23
3.2.3 Thermodynamic Factors	26
3.2.3.1 Cell Electrochemistry.....	27
3.2.3.2 pH-Overpotential Diagrams.....	27
3.2.3.2.1 Cell Kinetics.....	28
3.2.3.3 Electrolyte Temperature.....	31
3.2.3.4 Electrolyte pH.....	33
3.2.3.5 Pit Electrolyte Composition.....	33

3.2.3.6	Polarization	35
4.0	EXPERIMENTATION.....	37
4.1	Experimental Variables.....	37
4.1.1	Chloride Ion	37
4.1.2	Sulfate Ion.....	39
4.1.3	Iron Ion.....	41
4.1.4	Aeration.....	42
4.2	Experimental Procedures	43
4.2.1	Sample Preparation	43
4.2.1.1	Heat Treatment.....	44
4.2.1.2	Polishing	45
4.2.1.3	Microhardness Test.....	45
4.2.2	Electrolyte Preparation.....	46
4.2.3	Polarization	47
4.2.3.1	Potentiodynamic	47
4.2.3.2	Potentiostatic.....	48
4.3	Experimental Equipment	48
4.3.1	Hardware.....	49
4.3.1.1	Test Cell.....	49
4.3.1.2	Potentiostat.....	51
4.3.1.3	Mechanical Polisher.....	51
4.3.1.4	Microhardness Tester.....	51
4.3.1.5	Reference Electrode	52
4.3.1.6	pH Meter	52
4.3.1.7	Thermocouple	52
4.3.1.8	Constant Temperature Bath	53
4.3.2	Software	53
4.3.2.1	PowerCORR	53
5.0	RESULTS	54
5.1	Potentiodynamic Polarization Tests.....	56
5.1.1	Polarization Data.....	56
5.1.1.1	Pitting Potential.....	57
5.1.1.2	Free Corrosion Potential	59
5.1.1.3	Anodic Knee	60
5.1.1.4	Electrochemical Noise	61
5.1.2	Surface Analysis	61
5.2	Potentiostatic Tests	65

5.2.1	Argon	65
5.2.1.1	Polarization Curves.....	66
5.2.1.2	Pitting Potential.....	68
5.2.1.3	Anodic Dissolution	71
5.2.1.4	Surface Analysis	73
5.2.2	Oxygen.....	81
5.2.2.1	Polarization Curves.....	82
5.2.2.2	Pitting Potential.....	84
5.2.2.3	Anodic Dissolution	86
5.2.2.4	Surface Analysis	87
5.3	Scanning Electron Microscopy	94
6.0	DISCUSSION	96
6.1	Comparison of Polarization Techniques	96
6.2	Mixed Potential Theory	97
6.3	Pit Development and Growth.....	101
6.3.1	Brighten and Etching Dissolution.....	103
7.0	SUMMARY	106
8.0	CONCLUSIONS.....	109
	REFERENCES	111
	Appendix A.....	117
	Appendix B.....	119
	Appendix C.....	121
	Appendix D.....	127
	Appendix E	130
	Appendix F.....	133
	Appendix G.....	136
	Appendix H.....	138
	Appendix I	143

LIST OF TABLES

Table 1. Enthalpy of reaction for inclusion dissolution	25
Table 2. Chemical Composition of Investigated Steel (wt%)	43
Table 3. Test solution ion concentration (Molar)	46
Table 4. Subscripts describing specific pit characteristics	55
Table 5. Pit classification for samples potentiodynamically polarized using solutions 1, 2, 3, 4 and 5 deaerated)	63
Table 6. Pit classification for samples potentiodynamically polarized using solutions 1, 2, 3, 4 and 5 (aerated)	64
Table 7. Current range for samples polarized potentiostatically (deaerated)	67
Table 8. Pit classification for samples potentiostatically polarized using solution 2 (deaerated)	74
Table 9. Pit classification for samples potentiostatically polarized using solution 3 (deaerated)	75
Table 10. Pit classification for samples potentiostatically polarized using solution 4 (deaerated)	78
Table 11. Pit classification for samples potentiostatically polarized using solution 5 (deaerated)	81
Table 12. Current range for samples polarized potentiostatically (aerated)	83
Table 13. Pit classification for samples potentiostatically polarized using solution 2 (aerated)	88
Table 14. Pit classification for samples potentiostatically polarized using solution 3 (aerated)	90
Table 15. Pit classification for samples potentiostatically polarized using solution 4 (aerated)	92
Table 16. Pit classification for samples potentiostatically polarized using solution 5 (aerated)	93
Table 17. Standard reduction potentials	99
Table 18. Test Solution ion concentration (g/L).....	122

Table 19. Specific compound mixtures for Test Solution 1	122
Table 20. Specific compound mixtures for Test Solution 2	122
Table 21. Specific compound mixtures for Test Solution 3	123
Table 22. Specific compound mixtures for Test Solution 4	123
Table 23. Specific compound mixtures for Test Solution 5	123
Table 24. Micro-hardness values for potentiodynamic polarization tests	124
Table 25. Micro-hardness values for potentiostatic polarization tests – Solution 2	124
Table 26. Micro-hardness values for potentiostatic polarization tests – Solution 3	125
Table 27. Micro-hardness values for potentiostatic polarization tests – Solution 4	125
Table 28. Micro-hardness values for potentiostatic polarization tests – Solution 5	126

LIST OF FIGURES

Figure 1. EDS spectra of investigated steel	43
Figure 2. Test Cell Schematic	49
Figure 3. Potentiodynamic curves for solution 1	56
Figure 4. Potentiodynamic curves for solutions 2, 3 and 4 (aerated)	56
Figure 5. Potentiodynamic curves for solutions 2, 3 and 4 (deaerated)	57
Figure 6. Potentiodynamic curves for solution 5	57
Figure 7. Pitting potential as a function of test solution for potentiodynamic Polarization tests.....	59
Figure 8. Free corrosion potential as a function of test solution	60
Figure 9. Pictures of samples after potentiodynamic polarization (deaerated) (a) solution 1 (b) solution 2 (c) solution 3 (d) solution 4 (e) solution 4 (f) solution 5	63
Figure 10. Pictures of samples after potentiodynamic polarization (aerated). solution 1 (b) solution 2 (c) solution 3 (d) solution 4 (e) solution 4 (f) solution 5	64
Figure 11. Potentiostatic curves for solution 2 (deaerated)	66
Figure 12. Potentiostatic curves for solution 3 (deaerated)	66
Figure 13. Potentiostatic curves for solution 4 (deaerated)	66
Figure 14. Potentiostatic curves for solution 5 (deaerated)	66
Figure 15. Slope of the potentiostatic curves as a function of the applied potential for solutions 2, 3, 4 and 5 (deaerated)	68
Figure 16. Plot of applied potential vs inverse of the incubation time for solutions 2, 3, 4 and 5 (deaerated)	70
Figure 17. Pitting potential as a function of test solution for potentiostatic polarization tests (deaerated)	71
Figure 18. Plot of total charge as a function of applied potential for solutions 2, 3, 4 and 5 (deaerated)	73

Figure 19. Pictures of samples after potentiostatic polarization using solution 2 (deaerated). (a) 1.15 V (b) 1.125 V (c) 1.1 V (d) 1.125 V	74
Figure 20. Pictures of samples after potentiostatic polarization using solution 3 (deaerated). (a) 1.125 V (b) 1.1 V (c) 1.075 V (d) 1.05 V	75
Figure 21. Pictures of samples after potentiostatic polarization using solution 4 (deaerated). (a) 1.1 V (b) 1.1 V (c) 1.0 V (d) 1.0 V (e) 0.9 V (f) 0.9 V (g) 0.8 V (h) 0.8 V (i) 0.7V	77
Figure 22. Plot of corrosion current as a function of time for test solutions 4 (deaerated)	78
Figure 23. Revised plot of total charge as a function of applied potential for solutions 2, 3, 4 and 5 (deaerated)	79
Figure 24. Pictures of samples after potentiostatic polarization using solution 5 (deaerated). (a) 1.15 V (b) 1.1 V (c) 1.1 V (d) 1.05 V (e) 0.95 V (f) 0.9 V (g) 0.9 V (h) 0.7 V	81
Figure 25. Potentiostatic curves for solution 2 (aerated)	82
Figure 26. Potentiostatic curves for solution 3 (aerated)	82
Figure 27. Potentiostatic curves for solution 4 (aerated)	82
Figure 28. Potentiostatic curves for solution 5 (aerated)	82
Figure 29. Slope of the potentiostatic curves as a function of the applied potential for solutions 2, 3, 4 and 5 (aerated)	84
Figure 30. Plot of applied potential vs inverse of the incubation time for solutions 2, 3, 4 and 5 (aerated)	85
Figure 31. Pitting potential as a function of test solution for potentiostatic polarization tests (aerated)	86
Figure 32. Plot of total charge as a function of applied potential for solutions 2, 3, 4 and 5 (aerated)	87
Figure 33. Pictures of samples after potentiostatic polarization using solution 2 (aerated). (a) 1.2 V (b) 1.15 V (c) 1.12 V (d) 1.1 V (e) 1.075 V (f) 1.0 V	88

Figure 34. Pictures of samples after potentiostatic polarization using solution 3 (aerated) (a) 1.2 V (b) 1.15 V (c) 1.1 V (d) 1.0 V	90
Figure 35. Pictures of samples after potentiostatic polarization using solution 4 (aerated). (a) 1.0 V (b) 0.95 V (c) 0.9 V (d) 0.9 V (e) 0.8 V (f) 0.8V (g) 0.7 V (h) 0.6 V	91
Figure 36. Pictures of samples after potentiostatic polarization using solution 5 (aerated). (a)1.0 V (b) 1.0 V (c) 0.95 V (d) 0.8 V (e) 0.8 V (f) 0.7V (g) 0.7 V (h) 0.6 V	93
Figure 37. SEM micrograph of a sample polarized at 0.6 V in solution 5 (aerated)	94
Figure 38. SEM micrograph of a sample polarized at 1.05 V in solution 5 (aerated)-1	95
Figure 39. SEM micrograph of a sample polarized at 1.05 V in solution 5 (aerated)-2	95
Figure 40. SEM micrograph of a sample polarized at 0.95 V in solution 4 (aerated)-1	95
Figure 41. SEM micrograph of a sample polarized at 0.95 V in solution 4 (aerated)-2	95
Figure 42. SEM micrograph of a sample polarized at 1.1 V in solution 4 (deaerated)	95
Figure 43. SEM micrograph of a sample polarized at 1.1 V in solution 4 (deaerated)	95
Figure 44. Cross-section view of pits	102
Figure 45. Pitting potentials as a function of test solution for potentiodynamic and potentiostatic polarization tests	106
Figure 46. Proposed extraction process	118
Figure 47. Oxide penetration-90 minute Anneal	120
Figure 48. Oxide penetration-120 minute Anneal	120
Figure 49. Oxide penetration-180 minute Anneal	120

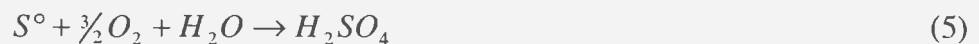
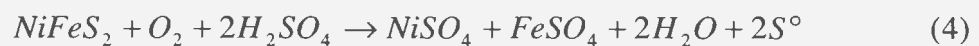
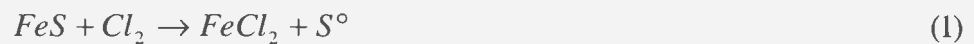
Figure 50. Test Cell.....	127
Figure 51. Pictures of Test Cell (a) Cover (b) Top view of Holder showing Pd auxiliary electrode (c) Stainless Steel Base (d) Bottom view of Holder showing removable sealing washer	128
Figure 52. Type A Pits	130
Figure 53. Type B Pits	130
Figure 54. Type C Pits	130
Figure 55. Type D Pits	130
Figure 56. Type E Pits	131
Figure 57. Classification Tree.....	134
Figure 58. Pictures of samples potentiostatically polarized using Test Solution 4 (deaerated). From L-R, 1.1 V, 1.0 V, 0.9 V, 0.8 V and 0.7 V respectively	136
Figure 59. Pictures of samples potentiostatically polarized using Test Solution 4 (aerated). From L-R, 0.95 V, 0.9 V, 0.8 V, 0.7 V and 0.6 V respectively	136
Figure 60. Pictures of samples potentiostatically polarized. From L-R, Test Solution 4-Deaerated (0.9V) Aerated (0.9V), Test Solution 5 Deaerated (0.9V), Aerated (1.0V) respectively	136
Figure 61. EDS Spectra of a sample polarized in Solution 5-Aerated-0.6V	138
Figure 62. EDS Spectra of a sample polarized in Solution 5-Aerated-1.05V-1-A.....	138
Figure 63. EDS Spectra of a sample polarized in Solution 5-Aerated-1.05V-1-B.....	138
Figure 64. EDS Spectra of a sample polarized in Solution 5-Aerated-1.05V-2-A.....	139
Figure 65. EDS Spectra of a sample polarized in Solution 5-Aerated-1.05V-2-B.....	139
Figure 66. EDS Spectra of a sample polarized in Solution 4-Aerated-0.95V-1-A.....	139
Figure 67. EDS Spectra of a sample polarized in Solution 4-Aerated-0.95V-1-B.....	140
Figure 68. EDS Spectra of a sample polarized in Solution 4-Aerated-0.95V-2-A.....	140
Figure 69. EDS Spectra of a sample polarized in Solution 4-Deaerated-1.1V-2-A	140
Figure 70. EDS Spectra of Stock 1-A.....	141

Figure 71. Localized Etching – Center	143
Figure 72. Localized Etching – Edge.....	143

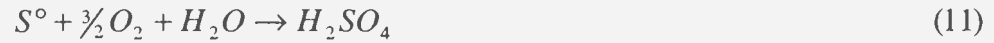
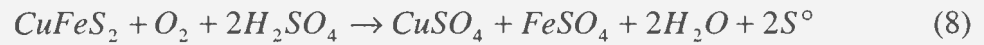
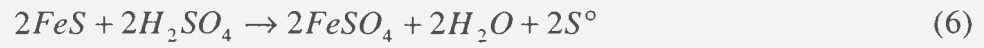
1.0 Introduction

The hydrometallurgical process proposed by Inco for the extraction of the Voisey's Bay nickel sulfide ore involves two leaching processes whereby the nickel sulfide floatation begins its separation process. The two leaching processes are the atmospheric acid chlorine leach and the oxidative pressure leach. Refer to appendix A to view a flowsheet of the proposed extraction process. The environment associated with the two leaching stages in the extraction process and their effects on the corrosion of stainless steel is the focus of the present study.

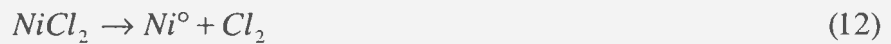
The atmospheric acid chlorine leach is the first step in the hydrometallurgical process. The sulfide floatation concentrate enters an autoclave wherein sulfuric acid and chlorine gas are added to begin the extraction process. The chlorine, oxygen and acid react with the nickel-containing minerals according to the following equations:



After the chlorine leach, the slurry is fed into a second autoclave for the oxidative pressure leach. The major chemical reactions occurring in the oxidative pressure leach can be represented by the following equations:



The final step in the extraction process is to remove the elemental nickel via electrowinning and in doing so, chlorine, oxygen and sulfuric acid are produced at the anodes according to the following equations:



All experimental variables investigated in the current work were based on the two leaching reactions outline above. From the reactions, one can see sulfuric acid is required in the initial stages of leaching to react with the nickel containing minerals, pyrrhotite and pentlandite. In addition to the leaching steps, sulfuric acid is produced at various extraction and separation stages of the process.

From the process information, Ni^{2+} , Cl^- , SO_4^{2-} , and Fe^{3+} were identified and investigated to develop a better understanding of how they will affect any process piping and equipment constructed from stainless steel. Five test solutions were prepared containing combinations of sulfuric acid and the respective ions. In addition to the ions, the effect of aeration was also investigated by bubbling oxygen or argon through the solution during

the testing phase. The specific concentration of ions in each of the five test solutions, as outlined in Table 3, were determined by analyzing the proposed extraction process and associated parameters.

2.0 Objectives

The Faculty of Engineering and Applied Science at Memorial University is conducting a research project in collaboration with Inco Limited and its subsidiary Voisey's Bay Nickel Company (VBNC). The research involves materials related testing of various metal alloys for potential use in the hydrometallurgical processes proposed for Argentina, NL to treat nickel-sulfide concentrate coming from Voisey's Bay, NL.

The primary objective and motivation for my research was to develop an improved understanding of the corrosion processes and mechanisms that occur as a result of the leaching steps during the hydrometallurgical processes of the nickel-sulfide ore. Specifically, pit initiation and propagation associated with 316 L steel immersed in a sulfuric acid medium with varying ion concentration.

My secondary objective was to establish a fully functional corrosion laboratory to be used for future corrosion research. Duties included acquiring and setting up appropriate corrosion testing equipment and software; designing and constructing a test cell that can be configured in a standard three electrode arrangement for polarization testing; establishing metallographic techniques to be used in the preparation of samples for corrosion testing, include, heat treatment, mechanical polishing, etching, hardness testing and electropolishing.

3.0 Localized Corrosion

Generally speaking, corrosion can be described as the degradation and/or dissolution of a material as a result of some interaction with its environment. This degradation can occur uniformly over the entire surface if the anodic and cathodic sites are distributed evenly and move around. However, if the number of anodic and cathodic sites on the corroding surface differ, or more importantly, if the relative area of the sites differ, the mechanism of dissolution becomes localized and contained only to the finite number of anodic sites. The particular mechanism of localized attack associated with an active-passive material such as stainless steel can vary depending on the specific nature of the electrochemical cell established as a result of the metal/electrolyte interfacial conditions. Pitting corrosion can be understood as a mechanism of film breakdown and repair which can be stabilized by the formation of complex species such as Fe (III) and chlorides [1]. Interest in pitting is high because it is often the first step leading to corrosion assisted failure such as crevice corrosion, corrosion fatigue, stress corrosion cracking and failure of coatings [2]. During pitting, small cavities are formed on the surface of the parent metal, which penetrate the passive film and result in localized dissolution of metal ions. Polarization techniques are very helpful in characterizing and understanding the specific corrosion mechanisms associated with a particular metal electrolyte combination. For instance, fluctuations in the corrosion current as a result of anodic dissolution during polarization have peaks which are characteristic of the localized breakdown and repassivation of the passive film [1, 3]. These curves can then be used to determine a metal's resistance to

localized attack as a function of specific experimental variables, such a potential, temperature, electrolyte composition, surface finish etc. The three main stages of pitting, as outlined in the literature [4, 5] are: (1) Pit nucleation (2) Pit propagation (3) Pit repassivation. These three stages of pitting are greatly influenced by two main groups of factors, mechanical and electrochemical.

3.1 Stages of Pitting

3.1.1 Pit Nucleation

The first step in localized corrosion is breaking the naturally occurring or electrochemically induced passive film or oxide on the metal's surface, exposing unprotected metal to the bulk electrolyte. The degree of protection afforded by such an oxide is a function of the thickness, composition, continuity, coherence and adhesion to the metal, and the diffusivities of oxygen and metal in the oxide [6, 7]. The composition and crystallographic structure of a passive film is generally described by a multilayer of metal oxide and/or metal hydroxide and is highly dependant on the bulk electrolyte composition and electrode potential. The corrosion resistant properties of the passive film formed on stainless steel are attributed to chrome, which provides stainless steels with excellent corrosion properties. Nishimura et al. [7, 8] concluded that an enrichment of chrome in the oxide as determined using x-ray photoelectron spectroscopy (XPS),

resulted in the ennoblement of the pitting potential or film breakdown potential. The resistance of a particular film to localized breakdown also depends largely on the specific electrolyte in question. The integrity of the film is compromised by the presence of impurities and intermetallic inclusions in the metal matrix, particularly sulfides (MnS) that provide excellent nucleation sites as outlined in [7, 10, 11, 12, 13, 14]. In addition to the specific film composition, pit morphology, as characterized by the surface roughness of the metal also plays a role in the ability of a specific site to nucleate and develop into a stable propagating pit.

Nucleation events are random in time and can be modeled by a homogeneous Poisson process [11, 15]. The frequency of nucleation events are said to decay exponentially with polarization time indicating there must be a discrete number of pit nucleation sites on the surface. This was shown by a number of researchers [1, 3, 11, 16] wherein the potential and current fluctuations spontaneously generated by corrosion reactions, known as electrochemical noise (EN), were recorded during polarization tests. Rosenfeld and Danilov [17] observed that the majority of pits originate instantaneously, after which no more appear. This is because each initially generated pit is a point 'protector', which essentially reduces the possibility of the pits being originated in other places.

After the initial breakdown of the film, and a new pit site has nucleated, the mechanism by which the pit propagates is well established, being described as a self-propagating autocatalytic process [18, 19, 20, 21]. However, all nucleation sites do not necessarily

develop into metastable or stable pits, they often repassivate immediately after formation [11]. The specific mechanism by which the passive film is breached has been a topic of debate with many different models and hypotheses proposed. The following are three widely accepted models that describe the mechanisms by which the bulk electrolyte contacts the underlying metal promoting metallic dissolution.

I. Penetration Mechanism

The general concept associated with the penetration mechanism is that aggressive anions in the bulk electrolyte diffuse through the passive layer to the metal-oxide interface. On the basis of this idea, a model was developed where it was assumed that cation vacancies migrated from the oxide-electrolyte interface to the metal-oxide interface [4]. The notion that was presented is that if the vacancies penetrate the metal surface at a slower rate than the diffusion rate through the oxide, residual stresses would build up at the metal-oxide interface causing the film to break down. Hoar et al. [20] proposed that aggressive anions (Cl^-) adsorbed on the oxide film surface penetrate the film under the influence of the electrostatic field across the film/solution interface. A contaminated oxide film is formed having a much higher ionic conductivity than the original in an autocatalytic process. As a result of the increase in conductivity, the film may become undermined by vacancy formation or be able to release cations rapidly at the film/solution interface leading to nucleation. Sites most likely to allow aggressive anions to penetrate and

accumulate are at the boundaries located at the matrix/inclusion interface or at any site where the passive film is rendered defective [9, 11, 22].

II. Film Breaking Mechanism

Mechanical stresses which develop in the oxide layer as a result of surface polarization, either, anodically or cathodically, can result in the rupture of the passive film, leaving the underlying metal exposed to the bulk electrolyte. At the film/electrolyte interface fluctuations occur in the potential which result in film rupture near some critical potential. Statistical methods and stochastic models are used to predict the probability of pit initiation [16]. Depending on the specific nature of the electrolyte composition and surface polarization, the ruptured area or surface defect will repassivate or develop into a self-propagating pit. As suggested in [4, 5] pit nucleation can occur in less than a millisecond, which supports the film breaking mechanism as the penetration mechanism would require a longer initiation time to allow for ion diffusion and film breakdown.

III. Adsorption Mechanism

The processes on which the adsorption mechanism is based are not completely understood in their entirety. However, it is widely accepted that aggressive anions, such as halides in the bulk electrolyte, become adsorbed to the protective oxide film where they promote the dissolution. This is achieved by dissolving cations from passive film by

the formation of soluble complex ions as well as the substitution of the anions, namely Cl^- for water and/or O^{2-} [4, 5]. As the potential shifts in the noble direction more chloride ions move into the double layer and at a specific concentration corresponding to the critical pitting potential the chloride ions destroy passivity by displacing the adsorbed atomic oxygen. The anodic overvoltage for the dissolution of the metal is then greatly reduced wherever the chloride ions are in contact with the metal surface in comparison with areas covered with atomic oxygen. This results in pit initiation. When sulfate ions are present, they compete with chloride ions so a higher potential is required for the chloride ion to achieve the critical concentration in the double layer to destroy passivity [23]. In a recent study by Moayed and Newman [24] XPS was used to analyze the oxide constituents of an alloy exposed to chloride containing solution. The results showed that chloride was indeed present in the oxide and a decrease in pitting potential was associated with the adsorbed chlorides. The highest amount of adsorbed chlorides was detected in stainless steel with high sulfur content indicating chlorides were adsorbed on top of MnS inclusions. Schwenk [25] suggested, activator ions such as chloride or bromide are chemisorbed preferentially in the passive layer resulting in an active spot for pit initiation.

3.1.2 Pit Propagation

Once a nucleation site has developed on the surface of the metal, one of three events can occur. (1) it will either develop into a stable, self propagating pit having an indefinite life, (2) the nucleation site will develop into a metastable pit, grow for a short time and then repassivate or (3) repassivate immediately after nucleation. Whichever the case, it has been shown that metastable pitting will always precede the development of a stable growing pit [11, 18, 21, 22, 26, 27].

3.1.2.1 Metastable Pitting

After a nucleation site has developed on the surface of the metal due to the localized breakdown of the passive film, a metastable pit will develop if local conditions satisfy growth kinetics. According to Moayed and Newman [24] pit development and growth will occur in two stages when a surface is anodically polarized. The first is under activation control, where an increase in current accompanies the formation of a few stable pits covered by thin metal/chloride salt. The second stage, under a diffusion control regime, begins with a drop in current due to the coalescence of pits and increased depth. In addition to the diffusion control regime the potential (IR) drop from the base of the pit to the bulk electrolyte is thought to lower the potential of the pit to the active region resulting in active dissolution. The evolution of hydrogen gas from the dissolving pit will indicate the pit is at a lower potential than the electrode surface indicating there is an

IR drop across the pit solution. The specific mechanism of control will depend largely on the applied potential and pit morphology with the higher potentials favoring the diffusion controlling mechanism and lower potentials favoring activation/ IR drop regime as discussed by [22, 28, 29, 30], with diffusion control being the more accepted mechanism of control. However, the initial nucleation process is highly dependent on potential [21], since a finite time is require for a concentration of the relevant ions to be established after which the growth is better described by a diffusion process. Thus, assuming a diffusion control regime, the growth of a pit, stable or metastable, is a result of the diffusion of metal ions from the pit to the bulk electrolyte. The diffusion can be quantified by measuring the corresponding current and applying Faraday's first law [4],

$$Dissolution\ Rate = \frac{i_{corr}}{nF} \quad (14)$$

Where: i_{corr} = corrosion current density

n = number of moles of electrons per mole of metal involved in the reaction

F = Faraday Constant

From which we can determine the anodic dissolution rate.

Due to the relative small size of the pit areas and high over-potential, the current density associated with a pit can be very large indicating rapid dissolution/propagation.

However, this is not the case as the dissolution rate is impeded by the formation of a cover at the mouth of the growing pit acting as a diffusion barrier between the localized pit electrolyte and the bulk solution.

The cover is an electrical insulator comprised of metal hydroxide with salt participation. Rupturing of the cover will result in the passivation of the pit due to its exposure to the bulk electrolyte resulting in dilution of the localized pit electrolyte. Rosenfeld and Danilov [17] found that destroying the cover of a pit during growth resulted in repassivation of the pit. Isaacs and Kissel [31] also concluded that puncturing the cover of growing pits led to repassivation except for the case of some very large pits which continued to grow after the cover was punctured. The tendency of a particular cover to rupture will increase with both applied potential and concentration of aggressive ions [32, 33].

3.1.2.2 Stable Pitting

During metastable pitting, metal cations accumulate inside the pit due to the diffusion inhibiting properties of the pit cover. The additional positive charge attracts aggressive anions from the bulk electrolyte to try and maintain electroneutrality. The solution inside the pit consists of metal chloride and a concentration equal at least 70% of the saturated value is required to achieve stable pit growth. According to Pistorius and Burstein [21] the critical metal ion concentration required to sustain stable pit growth is 3M, where as Sato [34] determined the value to be 2M, where M=Molar (mole/L). Due to the influx of chloride ions, hydrolysis within the pit results in an acidic, aggressive environment impeding any and all attempts of repassivation. Schwenk [25] and Galvele [35] suggest

that both hydrochloric acid concentration and resistance to polarization are necessary for stable coexistence of active and passive pits, both of which are dependent on geometry. Pit initiation and propagation is viewed as a competition between passivating species [MOOH]_{ads}, [MOMOH]_{ads} and non-passivating species (MOH)_{ads}, (MOMCl)_{ads} and (MOMOHCl)_{ads} [32, 33]. The lower pH will also increase the rate of metal dissolution due to the hydrogen reduction reaction characteristic of acidic environments.

According to the early work by Pistorius and Burstein [21] assuming hemispherical pits, the metal ion concentration at the surface of the pit is given by

$$\Delta C = \left(\frac{2\pi}{3zFD} \right) ia \quad (15)$$

Where z is the average oxidation state of the cations and F is the Faraday constant, i is the pit current density, a is the pit radius or depth (hemisphere) and ΔC is the critical concentration of metal ions, taken to be 3M. The requirement for stable pit growth of an open pit in austenitic stainless in a chloride media is summarized as

$$0.3Am^{-1} \leq ia \leq 0.6Am^{-1} \quad (16)$$

Where ia is the pit stability product. That is the critical product of anodic current and pit radius or diffusion length for stable pitting is $0.3Am^{-1}$. However, during metastable

growth the i_a value can be below 0.3 Acm^{-1} , but a stable pit can form due to the addition of a diffusion barrier provided by the porous pit cover. According to the work done by Galvele [35] the critical stability product for the initiation of pitting is obtained when

$$x \cdot i = 10^{-6} \text{ Acm}^{-1} \quad (17)$$

Where: x = diffusion length or pit depth

i = dissolution current density

In any case, once the particular stability product is attained for a given metal/electrolyte combination, pits will propagate in the absence of covers [29].

The stability product also indicates that a stable pit can continue to grow at potentials lower than those required to initiate pitting. Due to the anodic dissolution associated with the initial propagation, the effective diffusion length will increase, and as this occurs the pit stability can be attained at a lower current density or applied potential. Once a stable pit has formed and a diffusion control regime is established, propagation is independent of potential [11].

3.1.3 Pit Repassivation

Pit repassivation will occur if the conditions outlined above are not met and maintained long enough for the pit to become self-propagating. Major rupture of the cover during its

metastable growth stage accelerates the diffusion rate of the metal cations until the pit anolyte is diluted significantly and repassivation is inevitable [29]. Rosenfeld and Danilov [17] concluded that if pits are prematurely open up so as to allow the bulk solution to dilute the localized pit solution such pits would repassivate and new pits would form on the surface of the metal. The specific pit morphology will also play a role in whether a pit will repassivate or propagate. Yashiro and Tanno [36] showed that the amount of chloride in the bulk solution determined the morphology of any pits on the surface. They concluded that low concentrations of chloride ions resulted in small deep pits wherein the stability product was easily attained. In the high chloride solutions, pits were more open and therefore it was harder to achieve the critical stability product for stable pitting. However, Szklarska-Smialowska and Janik-Czachor [37] proposed that the repassivation potential of a particular metal does not depend on the extent to which the test sample has been pitted but rather on the composition of the electrolyte within the pit upon achieving stable growth.

3.2 Factors Affecting Pitting

3.2.1 Metallurgical Factors

The alloying elements, thermal and mechanical treatment associated with any metal play a very important role in its performance. This is very well established with regard to the

change in mechanical properties associated with Fe based alloys with the addition of carbon. In addition to the mechanical properties, the electrochemical properties of a particular metal are also affected by alloying elements as well as the crystallographic structure, resulting in an increased or decreased resistance to metallic dissolution.

3.2.2 Metal Composition

Austenitic stainless steels have excellent corrosion resistance due to their particular alloying elements as well as the decreased tendency for carbide precipitation along grain boundaries as a result of an increased solubility associated with austenite phase. The main constituents responsible for the formation of the austenitic phase are Ni, Mn, N which together with Cr, and Mo result in the formation of a very stable passive film responsible for the resistance to metallic dissolution. The Pitting Resistance Equivalent number (PRE) has been found to give a good indication of the pitting resistance of stainless steels [38]. The PRE can be calculated as follows

$$PRE = Cr(wt\%) + 3.3Mo(wt\%) + 30N(wt\%) \quad (18)$$

The exact role of the alloying elements that do not contribute significantly to the formation of the passive film are unclear, but three possible hypothesis are outlined in the

literature [4]. The first suggests that they might lower the ionic current through the metal-passive interface, the second suggests that they might favor pit repassivation by changing the solution composition inside the pit. Finally, they might counteract the harmful effect of sulfur species which can arise from the dissolution of sulfide inclusions, namely MnS.

Other than Ni and Cr, which are the main constituents of the passive film giving the steel its corrosion resistance, alloying with small amounts of N and Mo can greatly improve the pitting resistance of stainless steel. Nitrogen enriched on the surface of the stainless steel helps passivation of a micropit by preventing the lowering of pH in it before steady growth conditions are established [39]. Some researchers [18] have found the attainment of stable pitting is impeded in Mo containing stainless steels due to unstable potential at the bottom of the pit for long periods of time which prevents the diffusion control regime from being established leading to repassivation. Park et al [22] showed that an increase in Mo content from 0 wt % to 6 wt% increased the breakdown potential of the stainless steel in question from 350 mV_{SCE} to 1000 mV_{SCE}. In addition, the size of pits also decreased with increasing Mo.

The specific mechanism involved in increasing the pitting potential as well as increasing the alloy's ability to repassivate is unclear. Vignal et al. [40] observed that circular islands, composed of molybdenum chlorides, formed on the surface of stainless steel when exposed to chloride solutions thus reducing the amount of local chloride available

to penetrate the passive film. In addition Moayed and Newman [24] conclude that the Mo content in stainless steel had no important contribution to the chemistry of the pit solution.

3.2.2.1 Microstructure

The metallurgical processes associated with the formation of stainless steel will have a dramatic effect on its corrosion resistance. That is, changes in grain size and shape as well as increase in atom vacancy and dislocation density due to cold work. In addition to surface defects, additional energy is also added to the surface as a result of cold work which can introduce internal stress giving rise to stress corrosion cracking. The elongated grains characteristic of cold rolling have an increased surface area to volume ratio as compared with fully annealed uniaxial grains yielding higher dissolution rates. There are three specific localized corrosion problems associated with grain boundaries. First, grain boundaries act as collecting sites for impurity atoms which can serve as nucleation sites. Second, the specific bond energies are lower along the grain boundaries when compared with atoms in the grain making dissolution easier, Thirdly, diffusion occurs much more rapidly along grain boundaries giving rise to the formation of precipitates [41].

3.2.2.2 Surface Treatment

When considering the corrosive resistance of an active-passive metal, one must consider the surface condition of the metal at the metal/electrolyte interface in addition to any microstructural impurities. As outlined in a previous section, the degree of protection afforded by such an oxide is a function of the thickness, composition, continuity, coherence and adhesion to the metal, and the diffusivities of oxygen and metal in the oxide. These parameters will vary depending on the specific treatment applied to the metal surface. The particular surface treatment(s) associated with metallographic preparation can be divided into two distinct categories, mechanical and electrochemical.

3.2.2.2.1 Mechanical

Mechanical surface treatment such as polishing, grinding and sandblasting are often employed during the initial stages of surface preparation. The particular mechanical surface treatment used, if not done properly, can greatly reduce the corrosion resistance of a metal's surface by affecting the electrochemical and mechanical stabilities of the passive film, changing the surface reactivity and by altering the near-surface residual stress state as indicated in [42, 43].

Generally speaking, smooth surfaces tend to exhibit better resistance to localized corrosion when compared to rough surfaces due to the decrease in surface defects [44].

Burstein and Pistorius [27] found that the frequency of metastable pitting events decreased with increased surface roughness and when a metastable pit developed it had a greater probability of achieving stable growth on smoother surfaces. A smooth surface resulted in metastable sites that were more open as compared to sites on the rougher surface, and as a result propagated at higher current densities which in turn resulted in stable growth due to the attainment of the pitting stability product ia . The higher current densities enabled stable pits to form having smaller radii. The reason for the increase in metastable pitting on a rough surface is due to an increase in the actual surface area [27]. Although a smooth surface will yield fewer stable pits when compared to a rough surface it will in fact yield a much higher frequency of nucleation events [11].

In addition to smooth and rough surfaces, compressive, near-surface residual stresses can have a pronounced affect on the corrosion resistance as outlined by A. Ben Rhouma et al. [42]. When a ground surface having a surface roughness average (Ra value) of 0.68μ was sand blasted to an Ra value of 1.18μ the pitting potential increased by 190% from $110 \text{ mV}_{\text{SCE}}$ to $320 \text{ mV}_{\text{SCE}}$. An even larger increase in the pitting potential was observed when the initial residual stress in the surface was higher prior to sand blasting. Although increasing the compressive residual stresses on the surface can improve localized corrosion, it can have negative effects if the treatment is not uniform [45]. Surfaces that are shot peened should also be electropolished to establish a uniform surface eliminating any and all indentations and discontinuities as a result of the particular surface treatment reducing the metals susceptibility to pitting [43]. In addition to compressive stresses,

Suter et al. [46] showed that tensile stress can have adverse effects on the corrosion resistance of an alloy containing non-metallic inclusions, such as MnS.

3.2.2.2.2 Chemical/Electrochemical

Pickling, passivation and electropolishing are three procedures used to improve the corrosion resistance of stainless steel. Pickling and passivation in solutions of HNO₃ and HNO₃ plus HF produces a passive film rich in Cr having excellent corrosion characteristics [6, 47]. Electropolishing on the other hand, will not only produce a Cr rich film, it also improves the surface roughness of the metal and can remove harmful non-metallic inclusions from the surface of the metal through anodic dissolution [48, 49].

The resistance to localized attack can increase by as much as 90 % when electropolishing techniques are used [49]. This is primarily due to the change in film composition, in particular the ratio of Cr₂O₃ to Fe₂O₃ in the passive film, which increased by 166%, from 0.97 in the untreated sample to 2.58 in the electropolished sample. The increase in chromium oxide is due to the production of oxygen at the anode during the polishing procedure which then reacts with the chromium rich surface. In addition to chromium oxide, nickel, chromium and carbon can react to form Nichrome which has excellent corrosion resistance.

3.2.2.3 Pit Morphology

When a pit has initiated, and has achieved stable growth, the localized current density associated with the anodic dissolution can be several orders of magnitude greater than the current density experienced in the passive state. Due to the fact that pits tend to grow directly into the parent material with a relatively small opening gives rise to a high resistance path from the bottom of the pit to the bulk electrolyte. This high resistance coupled with high current density due to the anodic dissolution yields a potential or IR drop across the pit [4].

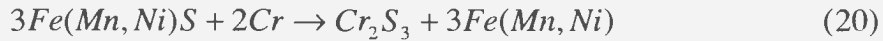
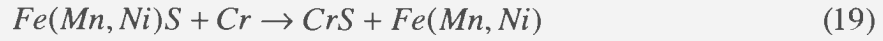
If a salt film forms in the bottom of the pit, the morphology of the pit will change from polygonal to a hemisphere structure. Moayed and Newman [24], found that pit growth under a metal chloride salt layer will produce a pit having a polished interior surface. According to Schwenk [25], circular polished pits can be attributed to noble potentials at which corrosion attack is isotropic. However, in the case of low potentials, irregularly etched pits, mostly hexagons and squares, may be observed from time to time. In any case it was concluded that all pits will become irregular in shape after long test periods. Mankowski and Szklarska-Smialowska [30] found that pits initially developed isotropically in the form of a hemisphere, but after a certain time period settled into the shape of a spherical cup.

3.2.2.4 Precipitates and Metallic Inclusions

As outlined above, the metallurgical process associated with steel formation can have detrimental effects on the corrosion resistance of a metal to localized anodic dissolution. More specifically, the formation of precipitates and metallic inclusions serve as initiation sites for localized attack. When considering stainless steel, the precipitates in question are chromium carbides, which form at grain boundaries resulting in localized areas depleted of chrome. The metallic inclusion(s) of interest are sulfides, namely MnS, FeS and NiS. They, have three basic characteristics associated with them with regard to pitting resistance or lack there of.

They generally have a lower electrical conductivity when compared to the base metal and therefore dissolution will often occur at the inclusion/metal interface. The driving force associated with dissolution at the interface is enhanced by the localized galvanic cell [9, 46].

They have different electrochemical properties and when compared with the parent metal, and therefore can and will readily dissolve at a potential that promotes passivation for the rest of the metal matrix. According to the work of Williams and Zhu [12] the chromium content in the inclusion can greatly increase during heat treatment as a result of diffusion from the parent metal leaving a chromium depleted zone susceptible to localized attack. The excess chromium then reacts with the inclusion species promoting dissociation according to the following equations.



Where the standard enthalpy change of formation $\Delta^\circ H$ for each respective reaction as follows.

Table 1. Enthalpy of reaction for inclusion dissolution

Reaction	$\Delta^\circ H$ (Kcal/mol)
$FeS + Cr \rightarrow CrS + Fe$	-48
$MnS + Cr \rightarrow CrS + Mn$	-50
$NiS + Cr \rightarrow CrS + Ni$	-22
$3FeS + 2Cr \rightarrow Cr_2S_3 + 3Fe$	-144
$3MnS + 2Cr \rightarrow Cr_2S_3 + 3Mn$	-150
$3NiS + 2Cr \rightarrow Cr_2S_3 + 3Ni$	-64

Since all enthalpy values are negative, all reactions can occur spontaneously.

Finally, the size and morphology of the inclusion must be considered. Suter et al. [46] have shown, via microelectrochemical cells that shallow inclusions developed into metastable pits, whereas the deeper inclusions developed into stable pits.

According to Manning et al. [9] heat treatment can result in spheroidized inclusions having a reduced surface area to volume ratio which in turn shifts the pitting potential in the noble direction.

In addition to morphology, the specific size of the inclusion play an important role in pit nucleation. Stewart and Williams [50] showed conclusively that large sulphur-rich

inclusions dominate as nucleation sites where as smaller inclusions with lower sulfur content cannot nucleate a stable growing pit, unless grouped in clusters. In general, increasing the sulfur content of a stainless steel results in a negative shift in the respected pitting potential and an increase in the number of nucleation sites [40].

3.2.3 Thermodynamic Factors

From a microscopic viewpoint, the corrosion process can be described as the transport of atoms, molecules or ions at the metal-electrolyte interface. The transport processes involves several different reactions and can encompass a wide variety of intermediate chemical reactions resulting in the formation of various reaction products in the form of compounds and complex ions. The specific compounds and/or ions formed will vary depending on the characteristics of the metal and electrolyte in question. The application of chemical thermodynamics can aid in the prediction of a metal's susceptibility to corrosion given the properties of the electrochemical cell involved. Quantifying the corrosion process involves analyzing the phenomena associated with the atomic transport described above. This is achieved by analyzing the reaction products, and electrical properties associated with the corrosion reactions, namely potential and current.

3.2.3.1 Cell Electrochemistry

3.2.3.2 pH-Overpotential Diagrams

The pH-equilibrium potential diagram, more commonly known as Pourbaix Diagrams, initially developed by Dr. Marcel Pourbaix, are used to illustrate the thermodynamic state of a material in a dilute aqueous solution at equilibrium. Simply speaking, the diagrams show regions of stability for a given metal as a function of the applied potential and electrolyte pH wherein each region is labeled indicating the dominant stable species present. These diagrams are critical in corrosion analysis when trying to determine the factors that will promote corrosion and those that will impede or completely stop the dissolution process. With respect to stainless steel, the diagrams show regions in which the predominant oxide species are insoluble, indicating regions of passivity.

The driving force associated with all metallic corrosion is based on the change in the Gibbs free energy. For a particular reaction to occur the change in Gibbs free energy must be a negative value, that is the energy associated with the final state of the reaction must be lower than that of the initial state. It is a function of state which provides the criterion for deciding whether or not a change of any kind will tend to occur [51]. The specific magnitude of the driving potential cannot be determined from the Pourbaix diagrams, as they represent equilibrium conditions. However, the tendency for a reaction to occur can be obtained by comparing the applied potential to the equilibrium for the specific pH and ion concentration. The more positive the applied potential as compared

to the equilibrium value the higher the driving potential or corrosion rate. The two underlying principles governing the spontaneity of any reaction are, changes in entropy and enthalpy. The change in Gibbs free energy is defined as.

$$\Delta G = \Delta H - T\Delta S \quad (21)$$

Where: H = enthalpy

S = entropy

T = Temperature

The expression for the driving potential of a reaction is generally presented in the following form [42].

$$E = \frac{-\Delta G}{nF} \quad (22)$$

Where: E = Driving Potential

ΔG = Change in Gibbs Energy

n = Number of moles of electrons per mole of metal involved in the reaction

F = Faraday Constant

3.2.3.2.1 Cell Kinetics

During aqueous corrosion as a result of a positive overpotential, the anodic and cathodic reactions are not at equilibrium and the net anodic current results in dissolution of the

parent metal. At any given time, a surface under free uniform corrosion has localized anodic and cathodic sites which are continuously moving on the surface. However, when considering the anodic dissolution of an active-passive metal, the anodic site or pit is fixed and is very small in relation to the cathodic site. This large cathode/anode ratio results in an increased exchange current density at the anode translating into rapid localized corrosion according to Faraday's first law. An increase in current density can also be achieved if an external source or sink is connected to the particular half-cell. If an external power supply is used to polarize an electrochemical half-cell, the corresponding current density will also change depending on the sign associated with the applied potential. The metal in question can be made active or passive depending on the applied potential and metal/electrolyte interface.

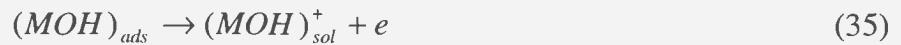
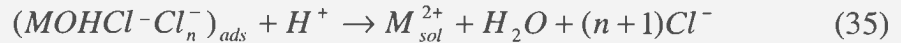
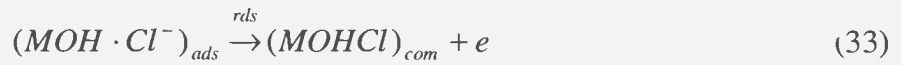
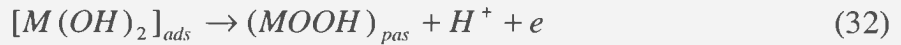
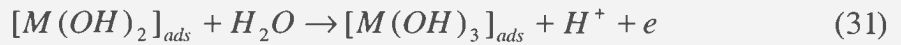
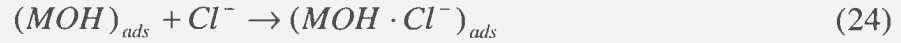
The applied potential according to Schwenk [25] will also determine the number of pits on a particular surface. That is the number of pits will increase with applied potential. However, when stable pitting is established, the associated dissolution current will increase with the square of exposure time according to the following expression.

$$i = ct^2 \quad (23)$$

Where: c = constant

In addition to the applied over potential, specific ions in solution will also have a significant influence on pit growth kinetics. When the concentration of SO_4^{2-} in the solution is greater than the concentration of Cl^- the fraction of adsorbed Cl^- on the pit surface is decreased resulting in low, more stable, dissolution, according to Zhang et al. [52] and Hakkarainen [6].

According to the work of Zhang et al. [52] the following reactions will take place on the film of an austenitic stainless immersed in a solution of sulfuric acid containing chloride ions.



ads, *pas*, *com*, and *rds* represent adsorption, passive, complex, and rate determining step, respectively.

Reactions (25)-(32) are passivation reactions, and reactions (24), (33)-(37) are depassivation reactions. Only when a certain critical potential is reached can reaction (33) take place and reactions (35)-(36) follow it, leading to a high dissolution rate at some local points, which result in pit nucleation.

3.2.3.3 Electrolyte Temperature

Increasing the operating temperature of an electrochemical process worsens the situation with regard to corrosion, however, the specific corrosion rate will depend on the electrochemical cell in question. It is well established that reactions rates, and diffusion rates increase with temperature giving rise to rapid anodic solution. The effect of temperature on corrosion rate can be expressed using the Arrhenius equation [53].

$$k = A[\exp(-E_a / RT)] \quad (38)$$

Where: k = reaction constant

A = constant

E_a = apparent activation energy of the corrosion process

R = universal gas constant

T = temperature

An increase in temperature will also increase the rate at which ionization occurs resulting in an increase in electrical conductivity as well as a decrease in the electrolyte pH. In addition to reaction rates, the solubility of gases in water, particularly oxygen, which is critical for forming a protective film on passive metals will decrease. Higher temperatures can mean oxides become damaged at a faster rate due to the increased diffusion of aggressive anions. In the situation where the controlling step in corrosion is the reduction of oxygen at cathodic sites, an increase in temperature can decrease the reduction reactions and therefore decrease the overall corrosion rate.

For any particular stainless steel, a critical pitting temperature (CPT) can be measured, below which stable pits do not form at any potential up to the onset of transpassivity. The CPT can be obtained by performing potentiostatic polarization test, wherein the potential is held at 750mV and ramping up the temperature until film breakdown occurs [38].

In a chlorinated solution Park et al. [13] showed that temperature influenced the pitting potential more significantly than the actual chloride concentration. Yashiro et al. [54] found that the incubation time for pit initiation for austenitic stainless steel in a chloride media decreased with increasing electrolyte temperature.

However, Leckie and Uhlig [23] found that temperature had little effect on the pitting potential of 18-8 stainless steel in chloride media above 25 °C. Similar results were

reported by Ruijini et al. [55], in that the pitting potential of 904L stainless steel was independent of temperature below 50 °C.

3.2.3.4 Electrolyte pH

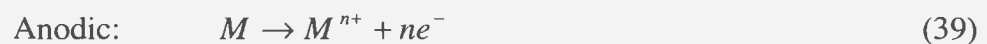
According to the literature [23, 29, 36, 56,] a change in pH of the bulk electrolyte has little or no effect on the pitting potential of stainless in a chlorinated media in the acid range. The work done by Yashiro and Tanno [36], has shown that the pitting potential and repassivation potential are both independent of pH up to a pH = 10. Above this the pitting increased while the repassivation potential remained unaffected. Similar observations were reported by Leckie and Uhlig [23] who concluded that the pitting potential was independent of pH in the acid region because the H⁺ ion does not competitively adsorb on the passive surface.

3.2.3.5 Pit Electrolyte Composition

The composition of the bulk electrolyte in contact with a particular metal is the single most important factor governing any corrosion activity associated with its surface. One can approach a specific corrosion problem from a theoretical point of view, employing the laws of thermodynamics and the appropriate pH diagrams to try and study the electrochemical activity from an academic standpoint. However, from a practical point

of view, the composition of electrolyte is constantly changing, especially when one considers the actual microenvironment associated with localized areas of the metal.

The extent to which localized anodic dissolution occurs depends on the specific composition of the pit electrolyte, which in turn will govern the specific anodic and cathodic reactions involved in the dissolution process. According to Wranglén [19] the propagation of a pit depends upon the formation of a concentration cell in which the pit solution has a higher salt content, a higher acid content and a lower oxygen content than the surrounding bulk solution. Generally speaking, the rate determining steps when considering localized corrosion are the cathodic reactions. As a result, an aqueous environment having a relatively low pH and high dissolved oxygen concentrations will yield higher corrosion rates due to the increase in the possible cathodic reactions. Mankowski and Szklarska-Smialowska [30] attributed the low pH inside pits to the hydrolysis of corrosion products and high concentrations of chloride ions. That is, the presence of FeCl_2 and CrCl_3 increase the activity of the hydrogen ion H^+ . The common anodic and cathodic reactions for an aerated acidic environment are as follows:



Additional ions in the electrolyte will effectively increase the number of possible cathodic and anodic reactions further increasing the rate of corrosion. As discussed in a previous section, the concentration of metal ions in the local environment must exceed critical concentration in order for a stable pit to form.

3.2.3.6 Polarization

As discussed in a previous section, pH-diagrams show regions of stability for a given metal as a function of the applied potential and electrolyte pH wherein each region is labeled indicating the dominant stable species present. Therefore, changing the applied potential through the application of common polarization techniques will greatly effect the stability of all ionic species. When stainless steel is polarized potentiodynamically in an acidic media, its surface will pass through three different regions of the pH-diagram, active, passive and transpassive at which point the passive film will breakdown and pits will nucleate. However, if no pitting occurs up to a potential corresponding to the equilibrium oxygen reduction potential, pitting will be inhibited since the corrosion potential arising from local cell action can never be more noble than this value [56].

According to Galvele [35] the pitting potential of a metal in a given solution is a function of the metal's corrosion potential E_{corr} below which no anodic dissolution can occur, a positive applied over-potential η , required to maintain a net anodic current density inside the pit to ensure the critical pit stability product ix is obtained, the potential drop

associated with any inhibitors or buffer salts E_{inh} and finally the electrical potential drop ϕ associated with the high current density in the pits. Therefore the pitting potential can be expressed as follows.

$$E_{pit} = E_{corr} + \eta + E_{inh} + \phi \quad (42)$$

Since the applied potential is the driving force behind corrosion, both pit growth rate and the repassivation time will increase as the applied potential increases [3].

4.0 Experimentation

4.1 Experimental Variables

The following discussion will identify the specific effects the individual variables and combinations of variables have on the ability of stainless steel to resist localized corrosion. The specific concentration of ions in the five solutions investigated are outlined in the sample preparation section of this document.

4.1.1 Chloride Ion

The chloride ion, known as the Achilles heel of stainless steels, is probably the most extensively investigated ion with regard to its effect on the corrosion resistance of stainless steels as discussed in a previous chapter. Newman et al. [57], confirmed that the chloride ion is responsible for the initial breakdown of the passive film exposing the unprotected metal to the aggressive electrolyte leading to pit initiation. The highest amount of adsorbed chlorides were found on the stainless steels having a high sulfur content suggesting that the chloride ions are adsorbed preferentially atop the uncovered MnS inclusions [30].

According to Rosenfeld and Danilov [17] pitting will occur in a chloride media due to the fact that the strength of the oxygen-metal bond will vary over the surface of the metal. In areas where the bond is weak, adsorption displacement or substitution of the oxygen by the chloride ion is possible. The chloride ions which replace the oxygen on the surface can then penetrate under the oxide film giving rise to pit nucleation. This process is favored by an increase in the chloride ion concentration as reported by [23, 38, 54, 55, 56]. More importantly, the pitting potential (E_{pit}) was found to vary proportionally with the $\log [Cl^-]$.

Leckie [56] found that for each tenfold decrease in chloride ion concentration the pitting potential shifted in the noble direction by about 70mV provided the potentiodynamic scan rate was held constant. Leckie and Uhlig [23] reported similar findings, in that the pitting potential of 18-8 stainless steel was shifted in the active direction by 90 mV for every 10 fold increase in Cl^- concentration.

According to the work of Yashiro et al. [54] and Leckie and Uhlig [23], the pitting potential (E_{pit}) can be related to the chloride concentration by the following expression.

$$E_{pit} = a - b \log[Cl^-] \quad (43)$$

Where a and b are constants and can be determined experimentally.

Estimates for a and b were presented by Leckie and Uhlig [23], who investigated the pitting potential of 18-8 stainless steel polarized in a chlorinated solution at 298 K. Their findings yielded the follow values for potentials measured relative to the standard hydrogen electrode (SHE).

$$a = 0.168 V_{SHE}$$

$$b = 0.088 V / decade$$

In addition to the pitting potential changing as a function of the chloride ion concentration, several researchers have shown that specific nucleation sites also vary with chloride concentration. Park et al. [22] found that MnS inclusions were the primary nucleation sites for low chloride concentrations (1M) where as other surface defects and/or inclusions served equally as nucleation sites in highly concentrated solutions (11M).

4.1.2 Sulfate Ion

The sulfate ion, however, will inhibit the negative effects of aggressive anions such as chloride, increasing a metal's resistance to localized corrosion. The specific mechanisms by which the inhibition occurs were studied by various researchers and are discussed below. During anodic polarization, the potential of the metal surface will shift in the noble direction. As a result, chloride ions become attracted to the surface and move into

the double layer at the metal/electrolyte interface. At a specific chloride ion concentration, corresponding to the critical pitting potential, the chloride ions will destroy the passive film giving rise to pit nucleation. However, when sulfate ions are present in the solution, they compete with chloride ions so a higher potential is required for the chloride ions to achieve the critical concentration [23]. This was verified by the work done by Rossi et al. [58], using XPS they found that the adsorbed chloride in the passive film of austenitic stainless steel decreased as the concentration of sulfate ion in the bulk solution was increased.

More important than the specific amount of sulfate in the bulk solution is the ratio of sulfate ions to chloride ions. Leckie and Uhlig [23] showed that when the ratio of sulfate to chloride is 1.5 no pitting was observed on the stainless steel samples. Their findings led to the development of the following equation which can be used to calculate the minimum sulfate ion activity necessary to inhibit pitting in 18-8 stainless immersed in a chlorinated solution:

$$\log[Cl^-] = 0.85 \log[SO_4^{2-}] - 0.05 \quad (44)$$

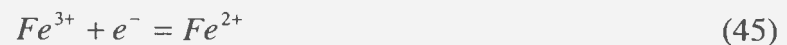
Although the ratio of the sulfate ion to chloride ion is important, the effects are greatly enhanced when the overall ionic concentration is reduced and the ion ratio is maintained [35].

In addition to the pitting potential, some researchers [6, 36] have found that additions of the sulfate ion will also shift the repassivation potential in the noble direction as well as reduce the rate at which a stable pit will propagate. The reason being is that sulfate ions become concentrated within the pit during propagation and will precipitate at lower ionic concentrations due to their lower solubility when compared to metal chlorides.

However, once stable pit growth is achieved, sulfate ions in the bulk solution are fairly ineffective in stopping pit growth [6].

4.1.3 Iron Ion

Unlike the aggressive halides, ferric ions act as inhibitors when present in electrolyte by acting as oxidizing agents through the reduction from Fe^{3+} ions according to the following equation.



By accepting electrons from the metal, the above reaction promotes the anodic dissolution process. Through the work of Gatos [59] it was concluded the corrosion rate of iron in sulfuric acid is greatly increased with additions of ferric ions. This increased dissolution rate is responsible for the formation of a passive film on the surface of stainless steels immersed in sulfuric acid media [60, 61, 62]. When Fe^{3+} ions are added to the electrolyte, the stainless steel begins to corrode rapidly. As a result of the rapid

dissolution, large amounts of metal ions, namely Ni^{2+} and Cr^{3+} are present on the surface of the alloy. These ions then react with oxygen to form a transparent passive anodic film, which in turn impedes any further anodic dissolution.

It has been found that additions of 0.19 g/L of Fe^{3+} ion is sufficient to cause passivity of austenitic stainless steel in boiling 10% sulfuric acid [63].

4.1.4 Aeration

Oxygen is essential in the formation of the passive film on stainless steels. When the electrolyte in contact with a stainless steel becomes stagnant and/or depleted of oxygen an electrochemical cell is established [42]. If the electrolyte contains aggressive ions the naturally occurring passive film becomes depleted as discussed in a previous chapter. However, when the concentration of dissolved oxygen in the solution is high, the passive film will repair itself before any damage to the underlying metal can occur. Pistorius and Burstein [29] observed that the frequency of metastable pitting events decreased as the concentration of dissolved oxygen in the electrolyte increased. However, if the electrolyte is extremely aggressive or the applied potential is above the respective pitting potential of the metal/electrolyte combination, no amount of dissolved oxygen will prevent corrosion.

4.2 Experimental Procedures

4.2.1 Sample Preparation

All polarization tests were performed with samples cut from $\frac{3}{4}$ inch AISI 316 L stainless steel round bar supplied by Russel Metals Inc. having a chemical composition as indicated below in Table 2. The samples were cut into 1/8 inch thick discs using a CNC machine to ensure accuracy and consistency. Prior to performing any polarization tests, all samples were heat treated and mechanically polished as outlined below to ensure repeatability from one sample to the next.

Table 2. Chemical Composition of Investigated Steel (wt%)

Alloy	Cr	Ni	Mo	N	Cu	Mn	Si	C	P	S	Co	Nb
AISI 316L	16.42	10.28	2.11	0.035	0.52	1.51	0.33	0.028	0.04	0.02	0.17	-

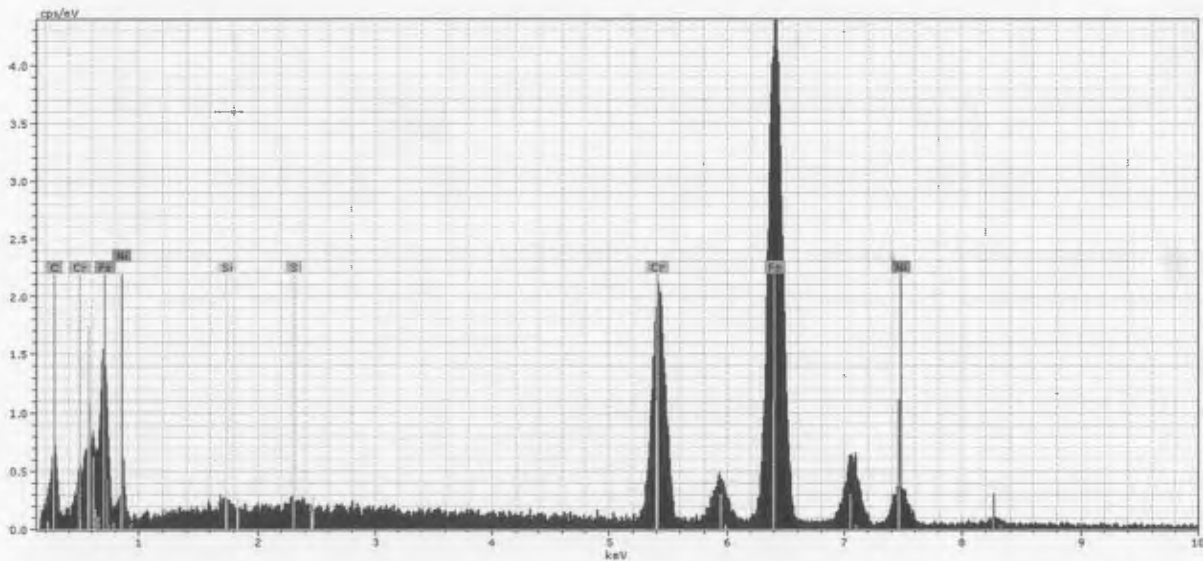


Figure 1. EDS spectra of investigated steel

4.2.1.1 Heat Treatment

After all the samples were cut to the appropriate dimensions, they were annealed in air at 1100 °C for 90 min to remove any residual stresses imparted during machining and to ensure the microstructure was consistent from one sample to the next. The annealing process allowed carbides precipitates to dissolve, grain growth ensuring an equiaxed microstructure as well as allowing inclusions, namely sulfides, to spheroidize improving the overall corrosion resistance of the alloy. Although the alloy used was a low carbon grade stainless steel, samples were quenched in oil after the 90 minute anneal to prevent any sensitization.

The specific annealing time was determined by performing a series of “mini” experiments, during which the annealing time was varied and the sample polished, etched and analyzed using standard metallographic techniques. During the analysis, the grain size was observed and compared to an untreated sample. The thickness of the oxide layer formed on the surface of the samples as a result of the atmospheric anneal had to be considered, since a thicker oxide would required more polishing. In addition to an increase in oxide thickness, oxide penetration between individual grains became an issue when the annealing time was extended beyond 90 minutes. Therefore a 90 minute annealing time was selected for all test samples. Refer to Appendix B for pictures of oxide growth and penetration associated with the various annealing times.

4.2.1.2 Polishing

After annealing, the bulk oxide on the test face and edge of the sample was removed using a lathe. The samples were then mechanically polished with silicon carbide (SiC) paper starting with 280 grit and proceeding to 600 grit. From there, they were polished using a Minimet Polisher with polishing cloths loaded with 6 μm and 1 μm diamond paste respectively. The samples were then cleaned with methanol and degreased with acetone.

4.2.1.3 Microhardness Test

The final step in sample preparation was to perform a Vickers Hardness test ensuring all samples had the same hardness value and therefore the same level of surface residual stress. The hardness test also created an artificial pit on the surface which could be analyzed after each polarization test as a possible nucleation site. All tests were conducted using a 200g weight. Refer to Appendix C for specific hardness values for each test sample.

4.2.2 Electrolyte Preparation

The specific ion concentrations associated with the five test solutions were obtained by combining appropriate mixtures of nickel sulfate, nickel chloride, ferric sulfate, sulfuric acid and deionized water.

Test solution 1, was used as a base case involving only sulfuric acid and deionized water, whereas test solution 2, 3, 4 and 5 included combinations of the various test variables. To ensure consistency from one test to another with regard to the electrolyte, each test solution was prepared in bulk and allowed to stabilize for a 24 hour period before any testing commenced. All solutions were stored in sealed glass containers for the duration of the test period. An attempt was made to measure the pH of each solution after the stabilization period but due to the relatively high acid concentration all pH values were below zero and an error was displayed on the meter. Table 3 shows the theoretical H^+ ion concentration (or H_3O^+) of each solution, assuming the sulfuric acid dissociates 100% and there are no buffering effects, as well as the concentration of ions in each of the 5 test solutions.

Table 3. Test solution ion concentration (Molar)

Test Solution	$[H^+]$	$[SO_4^{2-}]$	$[Cl^-]$	$[Ni^{2+}]$	$[Fe^{3+}]$	$[SO_4^{2-}]/[Cl^-]$
1	2.13	1.07	0	0	0	N/A
2	2.33	1.51	0	0.341	0	N/A
3	2.32	1.36	0.282	0.341	0	4.82
4	2.31	1.215	0.564	0.341	0	2.15
5	2.62	2.18	0.564	0.341	0.537	3.87

Refer to Appendix C for a complete table outlining the specific mixtures used for each test solution.

4.2.3 Polarization

After the sample preparation was complete, the test cell assembled and filled with the appropriate solution, polarization tests were used to characterize each of the metal/solution combinations. All polarization tests were conducted using a standard three electrode cell configuration at a temperature of 24 ± 1 °C.

4.2.3.1 Potentiodynamic

ASTM G-59 was used as a guide when establishing the specific test procedure for the potentiodynamic polarization tests. Prior to starting the potentiodynamic scan, the system, electrolyte and test sample, was monitored for a period of 60 minutes allowing the system to attain its free corrosion potential. After the 60 minute equalization phase, the applied potential was increased at a scan rate of 0.33 mV/s in the positive direction starting at the corresponding free corrosion potential and continuing until a preset threshold current value was reached, at which point the scan stopped. During each test run, the corresponding potential was measured relative to a silver-silver chloride (Ag/AgCl) standard reference electrode and recorded for analysis. This procedure was repeated for each of the five test solutions. For all potentiodynamic polarization tests, the

IR drop through the solution was compensated for by using the current interrupt function associated with the potentiostat.

4.2.3.2 Potentiostatic

Potentiostatic polarization tests were conducted in a similar manner to the potentiodynamic test, in that the system was monitored for 60 minutes prior to starting the test allowing the system to attain its free corrosion potential. However, after the 60 minute interval a discrete potential was applied to the system for a 2 hour period during which the corresponding corrosion current was monitored and recorded for analysis.

This procedure was then repeated for series of different potentials and the entire process repeated for each of the five test solutions. Again, the IR drop through the solution was compensated for by using the current interrupt function associated with the potentiostat.

4.3 Experimental Equipment

This section describes all equipment used during the experimentation, including the test cell and all associated instrumentation and data acquisition devices.

4.3.1 Hardware

4.3.1.1 Test Cell

The test cell used for all corrosion tests was designed and built in the student machine shop at the university. The cell body and cover were constructed from Teflon (PTFE), while the base was constructed from 316 stainless steel to provide an electrical path to the working electrode.

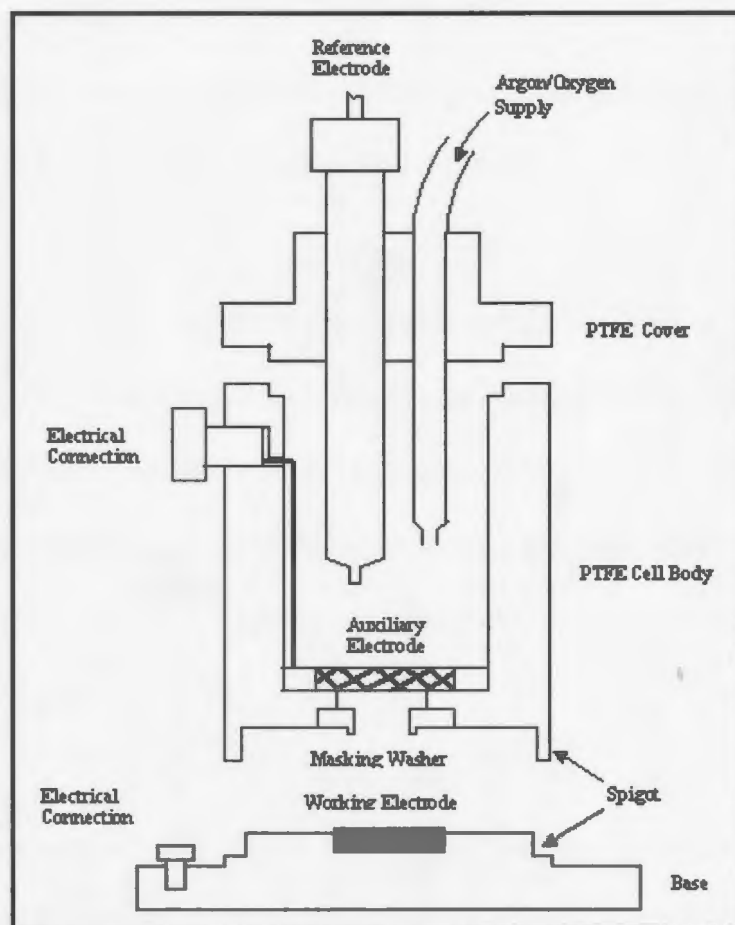


Figure 2. Test Cell Schematic

The base of the test cell served as the holder for the sample (working electrode). A concentric hole 2.5 mm deep, having a diameter of $\frac{3}{4}$ inch was machined in the base which provided support to the sample during assembly. Once the sample was in place, the Teflon cell body (electrolyte holder) was placed over the sample and mechanically fastened to the base with four hex screws. The bottom of the holder was fitted with a removable Teflon masking washer allowing 1.27 cm^2 of surface to be exposed. A compression seal was achieved between the sample and the washer by tightening the four hex screws in the cell body. Spigots were machined on both the cell body and base to ensure concentric alignment during assembly. The internal dimensions of the cell body allowed 45 ml of electrolyte to be added during each test giving an exposed surface area to electrolyte volume ratio equal to $0.02815 \text{ cm}^2/\text{ml}$.

A palladium auxiliary electrode was used to complete the electrical circuit of the three electrode cell. To achieve a uniform current distribution on the surface on the test sample, a palladium mesh was constructed by weaving 0.25 mm wire through a Teflon washer. The washer was then placed in the bottom of the cell body, directly on top of the masking washer. The mesh was connected to a bolt in the topside of the cell body via a single strand of palladium wire.

The cover of the test cell was used to support the associated instrumentation and aeration line. Three holes were machined in the cover to facilitate the reference electrode,

thermocouple and glass pipette. Refer to Appendix D for pictures of the test cell and associated parts.

4.3.1.2 Potentiostat

The potentiostat used for all polarization tests was a Princeton Applied Research (PARC) EG&G Model 273A Potentiostat/Galvanostat capability of supplying an output voltage of 100 V and a full scale current value of 1 A with accuracy of 0.2%. The unit was controlled remotely from a PC which was interfaced with the unit via an IEEE-488 (GPIB) interface using PowerCORR software.

4.3.1.3 Mechanical Polisher

A Buehler Minimet Polisher with 1 μ m diamond abrasive was used to achieve a smooth surface finish on the test samples. This unit allowed the user to vary the polishing speed, normal load and polishing time.

4.3.1.4 Microhardness Tester

Buehler Micromet 1600-1000 microhardness tester was used to perform a Vickers microhardness test on the samples prior to testing. All tests were performed using a 200g weight.

4.3.1.5 Reference Electrode

All potentials recorded during both polarization tests were measured with respect to an Accumet double junction Silver-Silver Chloride (Ag/AgCl) reference electrode. The double junction style of electrode was used to avoid any ionic interference with the specific electrolyte constituents, namely the chloride ion Cl^- and the sulfate ion SO_4^{2-} . The outer body of the electrode was filled with a 1.0M KNO_3 solution while the inner body containing the Ag/AgCl reference body was filled with a 4M KCl solution saturated with AgCl. Both solutions were supplied with the electrode.

4.3.1.6 pH Meter

The pH meter used was a VWR Scientific model 3000 with a measuring range of 0-14. Solutions having a pH value outside this range would result in an error on the digital display.

4.3.1.7 Thermocouple

The temperature during each experimental run was recorded using a type-K thermocouple that was inserted into the test electrolyte via the cell cover and remained there for the duration of the experiment.

4.3.1.8 Constant Temperature Bath

To ensure the temperature variable was consistent for all experimental runs, the test cell was placed in a constant temperature bath which had the capability of maintaining a constant temperature for an indefinite period of time. The particular unit used for the experimentation was a RET-111 refrigerated bath/circulator with microprocessor control supplied by NESLAB Instruments. The instrument had the capability of varying the temperature from $-25\text{ }^{\circ}\text{C}$ to $150\text{ }^{\circ}\text{C}$ with a stability of $\pm 0.01\text{ }^{\circ}\text{C}$ and cooling capacity of 500 Watts. The fluid used in the unit was mixture of water and ethylene glycol to achieve the desired temperature range of $0\text{ }^{\circ}\text{C}$ to $50\text{ }^{\circ}\text{C}$.

4.3.2 Software

4.3.2.1 PowerCORR

PowerCORR is a 32-bit windows based corrosion measurement software supplied by Princeton Applied Research. The software enables the user to set a current threshold limit when performing potentiodynamic polarization and a time limit when performing potentiostatic polarization runs. In addition to control, the software was also used for data acquisition and analysis.

5.0 Results

All results presented in this chapter are in relation to the polarization curves associated with the five test solutions and the metallographic analysis of the individual samples. Potentiodynamic polarization was used to characterize each metal/solution combination prior to conducting any potentiostatic polarization test. In doing so, a pitting potential was determined which served as the basis for the potentiostatic polarization tests as well as a reference to which the pitting potentials obtained using the potentiostatic technique could be compared.

As this is essentially a survey study, one test was conducted for each combination of solution, aeration/deaeration and potential. The results of the tests were accepted when several small changes in applied potential produced results which followed an accepted or explicable trend.

For a comparative surface analysis, a pit classification scheme was developed to describe the type of pits associated with a particular polarization technique and/or test solution. The system uses capital letters to identify the type of pits found on the surface, and subscripts to describe specific characteristics of the pits such as, the average size, surface condition, as well as their density and distribution.

An example of a pit classification is, A_{wxyz}

Where: A indicates pit type
 w indicates the pit size
 x describes the surface condition of the pit bottom
 y indicates pit density
 z indicates pit distribution

The five types of pits identified are:

Type A – Etch pits
 Type B – Circular pits with well defined edge
 Type C – Circular pits with fuzzy edge
 Type D – Irregular pits with well defined edge
 Type E – Irregular pits with fuzzy edge

Type A pits are small, <15 µm in depth, have a polished surface and are uniformly distributed over the entire surface of the sample. The only variable associated with type A pits is their density, whereas pit types B, C, D and E have variable size, surface condition, density and distribution. Refer to Appendix E for an example of the five different pit types. The letters used in the actual classification of specific pit characteristics are outlined in Table 4.

Table 4. Subscripts describing specific pit characteristics

Pit Size	Pit Bottom	Density	Distribution
S=Small B=Big	P=Polished D=Dull E=Etched	L=Low M=Medium H=High	U=Uniform E= Edge

S = (30-70 µm)

B = (71-120 µm)

E indicates pitting is concentrated at the edge of the sample near the metal/washer interface.

To ensure consistency in the classification from one surface to another a classification tree was used to accurately describe the surface the pits as well as other surface parameters such as etching, inclusions and edge dissolution. Refer to Appendix F to see a copy of the classification tree used in the analysis procedure.

5.1 Potentiodynamic Polarization Tests

5.1.1 Polarization Data

The results of the ten potentiodynamic polarization tests are presented in Figures 3-6, each graph shows a plot of the applied potential vs log of corrosion current, from which, one can determine the corresponding pitting potential, free corrosion potential as well as the anodic knee parameters, namely, critical current and the passivation potential. As noted above, some caution is in order regarding the precision (repeatability) of the results, particularly when small differences are concerned

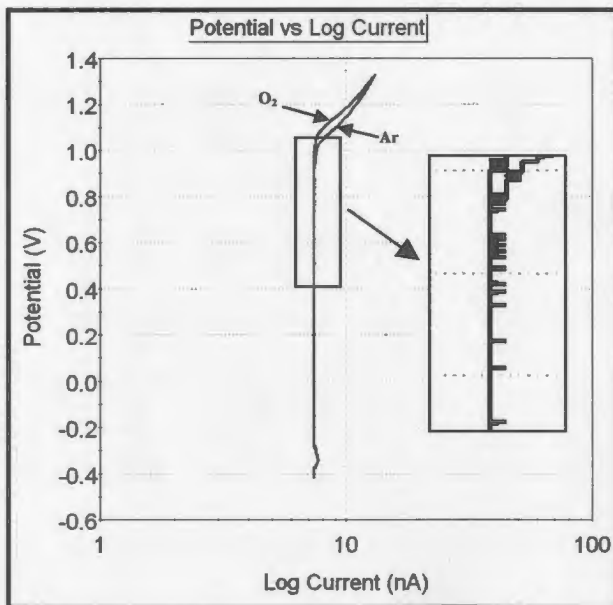


Figure 3. Potentiodynamic curves for solution 1

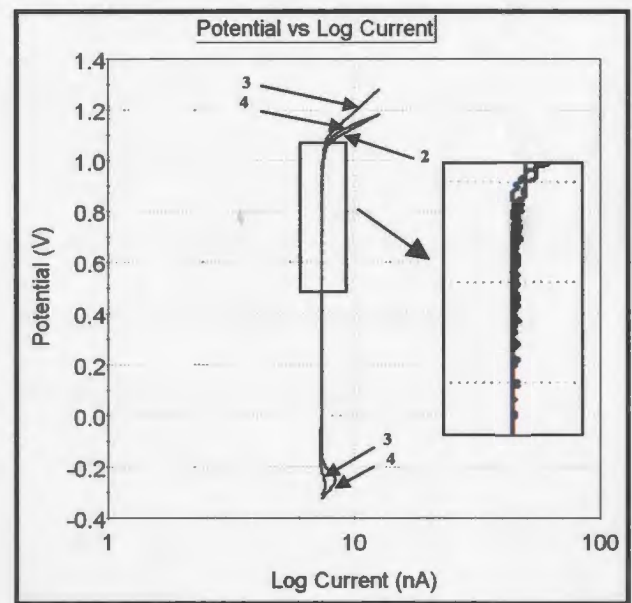


Figure 4. Potentiodynamic curves for solutions 2, 3 and 4 (aerated)

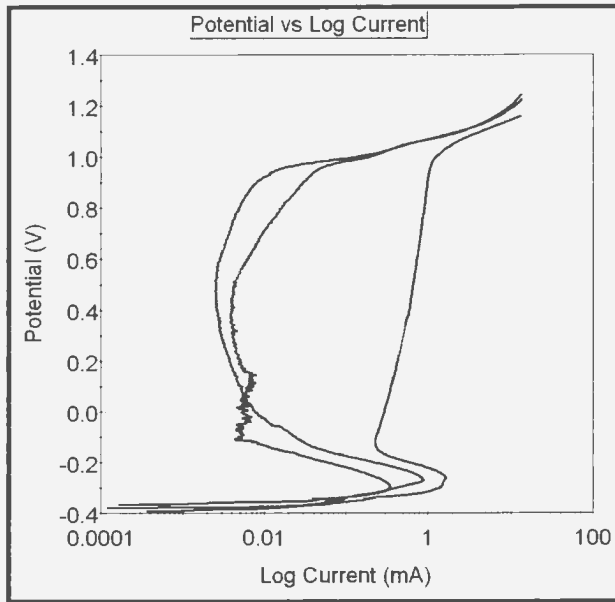


Figure 5. Potentiodynamic curves for solutions 2, 3 and 4 (deaerated)

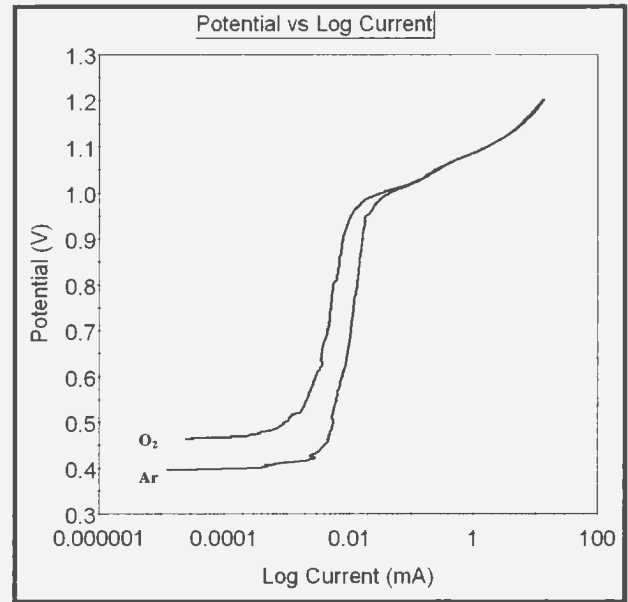


Figure 6. Potentiodynamic curves for Test Solution 5

5.1.1.1 Pitting Potential

The changes in pitting potential associated with each of the five test solutions are presented in Figure 7. From the graph one can see the influence the various solutions have on the respective pitting potentials or more importantly, the influence the test variables have on the pitting potential of test samples.

The pitting potentials associated with the aerated and deaerated solutions follow the same trend with respect to the specific test solutions, however, all values obtained when the electrolyte was aerated were higher than those obtained when the electrolyte was deaerated. The largest difference between the aerated and deaerated tests was obtained when solutions 2, and 3 were used which yielded an average increase of 75 mV. The

smallest difference was obtained when test solution 5 was used, with the aerated value being 25 mV more noble than the deaerated value.

Test solution 1 yielded the highest pitting potential for both methods, indicating the metals resistance to localized attack is the highest when exposed to this solution in comparison to the other four solutions. In addition, the results obtained with solution 5 indicates the metals resistance would be the lowest in this particular environment relative to the other four solutions. However, based on the literature, addition of ferric ions should improve the corrosion resistance of stainless steel immersed in a sulfuric acid solution as discussed in a previous chapter.

When chloride ions were added to the electrolyte (solutions 3 and 4), the respective pitting potentials increased, indicating an increase in corrosion resistance. However, based on the work of various authors [23, 38, 54, 55, 56], as outlined in a previous chapter, the opposite should occur.

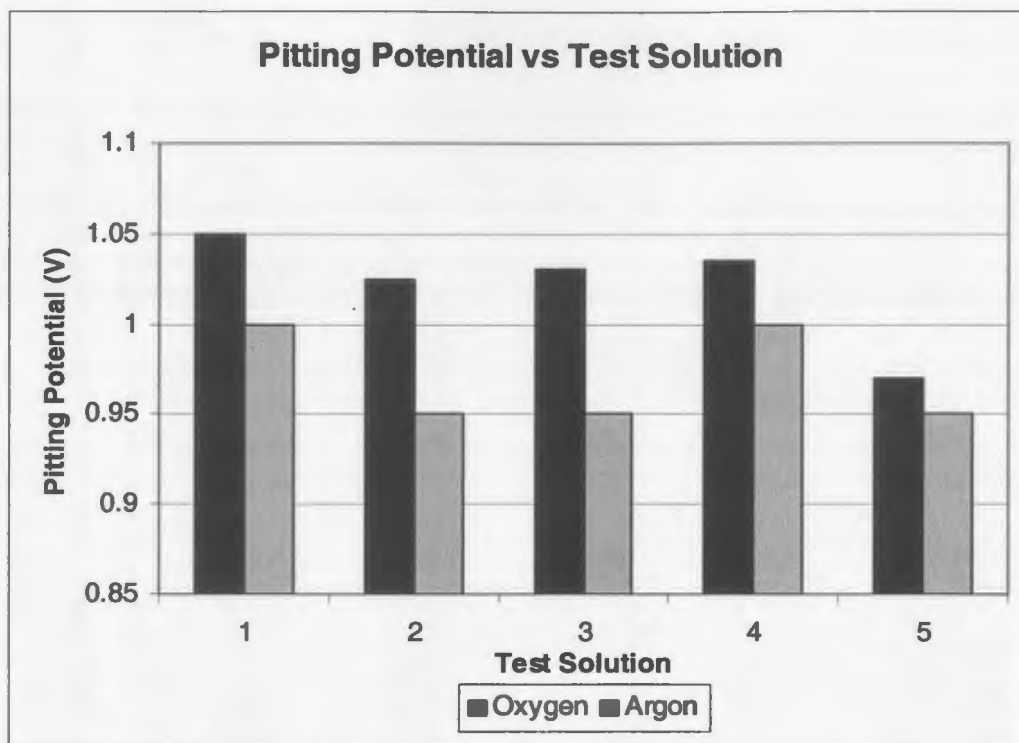


Figure 7. Pitting potential as a function of test solution for potentiodynamic polarization tests

5.1.1.2 Free Corrosion Potential

The free corrosion potentials of each test sample also varied depending on the specific test solution and aeration. For the aerated solutions, the free corrosion potential varied significantly from one solution to the next as illustrated in Figure 8. For test solutions 2 and 3, the free corrosion potential was above the anodic knee and therefore the surface of the metal was in the passive state prior to starting the polarization test. However, when the same solutions were deaerated, the free corrosion shifted in the active direction by 554 mV and 462 mV respectively. Due to this shift, the free corrosion potential was below the anodic knee and as a result underwent active dissolution prior to passivating. The free corrosion potential associated with test solutions 3, 4 and 5 are approximately equal for both methods of aeration, with solution 3 and 4 yielding the lowest values. The

solution yielding the highest free corrosion potential when deaerated was solution 5 and when aerated, the highest value was obtained with solution 2.

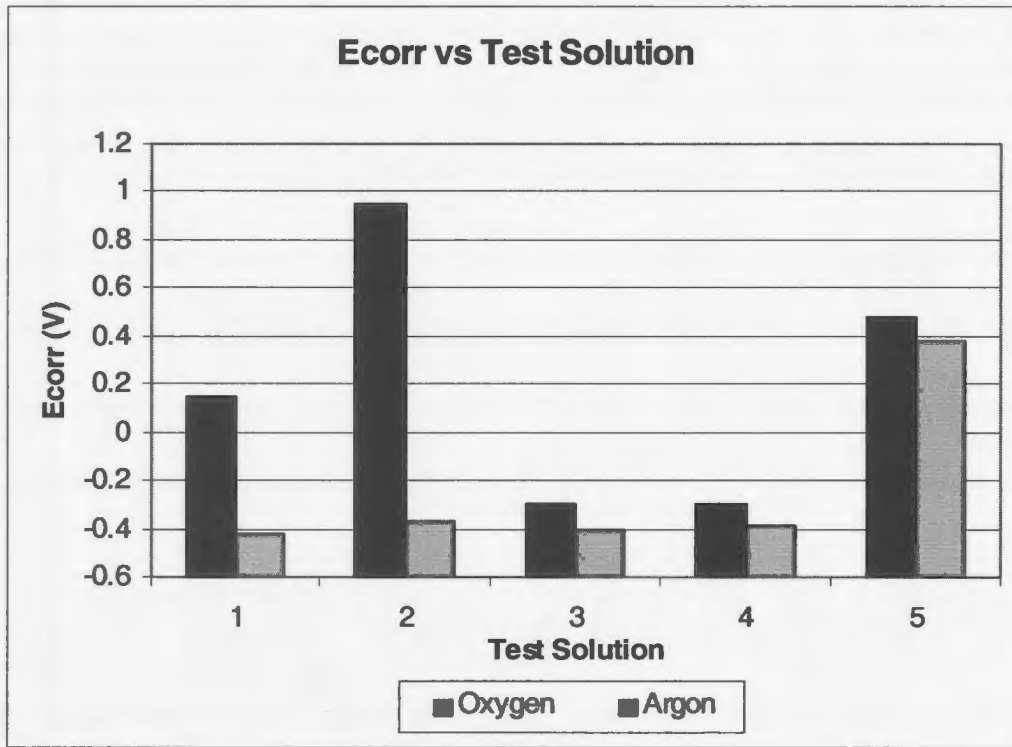


Figure 8. Free corrosion potential as a function of test solution

5.1.1.3 Anodic Knee

An anodic knee was present for all of the polarization curves when the respective solution was deaerated. For the aerated solutions however, only those solutions containing chloride ions resulted in the formation of an anodic knee due to the lower free corrosion potential. As can be seen from Figures 4 and 5, the knee of the curve is shifted to the right and in the noble direction when the chloride ion concentration was increased, indicating a higher potential is needed to provide the critical current required for the

surface to become passive. When test solutions 2, 3 and 4 were deaerated the corresponding critical current values were 0.352 mA, 0.921 mA and 1.69 mA respectively and the passivation potential values were, -0.3 mV, -0.27 mV and -0.25 mV respectively. When the same solutions were aerated the critical current values associated with solutions 3, and 4 were 7.6 nA and 8.38 nA respectively and the corresponding passivation potential were -0.27 mV and -0.25 mV. When ferric ions were added to the electrolyte, the transition from the active region to the passive region was no longer indicated by a distinct knee, as was the case for solutions 2, 3 and 4. The current did not decrease above the active region, instead, it slowly increased until the pitting potential was reached, at which point the current increased rapidly.

5.1.1.4 Electrochemical Noise

Some electrochemical noise (EN) was observed on three of the potentiodynamic polarization curves as indicated in figures 2 and 3. The plots show small fluctuations in current during the scan while the potential is still in the passive range which is characteristic of nucleation events according to the previously published work [1, 3, 11, 16].

5.1.2 Surface Analysis

Surface analysis of each sample was completed after all potentiodynamic polarization tests were completed to identify any pits and characterize them according to the pit classification scheme outline above. The classification results for the deaerated solutions

are presented in Table 5 and the results for the aerated solutions are presented in Table 6. In addition to pits, surface etching was also recorded and described during the analysis. Pictures of the samples, shown in Figures 9 and 10, were taken using a digital camera mounted to an optical microscope.

The only pits observed were on the samples polarized using solution 4, while the remainder of the samples only experienced etching. The amount and type of etching experienced by each sampled varied with solution, aeration and applied potential. Deaerated solutions showed etching along grain boundaries with some localized grain etching near the washer/sample interface. Aerated solutions caused similar grain boundary etching, but showed uniform grain etching even when pits developed on the surface. Lowering the applied potential resulted in an increase in localized etching at the sample/washer interface for nearly all samples.

The indentation on the surface of the sample as a result of the hardness test did not influence the development of pits for the deaerated solution, but possibly served as a nucleation site for the aerated solution as the indentation could not be located during analysis of pitted samples.

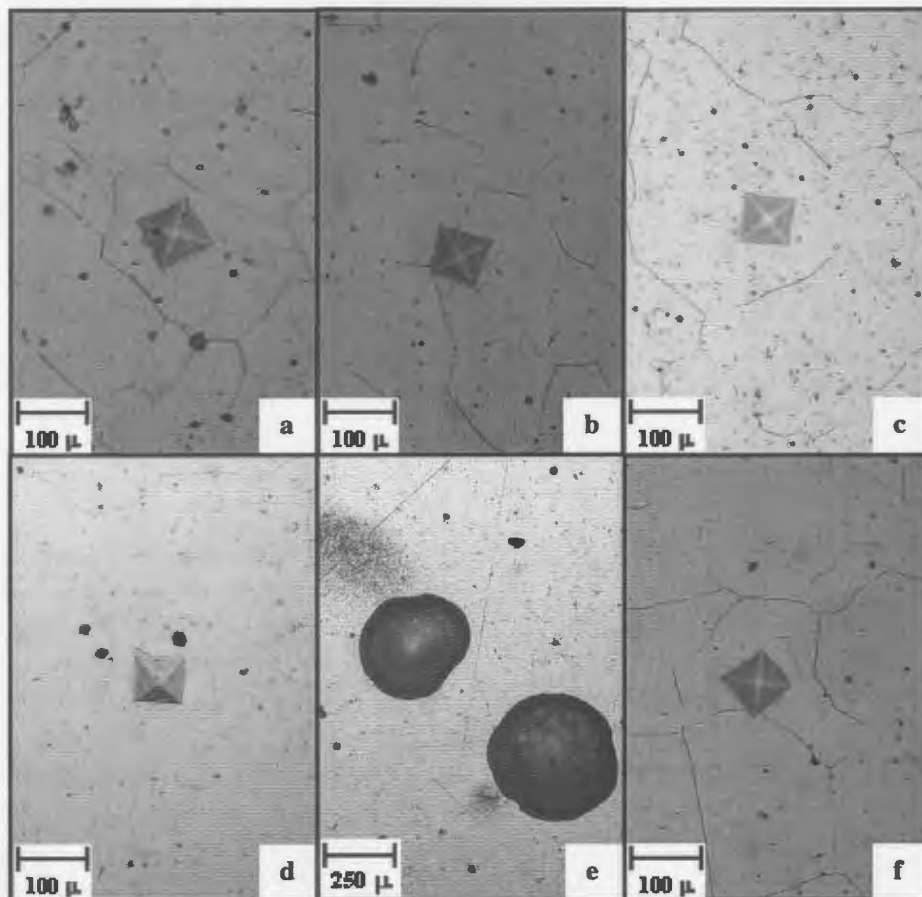


Figure 9. Pictures of samples after potentiodynamic polarization (deaerated).
 (a) solution 1 (b) solution 2 (c) solution 3 (d) solution 4 (e) solution 4 (f) solution 5

Table 5. Pit classification for samples potentiodynamically polarized using solutions 1, 2, 3, 4 and 5 (deaerated)

Test Solution	Type of Pit
1	N/A
2	N/A
3	A _H
4	B _{SPL}
5	N/A

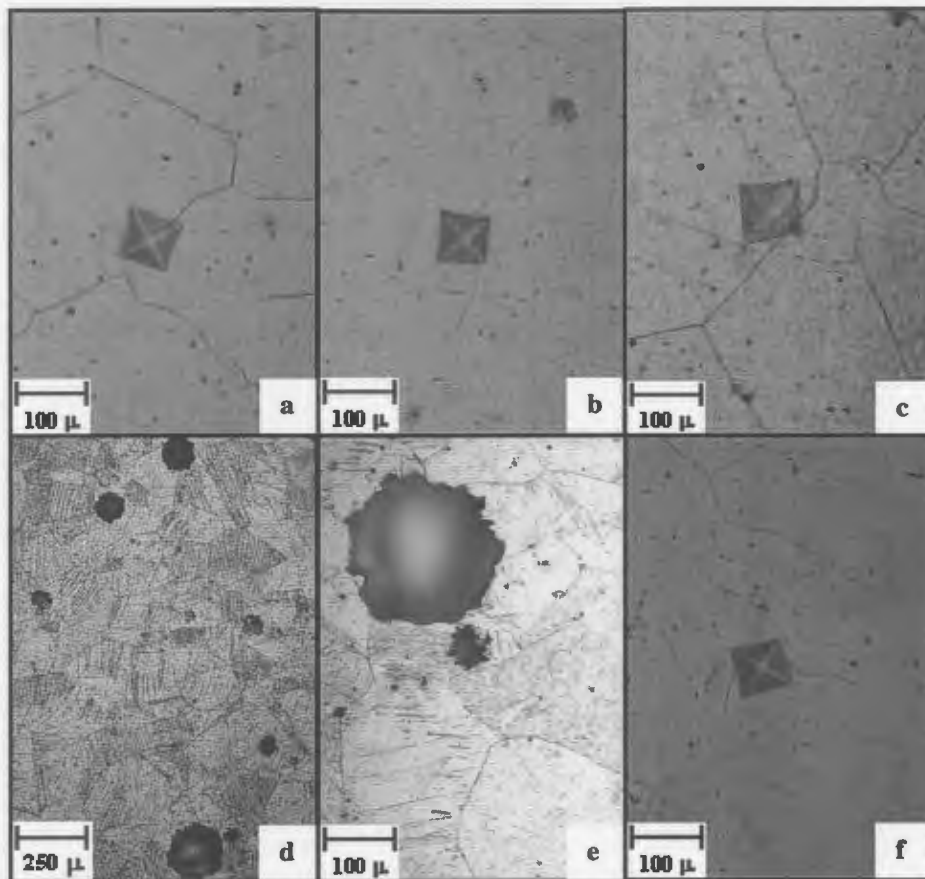


Figure 10. Pictures of samples after potentiodynamic polarization (aerated).
 (a) solution 1 (b) solution 2 (c) solution 3 (d) solution 4 (e) solution 4 (f) solution 5

Table 6. Pit classification for samples potentiodynamically polarized using solutions 1, 2, 3, 4 and 5 (aerated)

Test Solution	Type of Pit
1	N/A
2	N/A
3	A_L
4	C_{SDLU}
5	N/A

5.2 Potentiostatic Tests

The polarization curves associated with the potentiostatic tests are presented in the following sections, and show plots of the corrosion current as a function of test time. From the respective plots, the true pitting potential can be determined by plotting each discrete potential against the inverse of the incubation time, the time elapsed until the current started to increase. The intersection of the extrapolated curve with the y-axis will correspond to the true pitting potential for that particular metal/solution combination as described by various authors [37, 64, 65]. Using this method to determine the pitting potential allows one to validate the procedure by examining the surface after each polarization test to see if any pits developed. The results from the respective tests can be compared on a relative basis by plotting the data using a log-log scale and calculating the slope of the curve after the incubation time. For hemispherical pit growth, the slope of the curve should be 2 according to Schwenk [25] who showed that the corrosion current was proportional to the square of the test time, Eq. 23. Taking the log of both sides will give an equation of the form.

$$\log(i) = \log(c) + 2\log(t) \quad (46)$$

5.2.1 Argon

The results for the samples polarized in deaerated solutions are presented below in Figures 11-14.

5.2.1.1 Polarization Curves

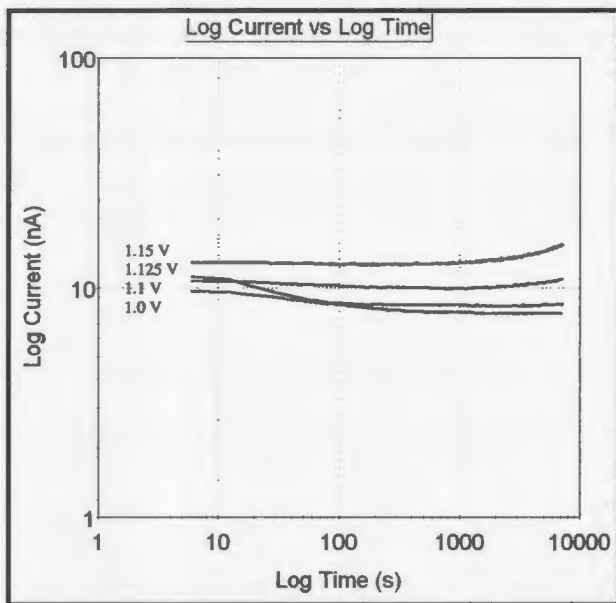


Figure 11. Potentiostatic curves for solution 2 (deaerated)

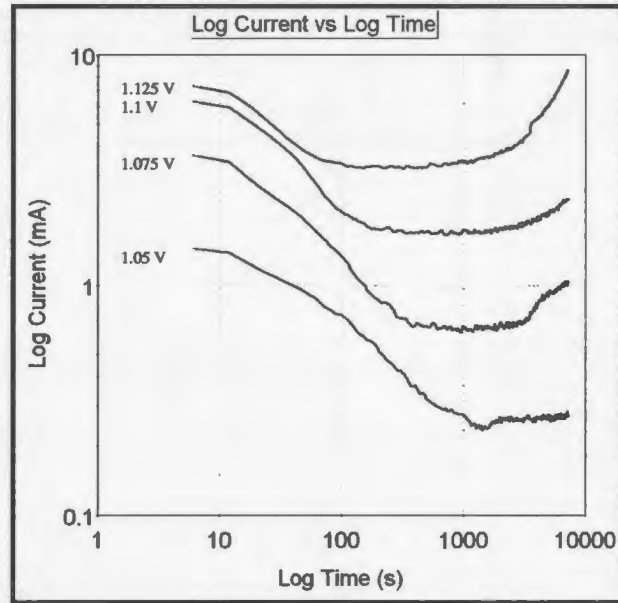


Figure 12. Potentiostatic curves for solution 3 (deaerated)

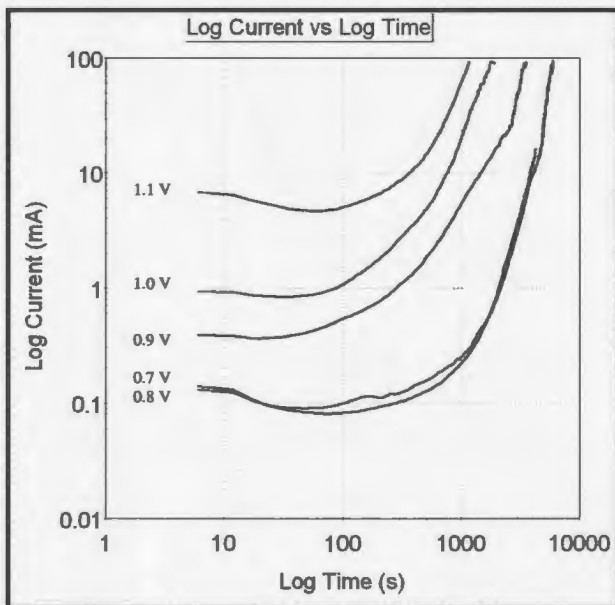


Figure 13. Potentiostatic curves for solution 4 (deaerated)

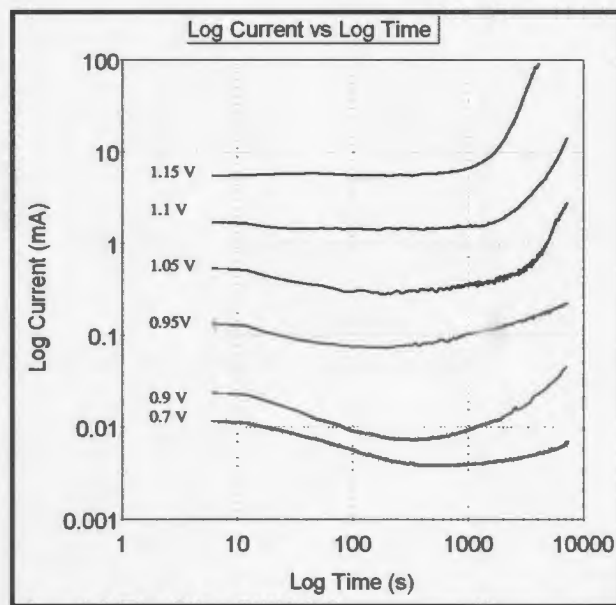


Figure 14. Potentiostatic curves for solution 5 (deaerated)

Solutions 2 and 3 show a distinct increase in the incubation time as the applied potential is incrementally decreased, until the potential is below the true pitting potential, at which point the current remains constant. Solutions 4 and 5 however, show the opposite effect, in that the incubation time initially decreases with applied potential but then begins to increase as the potential is lowered below 0.9 V for solution 4 and below 0.95 V for solution 5.

All three solutions containing chloride ions yielded higher current values when polarized as compared with the chlorine free solutions. The current values associated with solutions 3, 4 and 5 are in the mA range where as the current values associated with solution 2 are in the nA range. The difference in the maximum and minimum current values associated with each test solution is given below in Table 7.

Table 7. Current range for samples polarized potentiostatically (deaerated)

Test Solution	Min. Current Value	Max. Current Value	Current Range
2	7.7 nA	15.42 nA	7.72 nA
3	0.28 mA	8.64 mA	8.36 mA
4	14.7 mA	95.2 mA	80.5 mA
5	6.93 μ A	90.68 mA	90.67 mA

Figure 15 shows how the max slope of each curve beyond incubation changes with applied potential for solutions 2, 3, 4 and 5. As outlined above, if hemispherical pits develop on the surface of the sample, the slope of the curve should be 2.

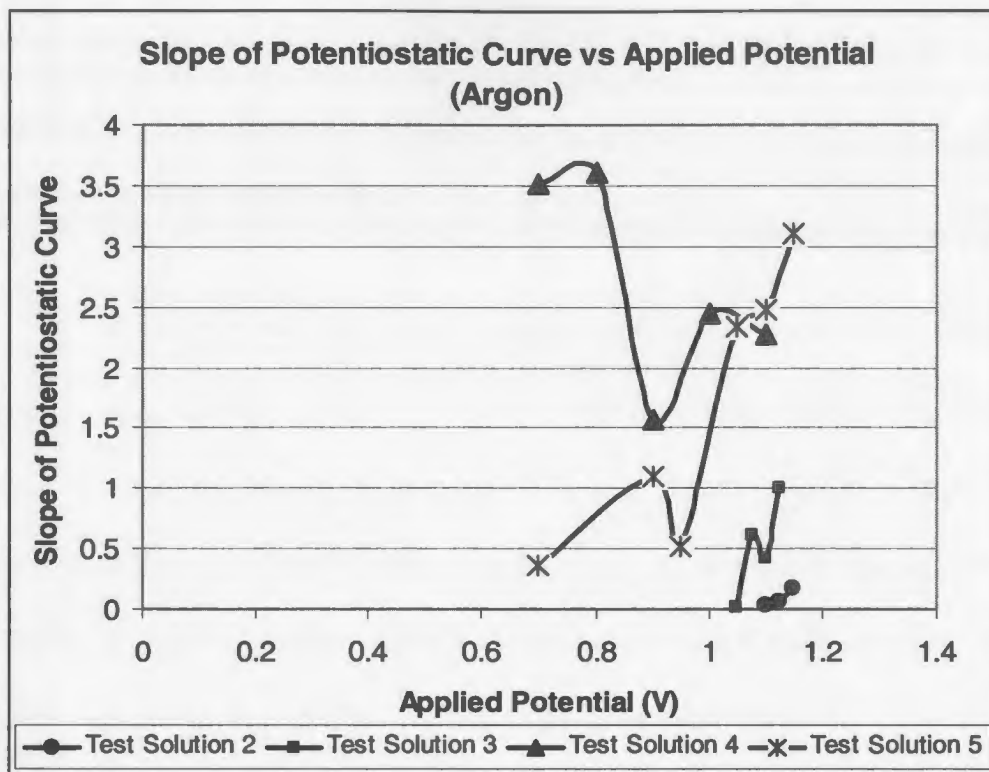


Figure 15. Slope of the potentiostatic curves as a function of the applied potential for solutions 2, 3, 4 and 5 (deaerated).

From the plot one can see that the slope of the curves for all solutions except solution 4 tends to increase with applied potential.

5.2.1.2 Pitting Potential

The results obtained when the applied potential was plotted against the inverse of each respective incubation time are shown below in Figure 16. A line of best fit was drawn through the points and extrapolated until it intersected the y-axis, this value was taken as the true pitting potential of that metal/solution combination. The data associated with solutions 2 and 3 produced results readily permitting the plot of a line of best fit.

However, when the data for solutions 4 and 5 were plotted, the actual sample had to be referenced and some judgment used to determine the lowest potential for pitting as discussed in the next paragraph.

In the case of solution 4, the data points show a trend, opposite to what is expected based on previous research, [37, 64, 65], that is, the incubation time decreases with applied potential resulting in a line that has a negative slope. When the surface of the samples was further analyzed, pitting could only be observed for potentials above 0.8 V. Therefore the line of best fit was drawn through point corresponding to 0.8 V to the point corresponding to the next positive potential and then extrapolated.

The points associated with solution 5 also show some irregularities when plotted and therefore also required further interpretation. According to the work of Alonso-Falleiros et al [64] potentiostatic polarization techniques can be used to determine both the stable pitting potential as well as the metastable pitting potential of a particular metal/solution combination. Since both of these potentials are determined in the same manner, when metastable pitting occurs on the surface the incubation time will begin to increase below the stable pitting potential and therefore will produce two distinct trends when plotted. This was the case with solution 5, stable pits were only observed above 1.05 V, therefore the increase in incubation time below this value was a result of metastable pitting. As a result, two lines of best fit were drawn through the data and extrapolated until they intersected the y-axis representing the two potentials. The metastable pitting potential for

solution 5 is approximately 0.65 V. The potentials associated with stable pitting as a function of specific test solutions are presented in Figure 17.

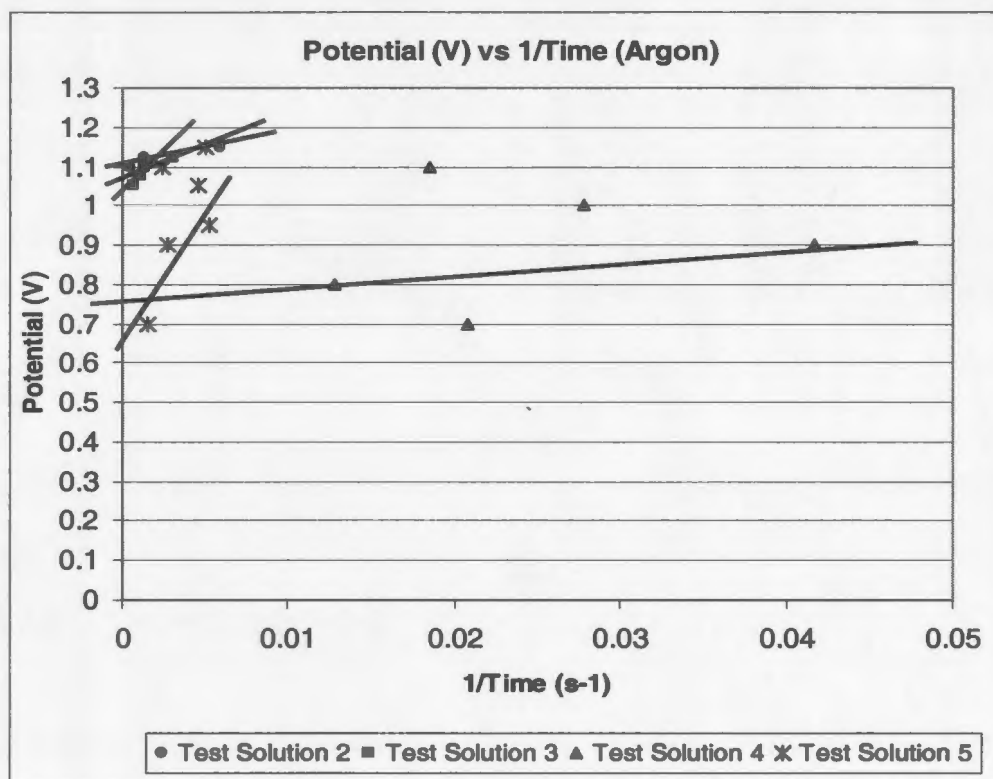


Figure 16. Plot of applied potential vs inverse of the incubation time for solutions 2, 3, 4 and 5 (deaerated).

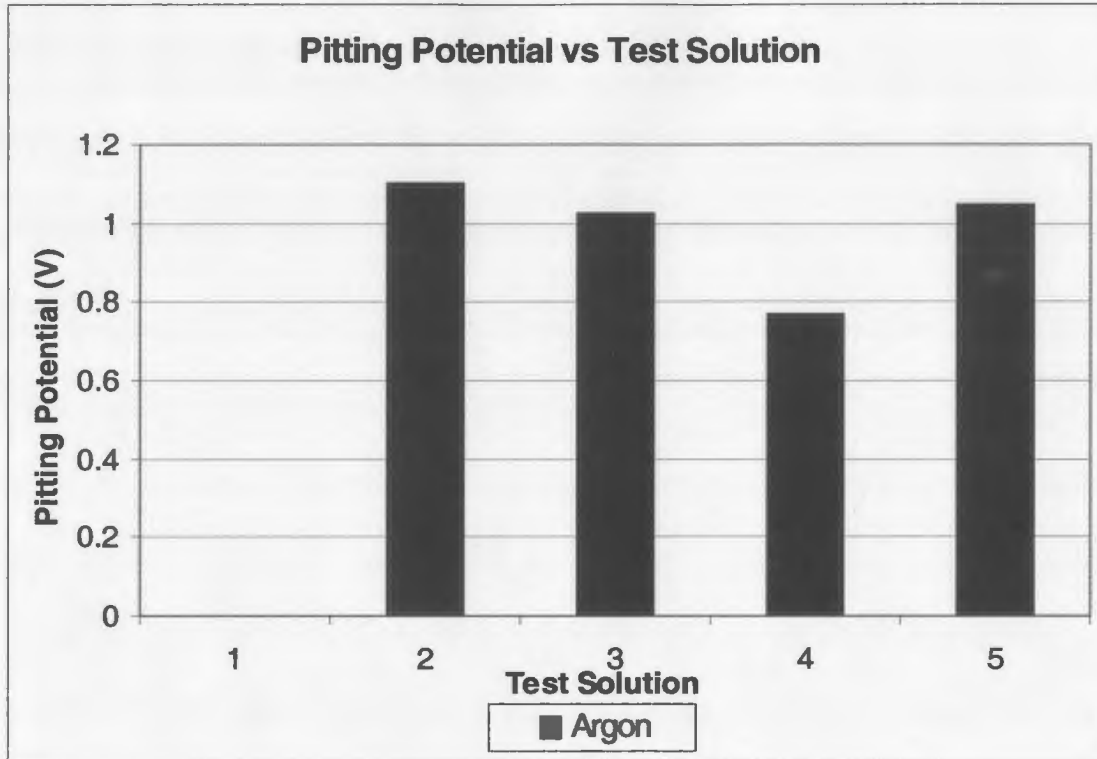


Figure 17. Pitting potential as a function of test solution for potentiostatic polarization tests (deaerated)

5.2.1.3 Anodic Dissolution

The volume (Vol.) of metal dissolved during the test period is directly proportional to the amount of electric charge transferred according to Faradays first law, of the form

$$Vol = \frac{QM}{\rho nF} \quad (47)$$

Where

- Q = The total charge passed in Coulombs
- M = Molar mass of the stainless steel
- ρ = Density of the stainless steel
- n = The number of electrons per mole of stainless steel
- F = Faraday constant

For a particular material, the equation can be rewritten as

$$Vol = cQ \quad (50)$$

$$\text{Where } c = \frac{M}{\rho nF} = \text{constant}$$

Therefore by plotting the total charge transferred as a function of the applied potential for all solutions one can relatively compare the amount of anodic dissolution for each specific test. Figure 18 shows such a plot indicating the total dissolution is low at low potentials, increasing as the applied potential is increased for all solutions except for solution 4. The results pertaining to solution 4 show that the total dissolution increases when the potential is increased from 0.7 V to 0.8 V and then decreases beyond 0.8 V. The plot also shows that the maximum dissolution is associated with the sample polarized at 1.15 V in solution 5. However, when the actual surfaces were analyzed, as described in the next section, the maximum anodic dissolution was associated with solution 4.

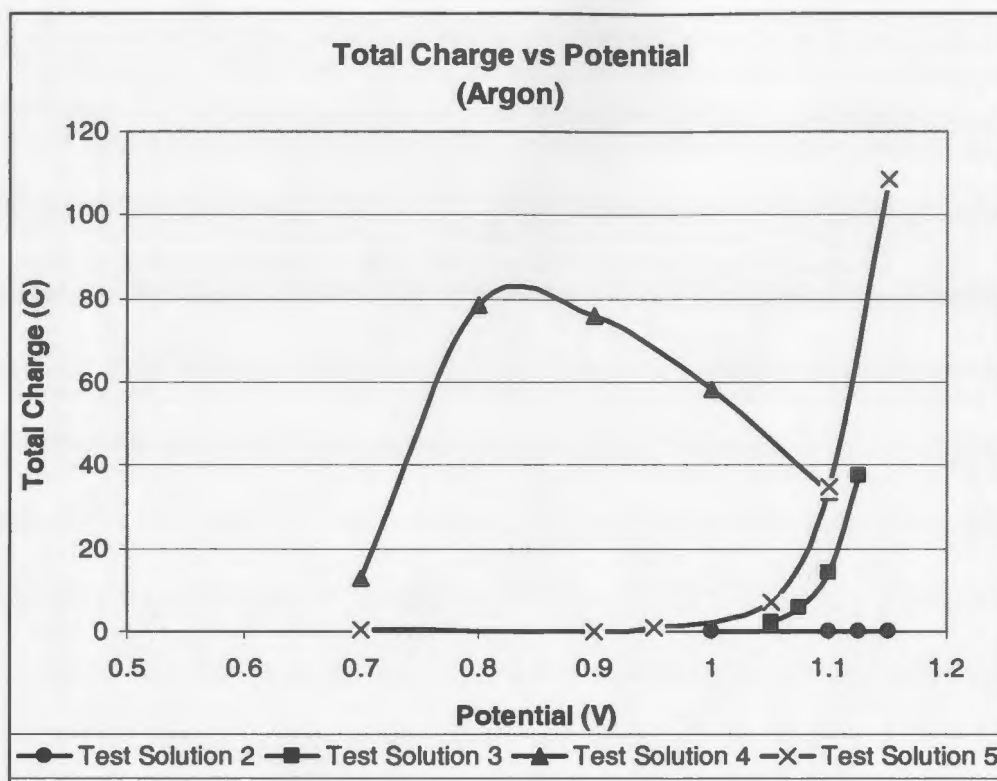


Figure 18. Plot of total charge as a function of applied potential for solutions 2, 3, 4 and 5 (deaerated)

5.2.1.4 Surface Analysis

After all polarization tests were completed, the surface of each sample was analyzed to identify and classify all pits, determine the extent of surface etching and quantify any dissolution at the sample/washer interface. Again, pictures of the samples were taken using a digital camera mounted to an optical microscope.

Solution 2

Only type A pits were observed on the samples polarized using solution 2 as summarized in Table 8. The density of the etch pits decreased with potential as did the intensity of the grain boundary etching. At lower potentials, severe grain etching was observed near the sample washer interface. In addition to etching, inclusions were visible along grain boundaries at the higher potential values but appear to be irrelevant in the development of the small etch pits which can be seen distributed uniformly over the entire surface. The microhardness indentation can be visibly seen on all samples (Figure 19) and do not show any signs of contributing to pit development.

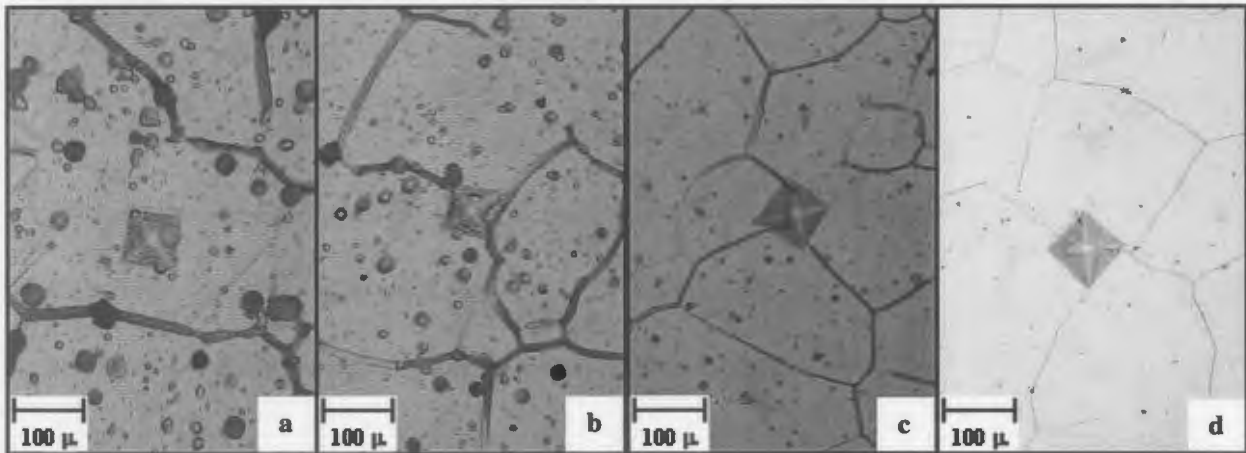


Figure 19. Pictures of samples after potentiostatic polarization using solution 2 (deaerated). (a) 1.15 V (b) 1.125 V (c) 1.1 V (d) 1.05 V

Table 8. Pit classification for samples potentiostatically polarized using solution 2 (deaerated)

Applied Potential (V)	Type of Pit
1.15	A _H
1.125	A _M
1.1	A _L
1.05	N/A

Solution 3

The surface analysis for the samples polarized using solution 3 (Figure 20) show similar results to the samples polarized using solution 2, in that type A pits were present and the etching was associated with the grain boundaries. Both pit intensity and grain boundary etching decreased with applied potential and at lower potentials localized grain etching was observed which increased in intensity near the edge of the samples at the sample/washer interface. In addition to the localized etching, type C pits were observed near the edge of the samples when the polarization potential was 1.125 V. Again, the indentation didn't effect the pitting or etching process associated with the samples as it was highly visible on all samples. The type of pits found on the samples is summarized in Table 9.

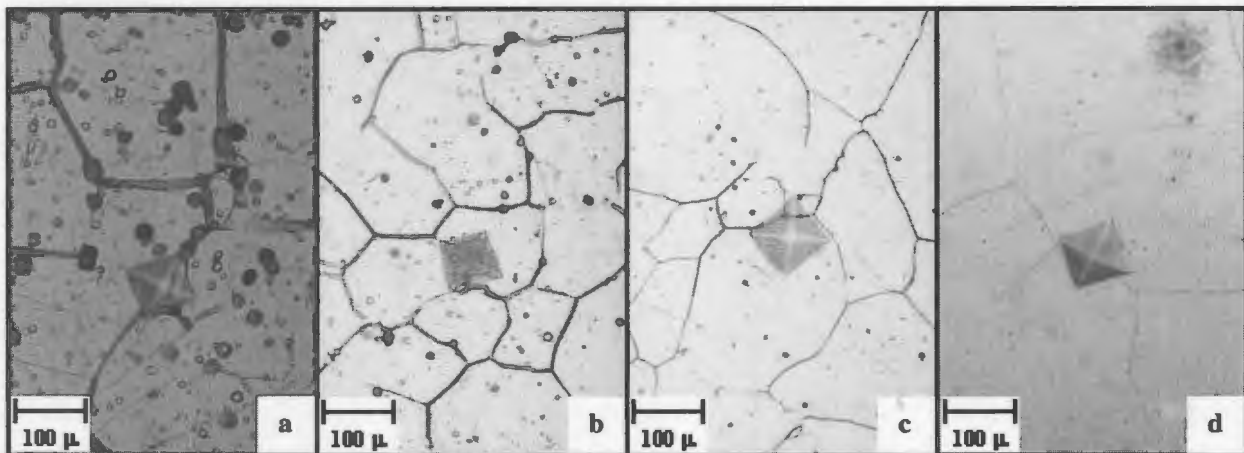


Figure 20. Pictures of samples after potentiostatic polarization using solution 3 (deaerated).
(a) 1.125 V (b) 1.1 V (c) 1.075 V (d) 1.05 V

Table 9. Pit classification for samples potentiostatically polarized using solution 3 (deaerated)

Applied Potential (V)	Type of Pit
1.125	A_H, C_{SPL}
1.1	A_M
1.075	A_L
1.05	N/A

Solution 4

When the applied potential was above 0.9 V, large circular pits developed on the surface of the samples as can be seen in pictures e and f of Figure 21. The surface between pits appeared to be unaffected for the most part, however some localized grain etching was observed near the edge of the sample. The indentation on the surface does not appear to play a role in the nucleation of the pits that formed as can be seen in picture c and of Figure 21. When the applied potential was 0.9 V, shallow irregular pits developed on the surface and the intensity of the localized etching increased. When 0.8 V was applied a single circular pit developed on the surface and no pitting was observed at potentials below 0.8 V.

In addition to pitting, a large amount of anodic dissolution was observed near the sample/washer interface for potential values of 0.8 V, 0.9 V and 1.0 V respectively. This dissolution is responsible for the high charge transfer indicated in Figure 18. Refer to Appendix G for a comparative picture of samples showing the dissolution ring at the sample/washer interface.

A summary of the pits observed on each surface is presented in Table 10 below.

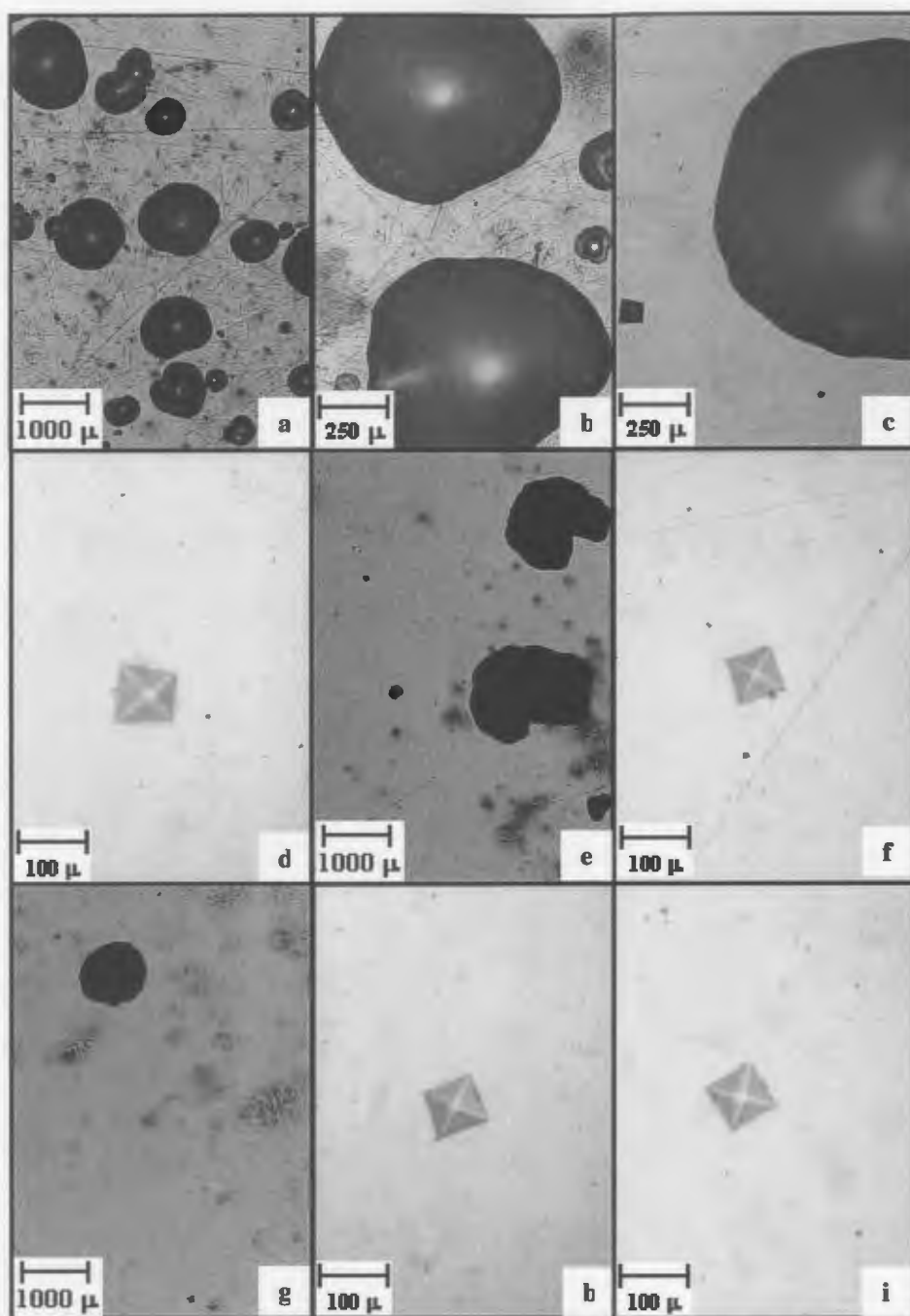


Figure 21. Pictures of samples after potentiostatic polarization using solution 4 (deaerated).
 (a) 1.1 V (b) 1.1 V (c) 1.0 V (d) 1.0 V (e) 0.9 V (f) 0.9 V (g) 0.8 V (h) 0.8 V (i) 0.7V

Table 10. Pit classification for samples potentiostatically polarized using solution 4 (deaerated)

Applied Potential (Volts)	Type of Pit
1.1	B _{BPHU}
1.0	B _{BDLU}
0.9	D _{BDLU}
0.8	B _{BDLU}
0.7	N/A

The charge associated with the edge dissolution was determined by plotting the anodic current as a function of time on a linear scale as shown in figure 22. From the plot, one can see that the current begins to fluctuate at the onset of edge dissolution. This was validated by stopping a polarization test at the onset of the current fluctuation and examining the surface. The total charge passed up to the onset of the current fluctuation was used in the plot shown above in figure 23. Refer to appendix G for a comparative picture of all samples including the sample used to determine the onset of edge dissolution. The polarization potential for this sample was 0.7 V.

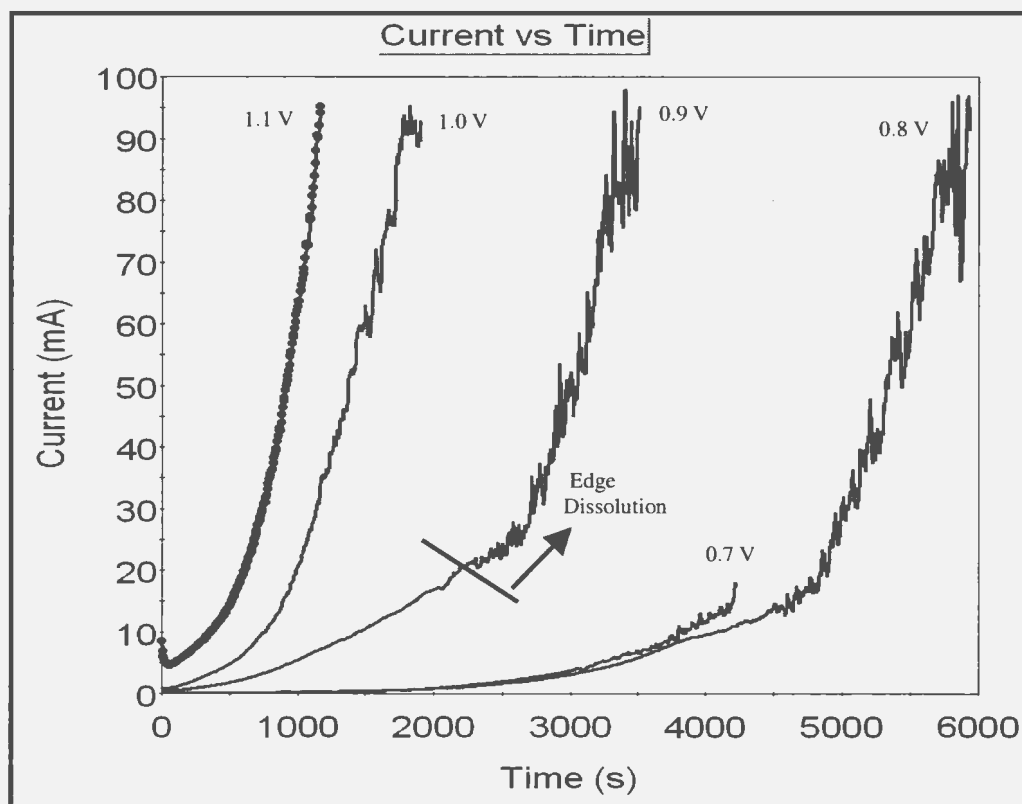


Figure 22. Plot of corrosion current as a function of time for test solutions 4 (deaerated)

If the amount of dissolution pertaining to the ring formed at the sample/washer interface is not included in the calculation of total charge, the revised plot will show an increase in the total charge transferred with increasing potential as expected. Figure 23 shows the revised plot of total charge vs test solution for the respective polarization potentials.

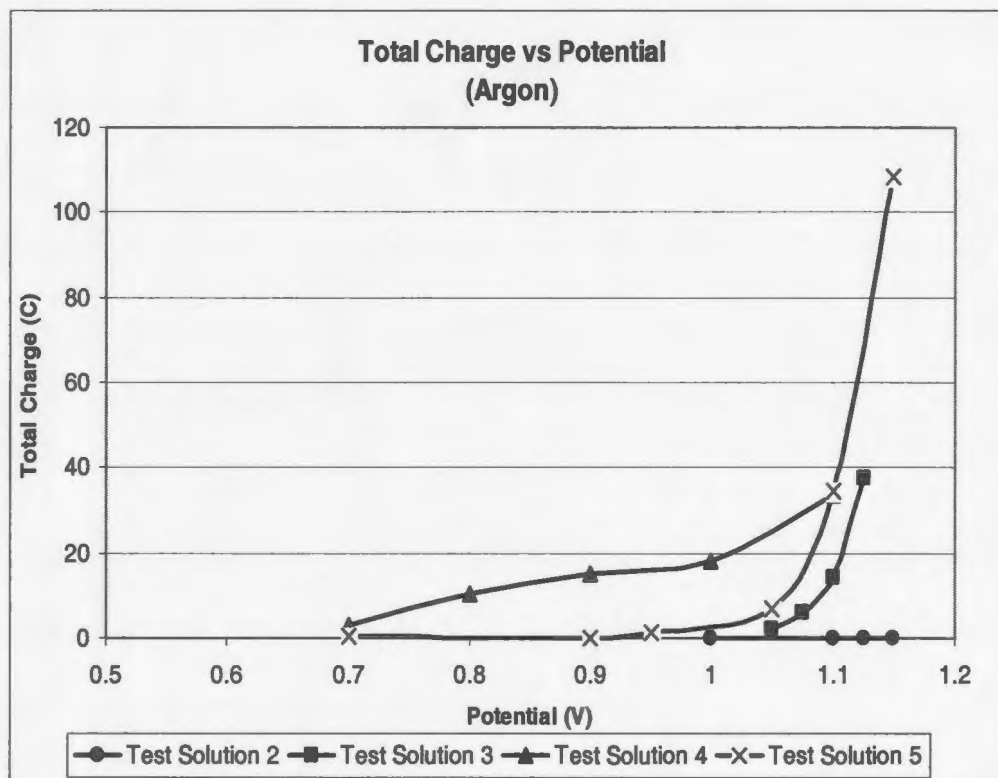


Figure 23. Revised plot of total charge as a function of applied potential for solutions 2, 3, 4 and 5 (deaerated)

Solution 5

Pitting was only observed on the samples that were polarized above 1.05 V as indicated by figure 24. In addition to pitting, the entire surface of the samples became etched along grain boundaries and the intensity of the etching decreased with potential until 1.05 V, below which, no etching was observed. No localized etching was observed on the samples, not even at the outermost edge at the sample/washer interface. However, orange deposits (iron oxide) were present on all samples with the highest density occurring at potential between 0.9 V and 1.05 V. As the potential was increased above 1.05 and decreased below 0.9 V the density decreased. When the applied potential was 1.05 V, slightly dome shaped, circular structures appeared on the surface scattered intermittently among the orange deposits.

The indentation was visible on all samples, therefore did not contribute to the development of pits. However, a pit on the sample polarized at 1.1 V nucleated near the indentation, as a result a portion of it was consumed.

A summary of pits found on the samples is presented in Table 11.

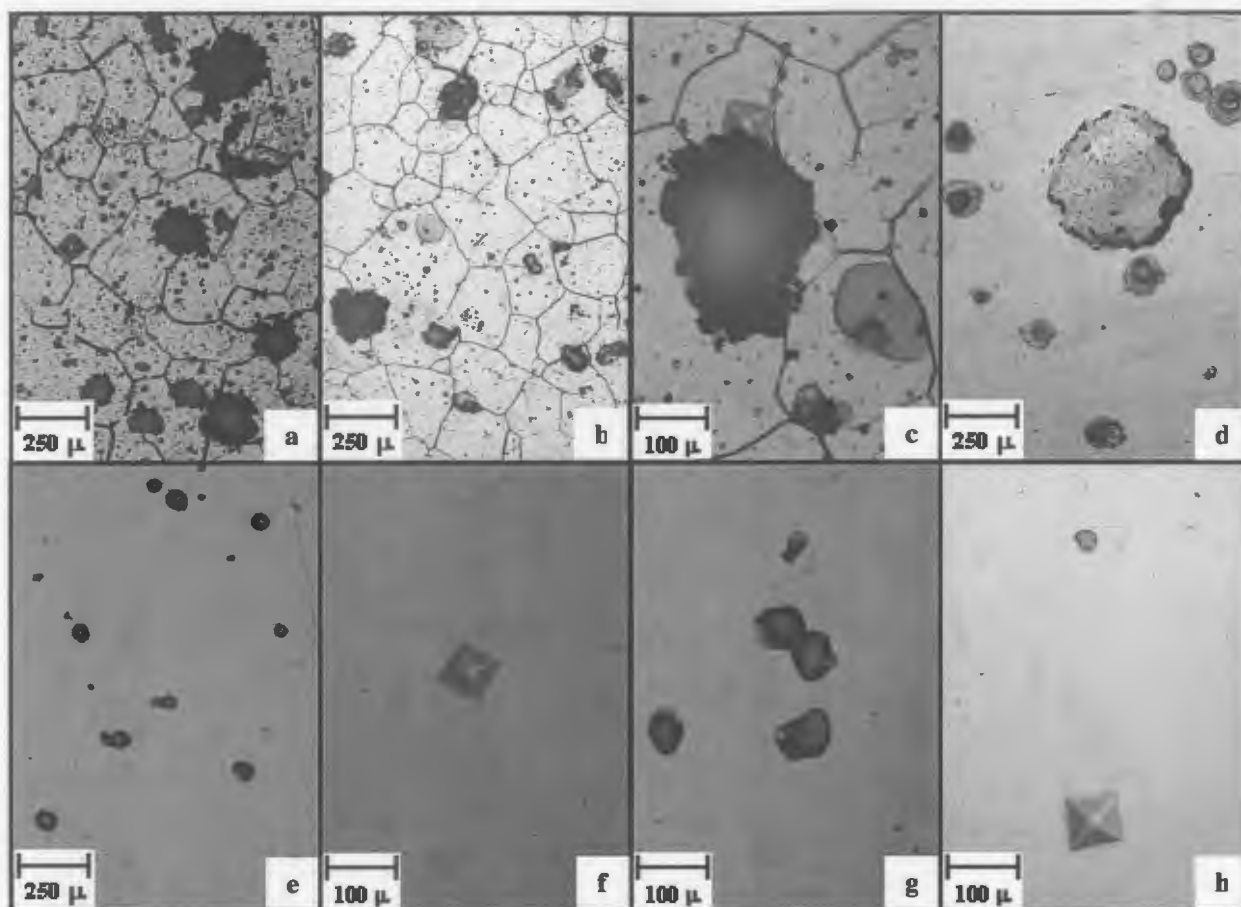


Figure 24. Pictures of samples after potentiostatic polarization using solution 5 (deaerated).
 (a) 1.15 V (b) 1.1 V (c) 1.1 V (d) 1.05 V (e) 0.95 V (f) 0.9 V (g) 0.9 V (h) 0.7 V

Table 11. Pit classification for samples potentiostatically polarized using solution 5 (deaerated)

Applied Potential (Volts)	Type of Pit
1.15	E_{SEHU}
1.1	E_{SEHU}
1.05	C_{BELU}
0.95	N/A
0.9	N/A
0.7	N/A

5.2.2 Oxygen

The results for the samples polarized in aerated solutions are presented below in Figures 25-28.

5.2.2.1 Polarization Curves

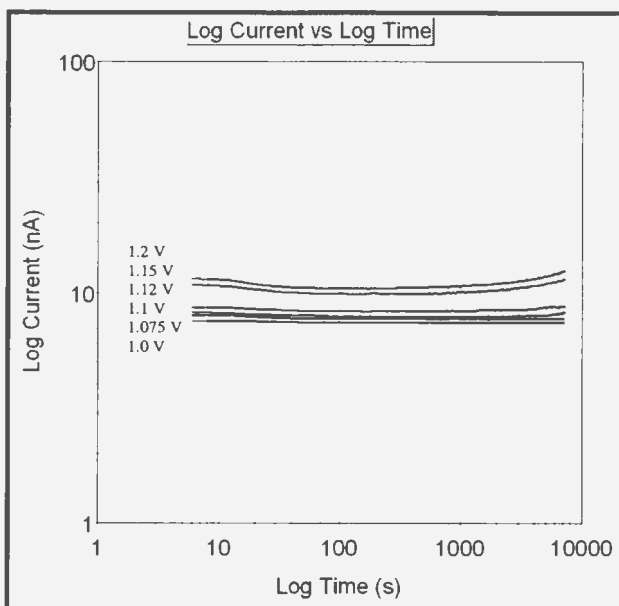


Figure 25. Potentiostatic curves for solution 2 (aerated)

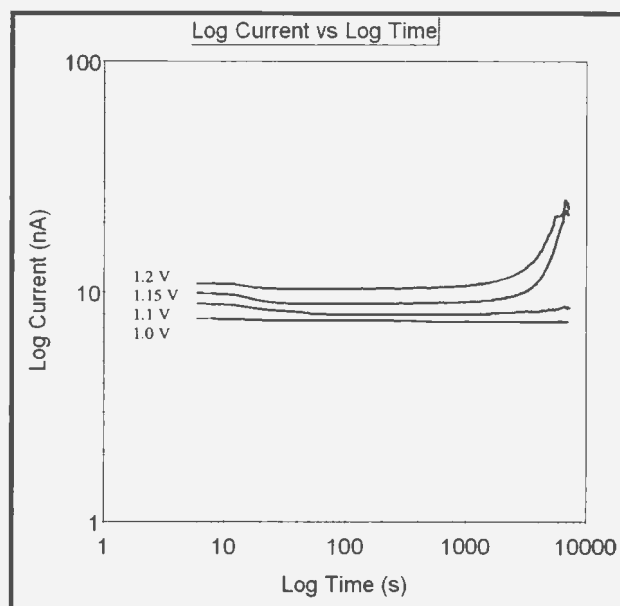


Figure 26. Potentiostatic curves for solution 3 (aerated)

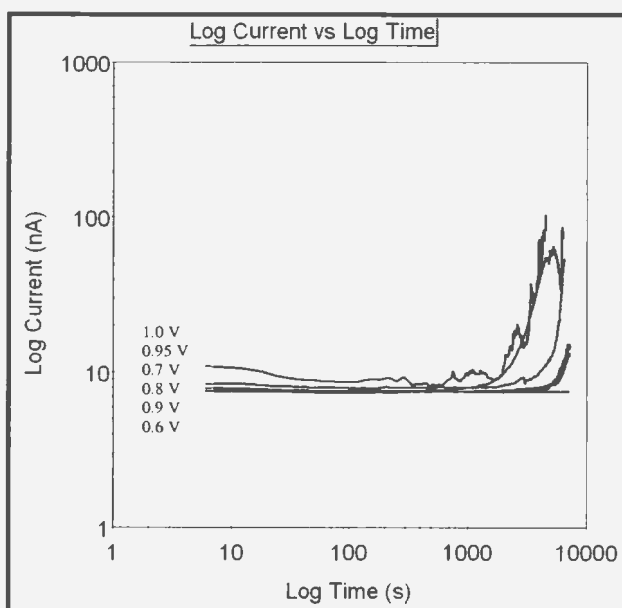


Figure 27. Potentiostatic curves for solution 4 (aerated)

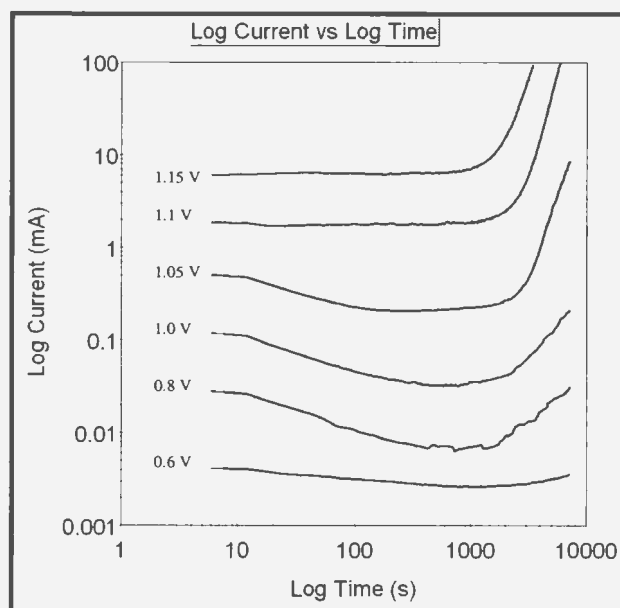


Figure 28. Potentiostatic curves for solution 5 (aerated)

Again, solutions 2 and 3 show a distinct increase in the incubation time as the applied potential is incrementally decreased, until the potential is below the true pitting potential, at which point the current remains constant. Solutions 4 and 5 follow the same general trend, however, some tests show the opposite effect. For example, a shorter incubation time resulted when the applied potential was 0.7 V as compared with 0.8 V and 0.9 V for solution 4. With regard to solution 5, the incubation time decreased as the potential was lowered from 1.15 V to 1.1 V. Below 1.1 V however the respective incubation increased with decreasing potential. All current values associated with the polarization tests are in the nA range except for those associated with solution 5 which yield current values in the mA range. The specific current range associated with each test solution is given below in Table 12.

Table 12. Current range for samples polarized potentiostatically (aerated)

Test Solution	Min. Current Value	Max. Current Value	Current Range
2	7.4 nA	12.43 nA	4.73 nA
3	7.4 nA	25.16 nA	17.76 nA
4	7.5 nA	104 nA	96.50 nA
5	3.6 μ A	97.8 mA	97.79 mA

Figure 29 shows how the maximum slope of each curve changed with applied potential for solutions 2, 3, 4 and 5. As outlined above, if hemispherical pits develop on the surface, the slope of the curve should be 2.

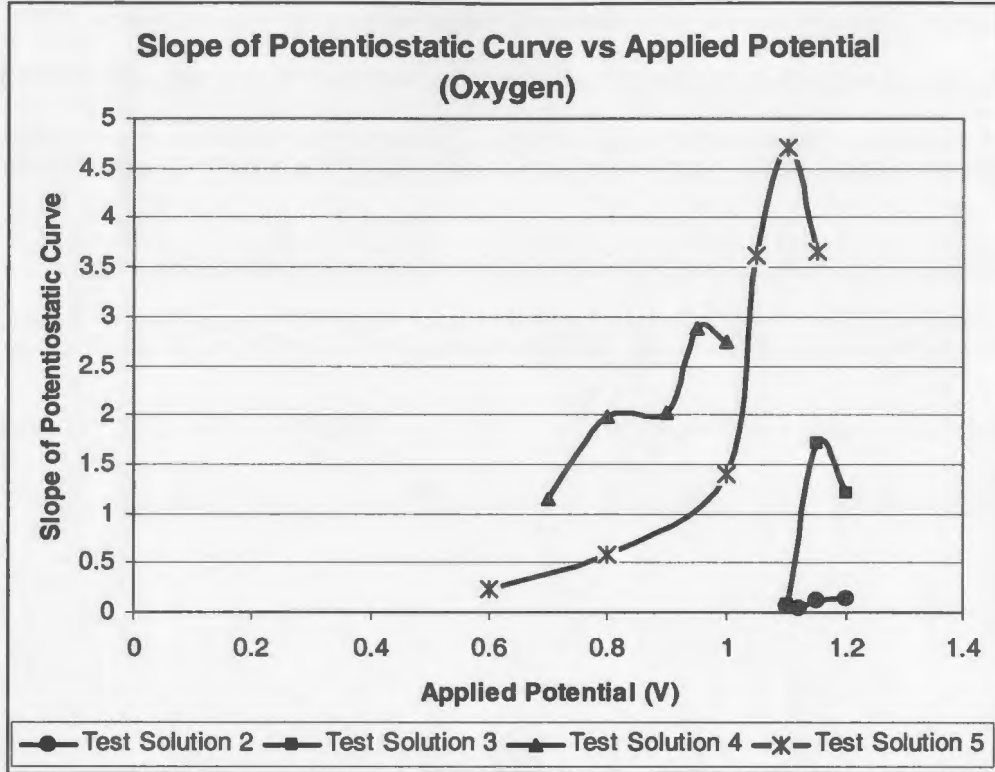


Figure 29. Slope of the potentiostatic curves as a function of the applied potential for solutions 2, 3, 4 and 5 (aerated).

From the plot (Figure 29) one can see that the slope of the curves tend to increase with applied potential.

5.2.2.2 Pitting Potential

The results obtained when the applied potential was plotted against the inverse of each respective incubation time are shown below in Figure 30. Again, a line of best fit was drawn through the points and extrapolated until it intersected the y-axis and this value was taken as the true pitting potential of the metal/solution combination. All five

solutions produced good results, particularly solutions 4 and 5 when compared to the results obtained with deaerated solutions.

From the data points associated with solution 5, two different trend lines can be fitted as was the case when the solution was deaerated. Therefore, two lines of best fit were drawn through the data until they intersected the y-axis representing the two potentials (stable and metastable). The metastable pitting potential for solution 5 is approximately 0.55 V (Figure 30). The pitting potentials associated with stable pitting are presented in Figure 31.

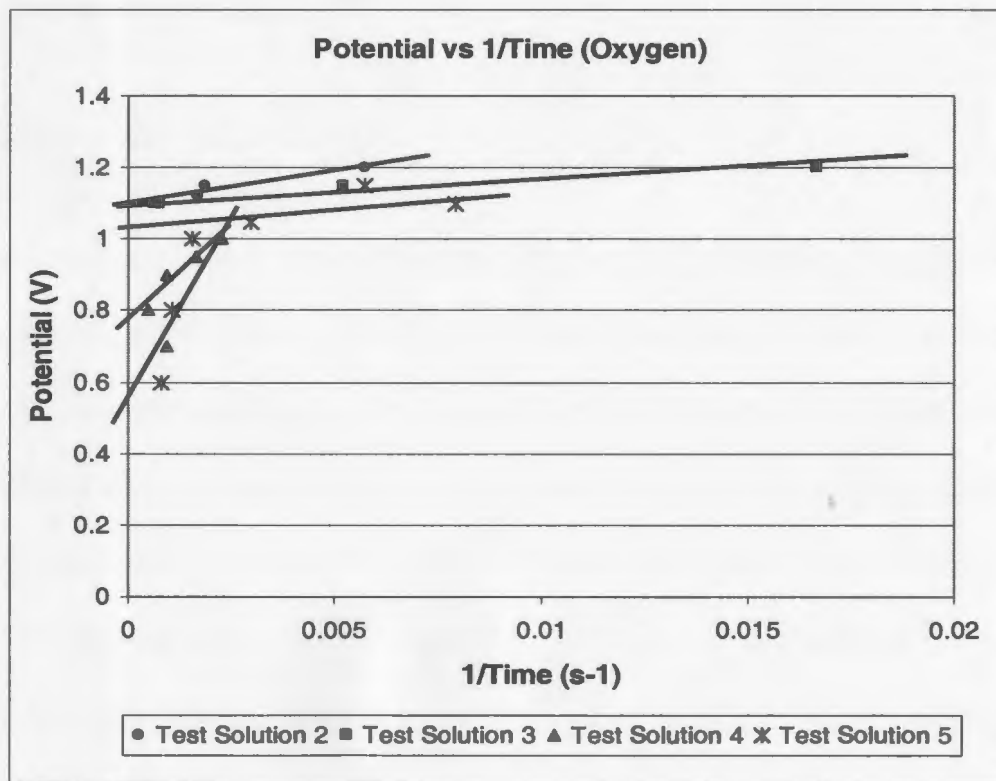


Figure 30. Plot of applied potential vs inverse of the incubation time for solutions 2, 3, 4 and 5 (aerated).

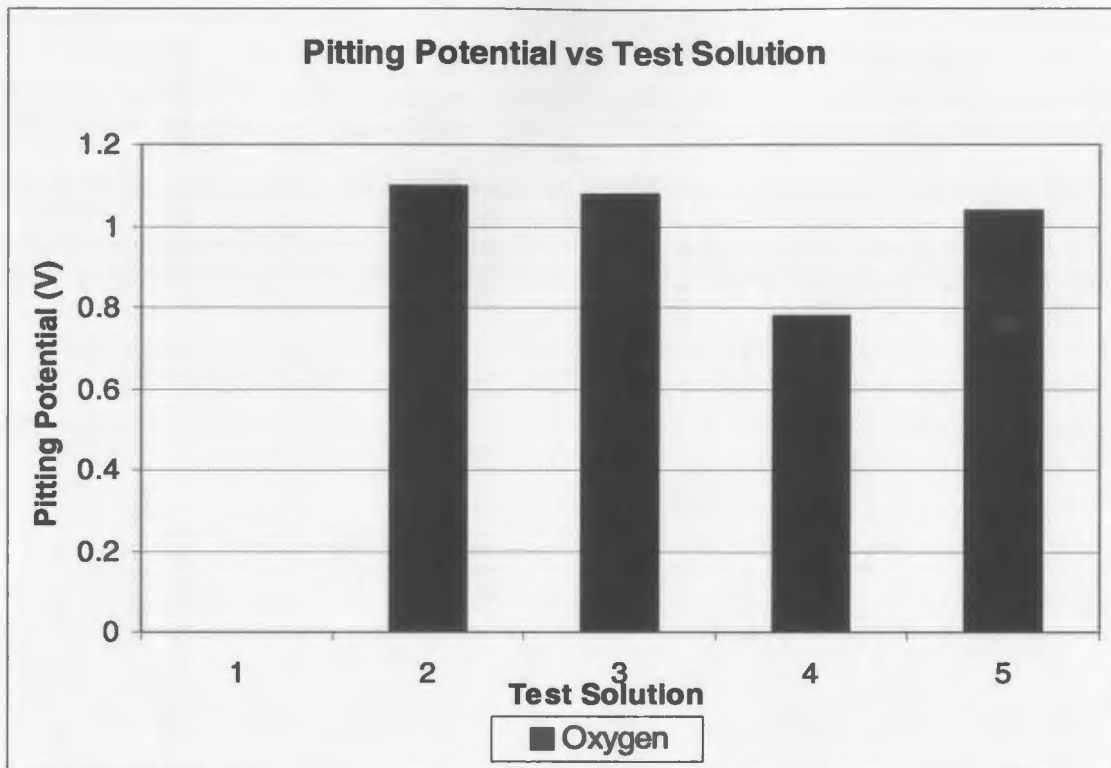


Figure 31. Pitting potential as a function of test solution for potentiostatic polarization tests (aerated)

5.2.2.3 Anodic Dissolution

As discussed in a previous section, the total charge transferred during a polarization test is directly proportional to the amount of anodic dissolution according to Eq. 47. A plot of the total charge passed as a function of the applied potential is shown in Figure 32.

From the plot one can see that the total charge increases with potential and therefore the total anodic dissolution will increase with applied potential. In addition, one would expect the total dissolution of a sample polarized at 1.1 V in solution 5 to be 100 fold greater than a sample polarized in solution 2, 3 or 4. However, this is not the case as can be shown by analyzing the surface of all samples tested.

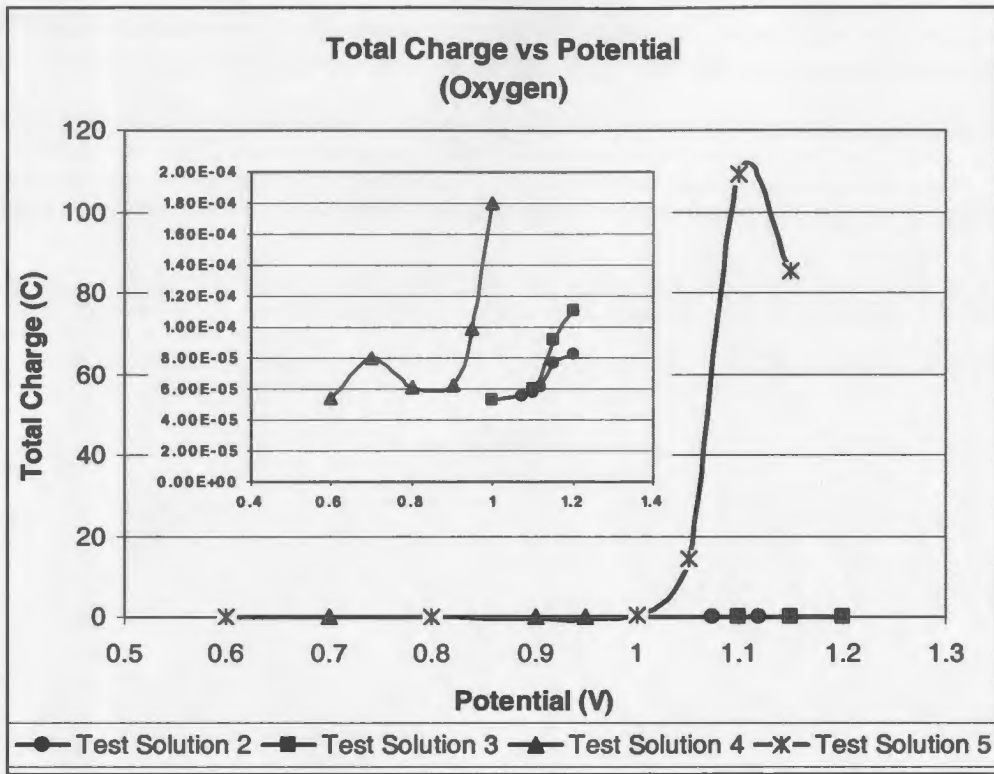


Figure 32. Plot of total charge as a function of applied potential for solutions 2, 3, 4 and 5 (aerated)

5.2.2.4 Surface Analysis

Solution 2

Only type A pits were observed on the samples polarized using solution 2 as summarized in Table 13. The density of the etch pits decreased with decreasing potential as did the intensity of the grain boundary etching as shown in Figure 33. The decrease in potential also resulted in some localized etching near the sample/washer interface. The higher potential tests show the presence of inclusions along grain boundaries, however they are irrelevant in the development of the small etch pits which can be see distributed

uniformly over the entire surface. The microhardness indentation can also be seen on all of the samples and did not show any signs of contributing to the pit development.

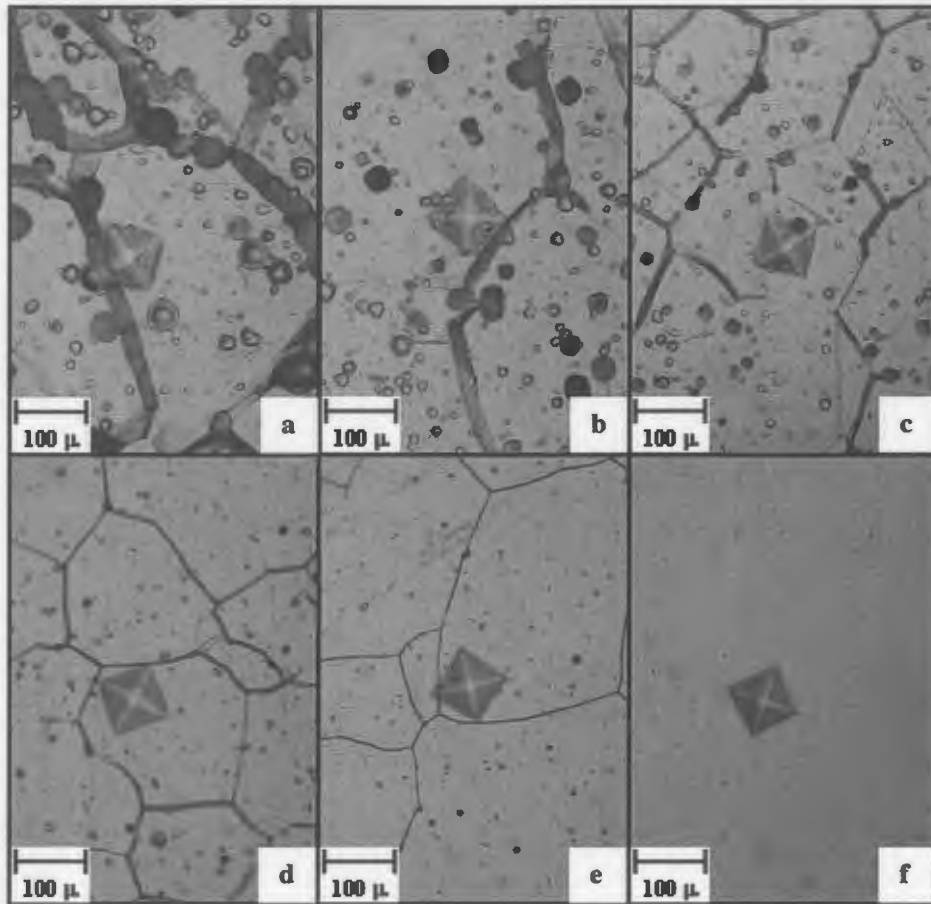


Figure 33. Pictures of samples after potentiostatic polarization using solution 2 (aerated). (a) 1.2 V (b) 1.15 V (c) 1.12 V (d) 1.1 V (e) 1.075 V (f) 1.0 V

Table 13. Pit classification for samples potentiostatically polarized using solution 2 (aerated)

Applied Potential (V)	Type of Pit
1.2	A _H
1.15	A _H
1.12	A _H
1.1	A _M
1.075	A _L

Solution 3

The surface analysis of samples polarized using solution 3 show similar results to the samples polarized using solution 2. Type A pits were present on the surface when polarized at higher potentials but became less visible as the potential was decreased. At higher potentials the surface etching was mainly associated with the grain boundaries but became focused on the actual grains at lower potentials. No localized etching of any kind was observed near the edge of the samples at the sample/washer interface. At potentials greater than 1.1 V, larger pits were observed on the surface as indicated in the pictures (Figure 34) and summarized in Table 14. The larger pits appeared to develop by the combination of several smaller pits resulting in irregular shapes and fuzzy edges. The microhardness indentation was only visible on the samples polarized below 1.1 V, and from the pictures one can see they are unaffected with regard to pitting, however suffered extensive etching at 1.0 V. Above 1.1 V, the surface was covered in pits therefore the microhardness indentation either served as a nucleation site or became consumed during pit development.

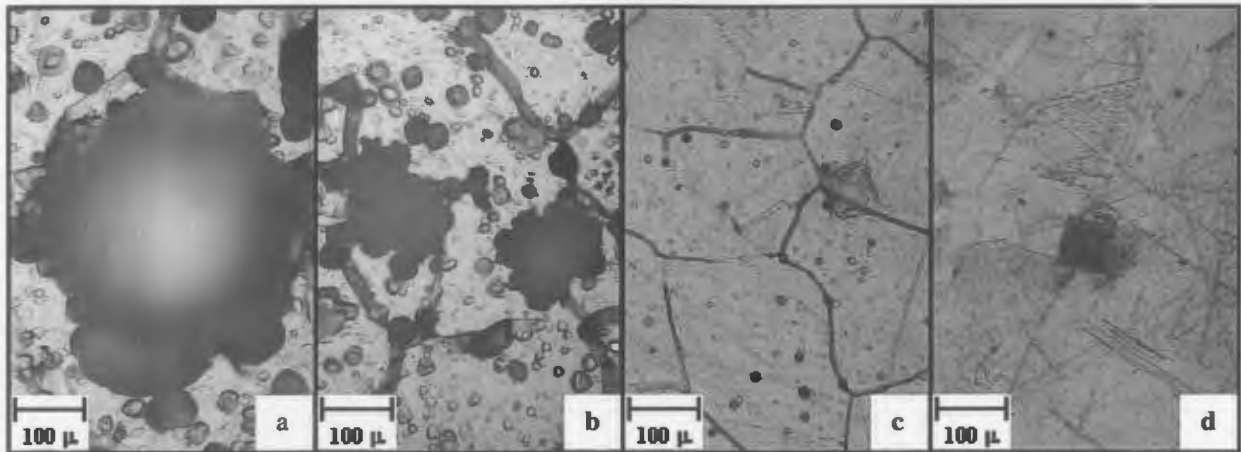


Figure 34. Pictures of samples after potentiostatic polarization using solution 3 (aerated).
 (a) 1.2 V (b) 1.15 V (c) 1.1 V (d) 1.0 V

Table 14. Pit classification for samples potentiostatically polarized using solution 3 (aerated)

Applied Potential (V)	Type of Pit
1.2	A_H, E_{BPHU}
1.15	A_H, E_{SPLU}
1.1	A_L
1.0	N/A

Solution 4

Pits were visible on all samples polarized above 0.8 V as can be seen in Figure 35 and are summarized below in Table 15. The surface between pits suffered from uniform grain etching and the intensity of such etching increased as the applied potential decreased. The sample polarized at 1.0 V resulted in a highly pitted surface with no visible etching; instead, the surface between pits suffered uniform dissolution and appeared polished. The microhardness indentation on the surface was only visible on samples polarized at

potentials below 0.7 V. Both large circular pits and small irregular pits were found on the surfaces polarized above 0.8V

In addition to pitting, some localized anodic dissolution was observed near the sample/washer interface on the samples polarized at 0.7 V and 0.8 V respectively. Refer to Appendix G for a comparative picture of samples showing the localized dissolution at the sample/washer interface.

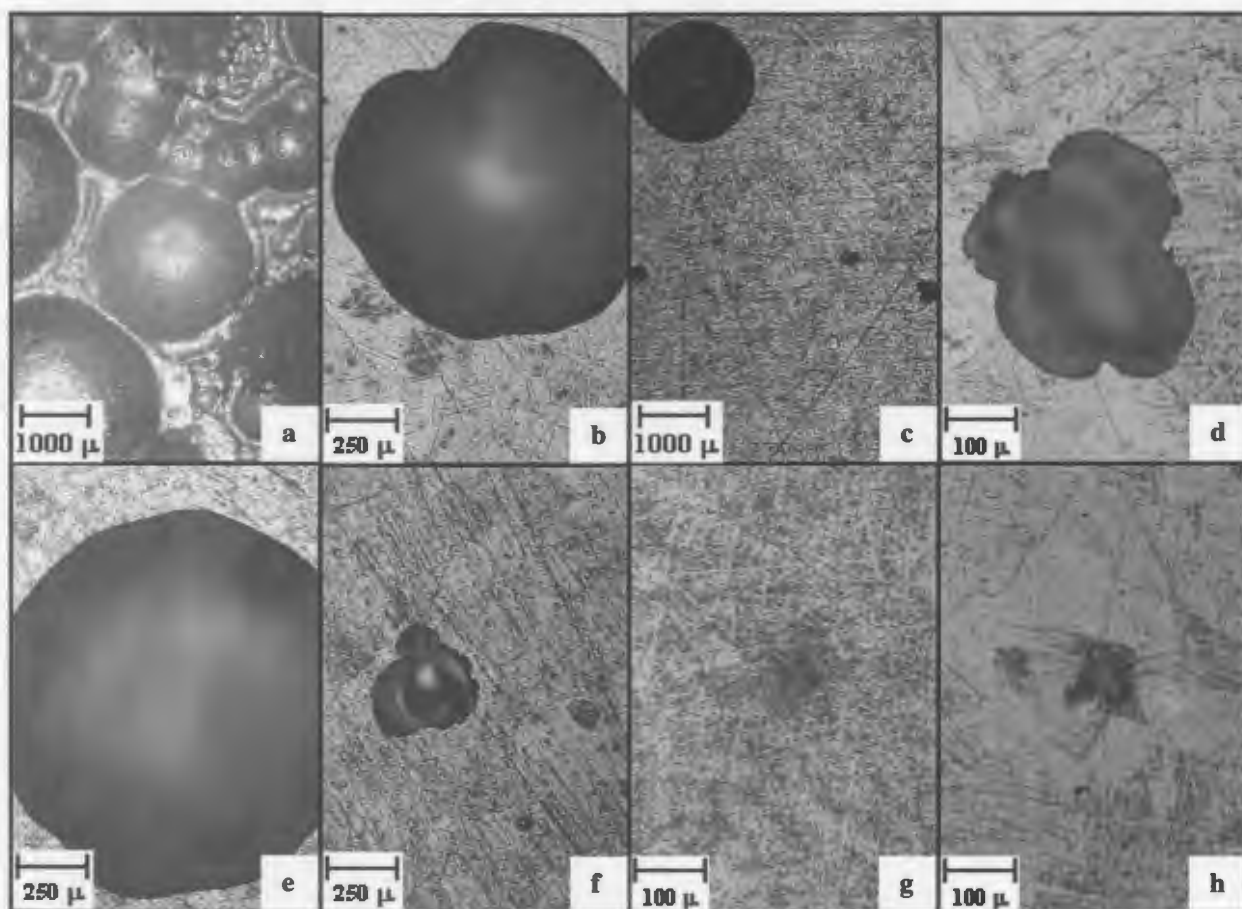


Figure 35. Pictures of samples after potentiostatic polarization using solution 4 (aerated). (a) 1.0 V (b) 0.95 V (c) 0.9 V (d) 0.9 V (e) 0.8 V (f) 0.8V (g) 0.7 V (h) 0.6 V

Table 15. Pit classification for samples potentiostatically polarized using solution 4 (aerated)

Applied Potential (Volts)	Type of Pit
1.0	B _{BPHU}
0.95	B _{BDHU}
0.9	B _{BDLU} , D _{SPLU}
0.8	B _{BDLU} (One Pit)
0.7	N/A
0.6	N/A

Solution 5

Pitting was only observed on the samples that were polarized at 0.95V and 1.0 V. In addition to pitting, the entire surface of the sample became etched along grain boundaries, and the intensity of the etching decreased with potential until 0.8 V, below which, no etching was observed. No localized etching was observed near the edge of the samples for any potential range. Orange deposits (iron oxide) were present on all samples with the highest density occurring at potential between 0.8 V and 0.95 V. As the potential was increased above 0.95 and decreased below 0.8 V the density decreased. Shallow pits developed uniformly over the entire surface of the sample having relatively large diameters and the bottoms showing grain boundary etching when the applied potential was 0.8 V. The shallow etched pits on the surface were scattered intermittently among the orange deposits.

The microhardness indentation on the surface was visible on all samples, except for the sample polarized at 1.0 V, indicating it served as a nucleation or became consumed during pit growth.

Pictures of the samples are shown in Figure 36 and a summary of pits found on the samples is presented in Table 16.

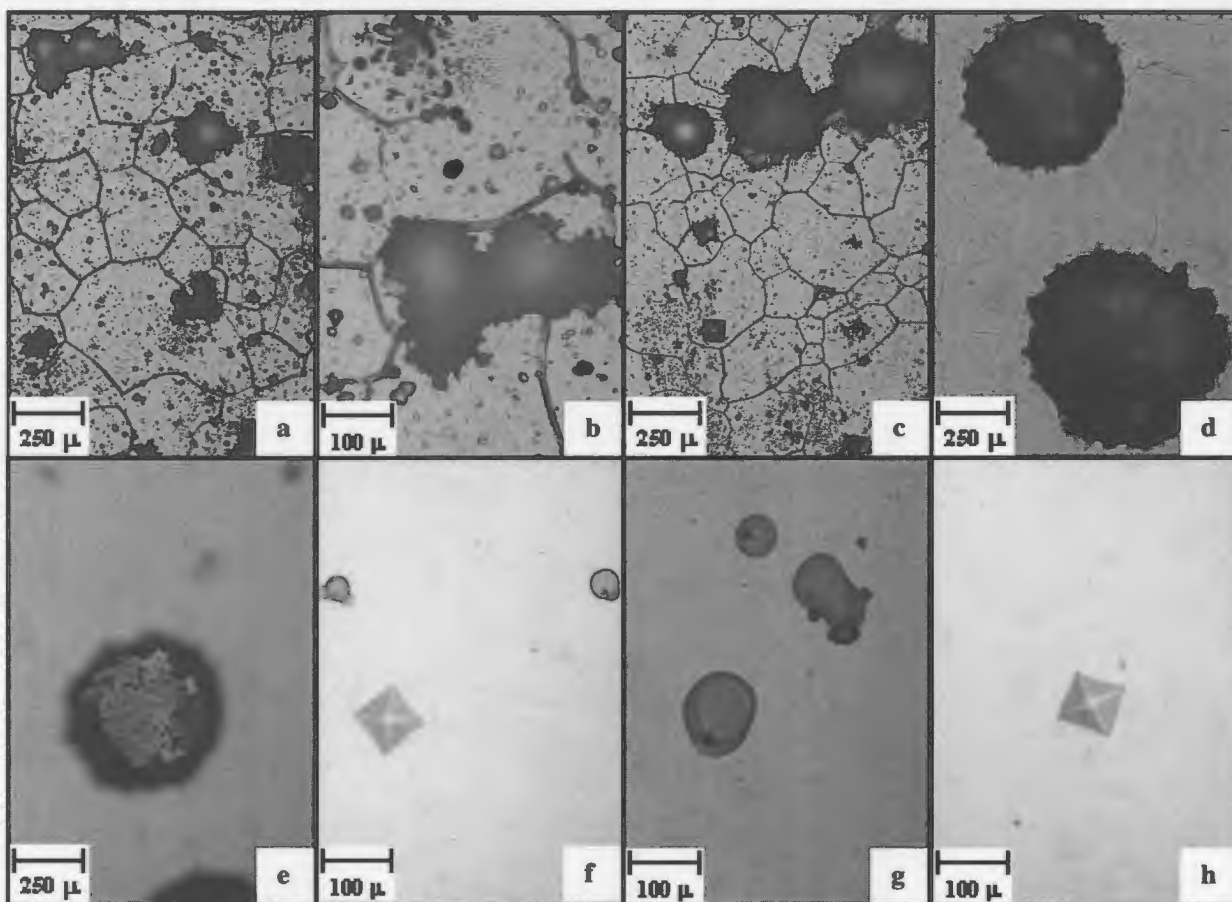


Figure 36. Pictures of samples after potentiostatic polarization using solution 5 (aerated). (a) 1.0 V (b) 1.0 V (c) 0.95 V (d) 0.8 V (e) 0.8 V (f) 0.7V (g) 0.7 V (h) 0.6 V

Table 16. Pit classification for samples potentiostatically polarized using solution 5 (aerated)

Applied Potential (Volts)	Type of Pit
1.15	E _{SEHU}
1.1	C _{BPLE} , E _{SPLU}
1.05	C _{BDLU}
1.0	N/A
0.8	N/A
0.6	N/A

5.3 Scanning Electron Microscopy

A scanning electron microscope (SEM) was used to investigate various pit nucleation sites on the surface of the samples. In addition to the SEM micrographs, energy dispersive x-ray spectroscopy (EDS) was used to identify all elements participating in pit growth. SEM micrographs of pit growth were taken using secondary electrons and are displayed in Figures 37-43 below. Figure 37 shows a sulfide inclusion with a pit cover during initial stage of development. Figures 38 and 39 show pits at later stages in the development where the cover is starting to rupture due to the build up of corrosion product as a result of anodic dissolution. The letters on each picture indicate the locations analyzed using EDS and the corresponding spectra are presented in Appendix H.



Figure 37. SEM micrograph of a sample polarized at 0.6 V in solution 5 (aerated)

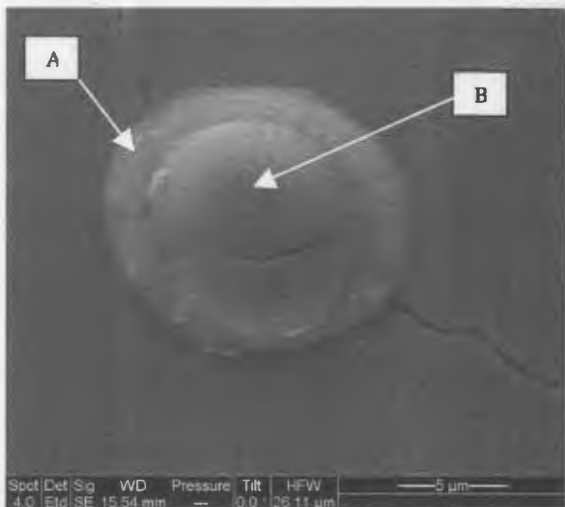


Figure 38. SEM micrograph of a sample polarized at 1.05 V in solution 5 (aerated)-1



Figure 39. SEM micrograph of a sample polarized at 1.05 V in solution 5 (aerated)-2

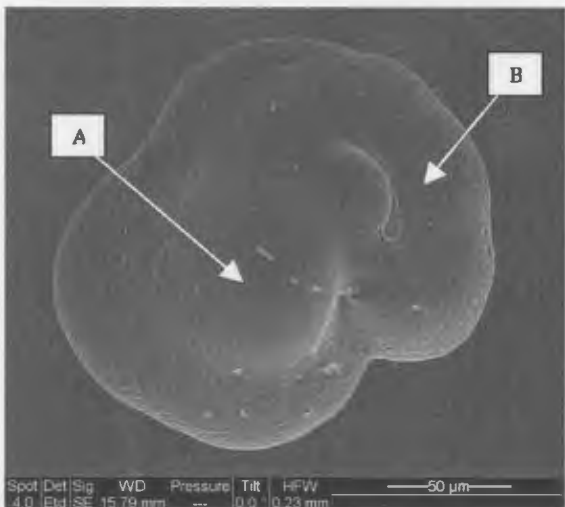


Figure 40. SEM micrograph of a sample polarized at 0.95 V in solution 4 (aerated)-1

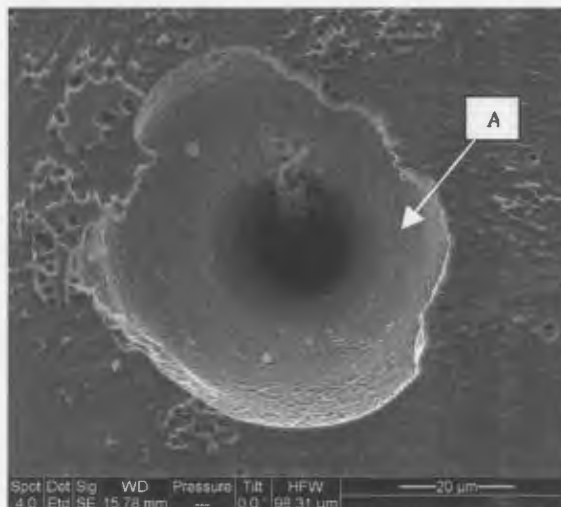


Figure 41. SEM micrograph of a sample polarized at 0.95 V in solution 4 (aerated)-2



Figure 42. SEM micrograph of a sample polarized at 1.1 V in solution 4 (deaerated)

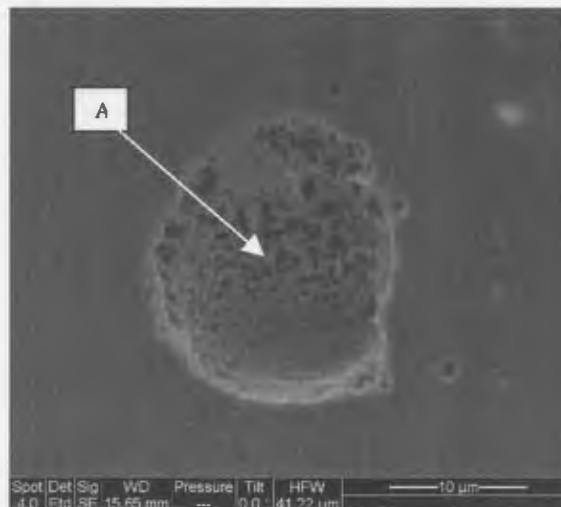


Figure 43. SEM micrograph of a sample polarized at 1.1 V in solution 4 (deaerated)

6.0 Discussion

6.1 Comparison of Polarization Techniques

The single most important parameter associated with potentiodynamic polarization is the rate at which the applied voltage is incrementally increased, known as the scan rate. If the scan rate is too high or too low, the pitting potential associated with the polarization curve would be greater than the true pitting potential of the metal/electrolyte combination. The idea can be best understood by modeling the surface as a resistor and capacitor in parallel. Ideally, the scan rate should be slow enough to ensure the capacitance remains fully charged and the current/voltage relationship at any given potential reflects the interfacial corrosion process only. If this is not the case, some of the current being generated would reflect changing the surface capacitance in addition to the corrosion process, yielding higher values for E_{pit} [66]. Szklarska-Smialowska and Janik-Czachor [37] concluded the high rates of potential change may give noble E_{pit} values, due to the long induction time for a pit to form. On the other hand, too slow a rate of potential change may also give more noble E_{pit} values, due to the development and amelioration of the passive layer.

In addition to the pitting potential, some researchers have found that the pit density was much higher on samples polarized potentiodynamically as compared with those polarized potentiostatically. According to Ryan et al. [67] the reason being is that the Cr-based passive film forms at a potential lower than that required to sustain pitting. During the

scan, the film has time to relax and possibly obscure some of the pit initiation sites. Also, pits which are initiated at low potentials consume some of the initiation site as they grow reducing the overall density.

This problem is alleviated when samples are subjected to potentiostatic tests, whereby a discrete potential is applied to the sample and the corresponding current is recorded as a function of time. During the potentiostatic tests, the passive film has no time to relax and as a result all possible initiation sites are simultaneously nucleated [67]. Alonso-Falleiros et al. [64] as well as Pulino-Sagradi and Alonso-Falleiros [65] concluded that the potentiostatic polarization technique is a more reliable technique for determining the true pitting potential for a particular metal/electrolyte combination.

From the current work one can see that there is a distinct difference in the pitting potentials obtained from the potentiodynamic test when compared to those obtained using the potentiostatic test, particularly when chloride ions were added to the electrolyte.

6.2 Mixed Potential Theory

When a particular system involves two or more possible oxidation-reduction reactions the free corrosion potential and corrosion rate can be determined by applying the two basic rules of mixed potential theory [68].

1. All electrochemical corrosion processes are composed of one or more anodic reactions and one or more cathodic reactions.
2. The electrons released at the anodic sites must equal the electrons consumption at the cathodic sites. That is, the total oxidation must equal the total reduction.

If we consider the situation of iron in aerated water, the oxidation and reduction reactions are as follows:



With the combined knowledge of standard reduction potential E_o , exchange current density i_o , and the Tafel slope β for the associated reactions as they pertain to a given system, one can draw the overpotential curves corresponding to the Tafel equation of the form.

$$E = E_o + \beta \log \frac{i}{i_o} \quad (51)$$

The intersection of the respective curves will correspond to the free corrosion potential (E_{corr}) for the system and the corresponding current value represents the exchange current for the system. The intersection point of the two curves, E_{corr} , will lie somewhere between the standard reduction potential of the oxidation reaction and the reduction reaction. The exact value will depend on the slope of the respective curves which in turn depends on the specific reaction rates for the given metal/electrolyte combination.

Considering the current work, the free corrosion potential associated with a particular metal/electrolyte was influenced by the ions in solutions and whether or not the solution was aerated. The standard electrode potentials for reaction associated with the current work are given below in Table 17.

Table 17. Standard reduction potentials

Electrode Reaction	E_o (V _{Ag/AgCl})
$\text{NiO}_2 + 2\text{H}^+ = \text{Ni}^{2+} + \text{H}_2\text{O}$	1.793
$\text{O}_2 + 4\text{H}^+ + 4\text{e}^- = 2\text{H}_2\text{O}$	1.23
$\text{Fe}^{3+} + \text{e}^- = \text{Fe}^{2+}$	0.771
$\text{H}^+ + \text{e}^- = \text{H}_2$	0.00
$\text{Ni}^{2+} + 2\text{e}^- = \text{Ni}$	-0.257
$\text{Fe}^{2+} + 2\text{e}^- = \text{Fe}$	-0.44
$\text{Cr}^{3+} + 3\text{e}^- = \text{Cr}$	-0.744

If the exchange current density and Tafel slopes were known for the above reactions as they pertain to stainless in sulfuric acid, one could draw the over potential curves for each reaction and theoretically determine E_{corr} . However, this specific information can only be obtained through experimentation.

If we consider solution 1, the free corrosion potential for the aerated system is approximately 0.5 V more positive than the deaerated solution. Since dissolved oxygen is the only variable, the oxygen reduction reaction must be responsible for the increase in E_{corr} for the aerated solution. An increase in free corrosion potential of 0.45 V was

obtained when 304 stainless steel was polarized in aerated solution of 1N H₂SO₄ when compared with a deaerated solution as illustrated in the literature [5].

The free corrosion potential for solution 2, when aerated, is even higher than the value for solution 1, 0.93 V as compared with 0.131V, whereas the value for the deaerated solution only experiences a small increase -0.423 V to -0.396 V. The difference in solution 1 and solution 2 is in the addition of nickel ions. Again, the amount of dissolved oxygen must be responsible for the increase in the free corrosion potential of the aerated solution. One explanation is that the dissolved oxygen reacts with the nickel ions in solution to form nickel oxide. From Table 17, the standard reduction potential for nickel oxide in an acid media is 1.793 V and therefore will shift the overall potential of the electrochemical cell in the positive direction. Again the precise value depends on the exchange current density and the Tafel slope for that reaction on a stainless steel substrate.

With the addition of chloride ions, in solutions 3 and 4, the free corrosion potential shifted in the active direction significantly when aerated, but remained relatively unaffected when the solutions were deaerated. One explanation is that the chloride ions react with the available hydrogen ions in solution eliminating the reduction of nickel oxide. In addition, the chloride ions become chemisorbed to the surface of the metal as discussed in a previous chapter. The change in the interfacial conditions of the metal and the electrolyte will influence the reduction ability of the ions in the solution.

The addition of ferric ions to the electrolyte in solution 5 resulted in the free corrosion potential shifting in the noble direction for both the aerated and deaerated solutions. The corresponding free corrosion potential of solution 5, containing both chloride ions and ferric ions is more noble than the value obtained with solution 1, without chloride ions. The positive shift in potential is a result of the reduction of Fe^{3+} to Fe^{2+} as indicated by the reaction in Table 17. The reaction involves accepting an electron from the metal surface, promoting the anodic dissolution of the metal resulting in the formation of a protective metal oxide as discussed in a previous chapter.

6.3 Pit Development and Growth

From the surface analysis of the samples after polarization, it is clear that pits initially develop with a cover to ensure the critical concentration of metal ions is maintained. From the SEM micrographs and EDS spectra it is also clear that chloride ions do in fact penetrate the passive film and combine with the metal ions. The micrographs also show that the nature of the cover depends on the electrolyte and amount of dissolved oxygen. The cover formed in solution 5, consisted of a Fe-Cr oxide which appeared to be very tenacious with large cracks developing prior to complete rupture. In the absence of iron ions, the cover seemed to be much thinner and in some cases perforated allowing diffusion of ions during pit growth.

A cross-sectional view of developed pits after potentiostatic polarization show they are not hemispherical as is assumed for their initial growth. The average width-to-depth ratio is about 6 showing the pits are saucer shaped (Figure 44). Similar findings were reported by Mankowski and Szklarska-Smialowska [30] who found that pits initially developed isotropically in the form of a hemisphere, but after a certain time settled into the shape of a spherical cup. They found that the broadening of the pits occurred at a faster rate than the deepening due to the unequal distribution of chloride ions in the pits, with the lower concentration near the edges. As a consequence, the local anodic current density is higher there, and as a result, broadening occurs at a faster rate than deepening.

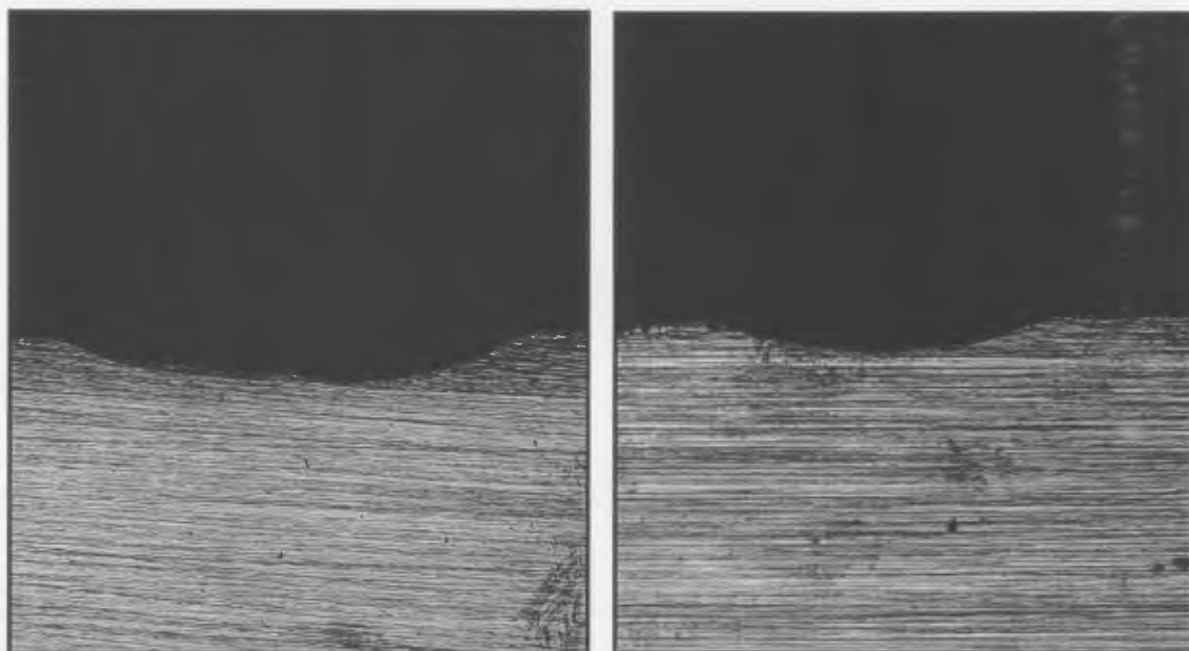


Figure 44. Cross-section view of pits

6.3.1 Brighten and Etching Dissolution

According to Sato [34] there are two modes of metal dissolution in concentrated aqueous solutions:

1. Active or etching dissolution which takes place on the bare metal at relatively less noble potentials
2. Transpassive or brightening dissolution which occurs on the metal surface with an anion-contaminated oxide or salt film at relatively noble potentials.

The critical aggressive anion concentration at which the transition from etching dissolution to brightening dissolution occurs is independent of potential. As long as the pit surface is in the brightening dissolution state, there is no possibility for repassivation.

If the local electrolyte potential composition at the breakdown site changes such that the hydrogen ion concentration exceeds its critical value for depassivation before the aggressive anion (Cl^-) reaches its critical value, the film breakdown site grows into an etching pit. The opposite is true if the aggressive anion concentration is reached first.

Hoar et al. [20] also reported that pits formed on stainless steel became brighter with increasing chloride concentration and applied potential. They suggest that there is a compact solid film of high cation conductivity on the pit anode, possibly consisting of chloride and oxide anions.

With regard to the current work, similar findings were reported in that etched pits were characteristic of lower applied potentials. As the potential approached the pitting potential the pit bottoms became dull or severely etched showing grain boundaries, above E_{pit} the pit bottoms were polished. However, pits formed on the samples polarized in solution 5, aerated and deaerated, resulted in the development of etch pits even at the higher applied potentials. One possible explanation for this occurrence is that due to the rapid anodic dissolution resulting from the reduction of the ferric ions, a thick metal oxide is formed on the surface of the metal. This protective film reduces the local concentration of aggressive anions by slowing the diffusion of chloride ions from the bulk electrolyte to the local pit environment. EDS of the pit covers formed on the samples polarized in solution 5 show chlorine is indeed present in the cover of the developing pits. Refer to Appendix H for the EDS spectra.

The final aspect of pit development pertaining to the present work is the current values associated with the anodic dissolution for a given sample. From the surface analysis, the anodic dissolution associated with samples polarized in solution 4 are very similar when aerated as well as deaerated. However, the corresponding current values recorded during the test period are very different. When the solution was aerated, the current values were in the nA range and when deaerated the values were in the mA range. One explanation for this increase in current is the absence or decrease in the passive film formed on the surface of the alloy therefore exposing more metal to the electrolyte.

During polarization, the potential of the solution is measured relative to the test sample by placing a reference electrode in the test solution and connecting the two via a voltmeter. When a positive current is applied to the test sample, electrons are removed from the metal and as a result metal ions are free to go into solution. Thus, the more metal ions in solution the more positive the solution becomes relative to the metal. If the only electron sink in the process is on the auxiliary electrode connected to the potentiostat, the corresponding current will be directly proportional to the amount of dissolution. However, if some electrons are consumed in the reduction of oxygen on the sample (working electrode), a smaller current value can be applied to achieve the same amount of dissolution. This is thought to be the case when solution 4 is aerated.

When samples polarized in solution 5 were compared to those polarized in solution 4, the amount of anodic dissolution was much less for both the aerated and deaerated cases. This is thought to be a result of the passive film which forms due to the reduction of ferric ions. If the film is a poor electrical conductor both electron and metal ion diffusion will be impeded. This helps explain the reason why the current values for the aerated case are the same as the values for the deaerated case. If electron diffusion through the passive file is hindered, the reduction of oxygen can no longer occur and therefore a higher current value is required to achieve the same amount of anodic dissolution. In addition to electrons, if the diffusion of the metal ions is also impeded, a much higher current value is required to “drive” the ions into solution. However, a more in depth study is required to verify this hypothesis.

7.0 Summary

Figure 45 shows a plot of the pitting potentials obtained using the potentiodynamic polarization technique as well as the values obtained using the potentiostatic technique.

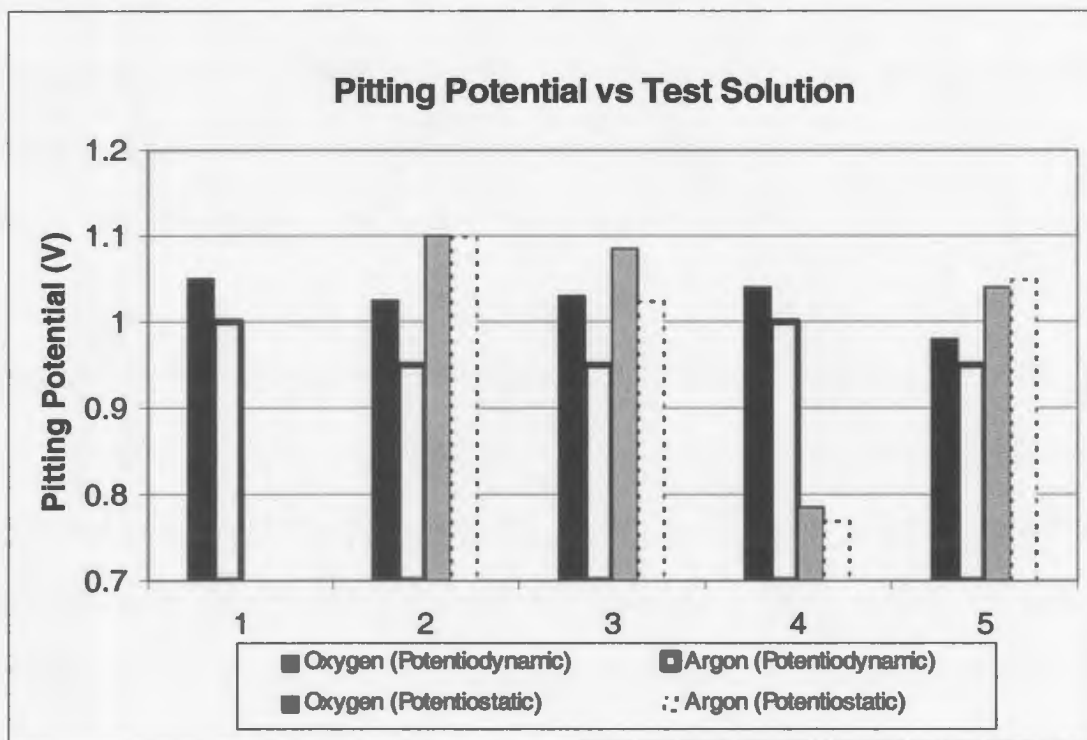


Figure 45. Pitting potentials as a function of test solution for potentiodynamic and potentiostatic polarization tests

The most notable difference in the pitting potentials are associated with solutions 3 and 4 which contain chloride ions. Using the potentiodynamic method the values increased with chloride ion concentration, however when potentiostatic methods were used the pitting potential decreased substantially as is expected. When ferric ions were added to the electrolyte, the pitting potential increased which is also expected based on the current

literature. The difference in the two curves also decreased with potentiostatic method, indicating aeration has little effect of the pitting potential for the given tests. However, the measured current values associated with the different tests varied with aeration. For deaerated solutions, all current values associated with polarization were in the mA range except for solution 2 which yielded current values in the nA range. For the aerated solutions all current values measured were in the nA range except for solution 5 which yielded values in the mA range. The only consistency with respect to the current range was associated with solution 5, which yields nearly identical results independent of aeration consistent with the findings of Uhlig and Geary [61].

With regard to the actual surface, solutions 2 and 3 yielded nearly identical results when aerated and deaerated, the only difference is that small irregular pits were located near the edge of the sample polarized using solution 3. Solution 4 produced the largest pits for both methods of aeration with an average width-to-depth ratio of about 6. The main difference between the samples polarized in the aerated solutions and those polarized in deaerated solutions is the surface between individual pits. For the deaerated solutions, the surface appeared unaffected where as the samples polarized in aerated solutions, the surface suffered from uniform grain etching. Solution 2, 3 and 4 showed an increased in localized etching near the sample/washer interface as the applied potential was lowered below the pitting potential for both aerated and deaerated solutions. However, the localized etching associated with samples polarized in deaerated solutions was more

severe than the solutions polarized in the aerated solutions. Refer to Appendix H for pictures of localized etching.

When samples were polarized in solution 5, the pits produced on the surface decreased in size and were irregular in shape as compared with pits on samples polarized in solution 4. In addition to pits, orange deposits (iron oxide) were distributed over the entire surface and increased in density as the potential was lowered toward the pitting potential. Below the pitting potential the density of the deposits began to decrease. One explanation for this is that the deposits on the surface developed into stable growing pits at higher applied potentials. No localized etching of any kind was associated with the samples polarized in solution 5.

8.0 Conclusions

Based on the results obtained from the current research, the following conclusions can be made.

1. Potentiostatic polarization techniques provide more accurate values of the pitting potential in comparison to potentiodynamic polarization techniques. The technique also provides information about the nucleation time for specific potential values. In addition, the pitting potentials obtained using potentiostatic polarization can be validated by analyzing the surface of the sample after each polarization test.
2. Cross-sectional analysis of the pitted surface show developed pits are not hemispherical in shape, but rather develop into a saucer shape or shallow spherical cup. For the current work, the average width-to-depth ratio for stable growing pits was found to be about 6.
3. From the surface analysis, it was confirmed that etched pits develop at lower applied potentials closer to the true pitting potential of the metal/electrolyte combination whereas highly polished pits developed when the applied potential was above the pitting potential.

4. Additions of Fe^{3+} to the electrolyte greatly reduced the localized attack on the surface of the test sample due the formation of a protective metal oxide as a result of the reduction reaction of Fe^{3+} to Fe^{2+} .

5. From the SEM micrographs it was confirmed that pits grow by undermining the passive film which served as a diffusion barrier ensuring the critical concentration of aggressive ions is maintained promoting stable pit growth. The nature of the film formed over the developing pits depends on the constituents of the bulk electrolyte.

References

1. E. Garcia, M. A. Hernandez, F. J. Rodriguez, J. Genesca and F. J. Boerio, "Oscillation and Chaos in Pitting Corrosion of Steel", *Corrosion*, **59**, 50-57 (2003).
2. S. Gray, K. Berriche-Bouhanek, H. E. Evans, "Oxide Growth in an Austenitic Stainless Steel Determined by Creep Extension", *Materials Science Forum*, **461-464**, 755-762 (2004).
3. Yoshimori Miyata, Takao Handa, Hisayoshi Takazawa, "An Analysis of Current Fluctuations during Passive Film Breakdown and Repassivation in Stainless Steel", *Corrosion Sci.*, **31**, 465-470 (1990).
4. P. Marcus, J. Oudar (editors), Corrosion Mechanisms in Theory and Practice, Marcel Dekker Inc., New York (1995).
5. E. E. Stansbury, R. A. Buchanan, Fundamentals of Electrochemical Corrosion, ASM International, Metals Park, Ohio (2000).
6. T. J. Hakkarainen, "Use of Artificial Pits to Investigate Conditions for the Growth and Repassivation of Open Macroscopic Corrosion Pits in Stainless Steel", *Materials Science Forum*, **289-292**, 955-968 (1998).
7. Rokuro Nishimura, Kiyokatsu Kudo, "The Effects of Passive Films Formed on Iron, Nickel and Austenitic Stainless Steels (SUS 304 and SUS 316) on Pitting Corrosion", *Corrosion Sci.*, **31**, 479-484 (1990).
8. Rokuro Nishimura, "The Effect of Chloride Ions on Stress Corrosion Cracking of type 304 and type 316 Austenitic Stainless Steels in Sulfuric Acid Solution", *Corrosion Sci.*, **34**, 1859-1868 (1993).
9. P. E. Manning, D.J. Duquette, W. F. Savage, "The Role of Sulfide Inclusion morphology in Pit Initiation of Several Type 300 Series Stainless Steels", *Corrosion*, **36**, 313-319 (1980).
10. G. Riedel, C. Voigt, H. Werner, K. P. Erkel, M. Gunzel, "The Influence of Acid Soluble Sulfide Inclusions on the Passivation Behavior of Austenitic Cr-Ni Stainless Steel", *Corrosion Sci.*, **27**, 533-544 (1987).

11. G. T. Burstein, S.P. Vines, "Repetitive Nucleation of Corrosion Pits on Stainless and the Effects of Surface Roughness", *J. Electrochem. Soc.*, **148**, B504-B516 (2001).
12. David E. Williams, Ying Yang Zhu, "Explanation for Initiation of Pitting Corrosion of Stainless Steel at Sulfide Inclusions", *J. Electrochem. Soc.*, **147**, 1763-1766 (2000).
13. J. O. Park, S. Matsch, H. Bohni, "Effects of Temperature and Chloride Concentration of Pit Initiation and Early Pit Growth of Stainless Steel", *J. Electrochem. Soc.*, **149**, B34-B39 (2002).
14. M. Kamrunnihar, R. D. Braatz, R. C. Alkire, "Parameter Sensitivity Analysis of Pit Initiation at Single Sulfide Inclusions in Stainless Steel", *J. Electrochem. Soc.*, **151**, B90-B97 (2004).
15. H. P. Hong, "Application of the Stochastic Process to Pitting Corrosion", *Corrosion*, **55**, 10-16 (1999).
16. A. Petek, V. Dolecek, V. Vlachy, "Stochastic Analysis of Current Fluctuations during General Corrosion of Stainless Steel in Sulfuric Acid", *Corrosion*, **53**, 928-934 (1997).
17. I. L. Rosenfeld, I. S. Danilov, "Electrochemical Aspects of Pitting Corrosion", *Corrosion Sci.*, **7**, 129-142 (1967).
18. R. K. Dayal, N. Parvathavarthini, J. B. Gnanamoorthy, "A Study of Various Critical Pitting Potentials for Type 316 Stainless Steel in Sulfuric Acid Containing Chloride Ions", *Corrosion*, **36**, 433-436 (1980).
19. G. Wranglen, "Pitting and Sulfide Inclusions in Steel", *Corrosion Sci.*, **14**, 331-349 (1974).
20. T. P. Hoar, D. C. Mears, G. P. Rothwell, "The Relationship Between Anodic Passivity, Brightening and Pitting", *Corrosion Sci.*, **5**, 275-289 (1965).
21. P. C. Pistorius, G. T. Burstein, "Metastable Pitting Corrosion of Stainless Steel and the Transition to Stability", *Phil. Trans. Royal Soc. London*, **341**, 531-559 (1992).
22. J. O. Park, T. Suter, H. Bohni, "Role of Manganese Sulfide Inclusions on Pit Initiation of Super Austenitic Stainless Steel", *Corrosion*, **59**, 59-66 (2003).

23. H. P. Leckie, H. H. Uhlig, "Environmental Factors Affecting the Critical Potential for Pitting in 18-8 Stainless Steel", *J. Electrochem. Soc.*, **113**, 1262-1267 (1966).
24. M. H. Moayed, R. C. Newman, "Using Pit Solution Chemistry for Evaluation of Metastable Pitting Stability of Austenitic Stainless Steel", *Materials and Corrosion*, **56**, 166-173 (2005).
25. W. Schwenk, "Theory of Stainless Steel Pitting", *Corrosion*, **20**, 129t-137t (1964).
26. R. W. Bosch, W. F. Bogaerts, J. H. Zheng, "Simple and Robust External Reference Electrodes for High-Temperature Electrochemical Measurements", *Corrosion*, **59**, 162-171 (2003).
27. G. T. Burstein, P. C. Pistorius, "Surface Roughness and the Metastable Pitting of Stainless Steel in Chloride Solutions", *Corrosion*, **51**, 380-385 (1995).
28. Toshio Shibata, Osamu Yamazaki, Shinji Fujimoto, "Two-Stage HNO₃ Passivation Treatment for Improving the Pitting Corrosion of Type 304 Stainless Steel", *Corrosion Engineering*, **48**, 209-219 (1999).
29. P. C. Pistorius, G. T. Burstein, "Aspects of the Effects of Electrolyte Composition on the Occurrence of Metastable Pitting on Stainless Steel", *Corrosion Sci.*, **36**, 525-538 (1994).
30. J. Mankowski, Z. Szklarska-Smialowska, "Studies on Accumulation of Chloride Ions in Pits Growing During Anodic Polarization", *Corrosion Science*, **15**, 493-501 (1975).
31. H. S. Isaacs, G. Kissel, "Surface Preparation and Pit Propagation in Stainless Steel", *J. Electrochem. Soc.*, **119**, 1628-1631 (1972).
32. J. L. Dawson, M. G. S. Ferreira, "Electrochemical Studies of the Pitting of Austenitic Stainless Steel", *Corrosion Sci.*, **26**, 1009-1026 (1986).
33. Yu Zuo, Haiou Du, Jinping Xiong, "Statistical Characteristics of Metastable Pitting of 316 Stainless Steel", *J. Mater. Sci. Technol.*, **16**, 286-290 (2000).
34. Norio Sato, "The Stability of Pitting Dissolution of Metals in Aqueous Solution", *J. Electrochem. Soc.*, **129**, 260-264 (1982).
35. Jose R. Galvele, "Transport Process and the Mechanism of Pitting of Metals", *J. Electrochem. Soc.*, **123**, 464-474 (1976).

36. H. Yashiro, K. Tanno, "The effect of Electrolyte Composition on the Pitting and Repassivation Behavior of AISI 304 Stainless Steel at High Temperature", *Corrosion Sci.*, **31**, 485-490 (1990).
37. Z. Szklarska-Smialowska, M. Janik-Czachor, "The Analysis of Electrochemical Methods for the Determination of Characteristic Potentials on Pitting Corrosion", *Corrosion Sci.*, **11**, 901-904 (1971).
38. N. J. Laycock, M. H. Moayed, R. C. Newman, "Metastable Pitting and the Critical Pitting Temperature" *J. Electrochem. Soc.*, **145**, 2622-2628 (1998).
39. Koichiro Osozawa, "The Effects of Nitrogen on the Passivity and the Pitting Corrosion of Stainless Steel", *Corrosion Engineering*, **47**, 629-643 (1998).
40. V. Vignal, J. M. Olive, D. Desjardins, "Effects of Molybdenum on Passivity of Stainless Steels in Chloride Media Using Ex Situ Near Field Microscopy Observations", *Corrosion Sci.*, **41**, 869-884 (1999).
41. Samuel A. Bradford, Corrosion Control, Van Nostrand Reinhold, New York (1993).
42. A. Ben Rhouma, C. Braham, M. E. Fitzpatrick, J. Ledion, H. Sidhom, "Effects of Surface Preparation on Pitting Resistance, Residual Stress, and Stress Corrosion Cracking in Austenitic Stainless Steel", *J. of Materials Engineering and Performance*, **10**, 507-514 (2001).
43. Martin Kraub, Ralf Herzog, Berthold Scholtes, "Influence of Surface Treatment on the Pitting Corrosion Behavior of High Alloyed Stainless Steels in a Chloride Solution", *Zeitschrift Metallkund*, **92**, 910-915 (2001)
44. R. F. A. Jargelius-Pettersson, B. Pires Duarte, G. Duchamp, "Pitting Corrosion in Austenitic and Duplex Stainless Steels", *Materials Science Forum*, **289-292**, 1029-1039 (1998).
45. Kiskeya Iida, Masayoshi Ohshima, "The Influence on Corrosion with Residual Stress and transformation Induced in Shot-Peened Austenitic Stainless Steel" *The 7th International Conference on Shot Peening*, Warsaw, Poland 192-198 (1999).
46. T. Suter, E. G. Webb, H. Bohni, R. C. Alkire, "Pit Initiation on Stainless Steels in 1 M NaCl With and Without Mechanical Stress", *J. Electrochem Soc.*, **148**, B174-B185 (2001).

47. Toshio Shibata, Osamu Yamazaki, Shinji Fujimoto, "The Effect of F⁻ in HNO₃ Passivation Treatment on Improving the Pitting Resistance of Type 304 Stainless Steel", *Corrosion Engineering*, **48**, 63-72 (1999).
48. E. S. Lee, "Machining Characteristics of the Electropolishing of Stainless Steel (STS 316L)", *International Journal of Advanced Manufacturing Technology*, **16**, 314-321 (2000).
49. Shuo-Jen Lee, Jain-Jang Lai, "The Effects of Electropolishing Process Parameters on Corrosion Resistance of 316L Stainless Steel", *Journal of Materials Processing Technology*, **140**, 206 (2003).
50. J. Stewart, D. E. Williams, "The Initiation of Pitting Corrosion on Austenitic Stainless Steel: On the Role and Importance of Sulfide Inclusions", *Corrosion Sci.*, **33**, 457-474 (1992).
51. J. R. W. Warn, Concise Chemical Thermodynamics, Van Nostrand Reinhold, London, UK (1969).
52. P. Q. Zhang, J. X. Wu, W. Q. Zhang, X. Y. Lu, K. Wang, "A Pitting Mechanism for Passive 304 Stainless Steel in Sulfuric Acid Media Containing Chloride Ions", *Corrosion Sci.*, **34**, 1343-1354 (1993).
53. A. M. Al-Mayouf, A. K. Al-Ameery, A. A. Al-Suhybani, "Inhibition of Type 304 Stainless Steel Corrosion in 2 M Sulfuric Acid by Some Benzoazoles-Time and Temperature Effects", *Corrosion*, **57**, 614-620 (2001).
54. H. Yashiro, K. Tanno, S. Koshiyama, K. Akashi, "Critical Pitting Potentials for Type 304 Stainless Steel in High-Temperature Chloride Solutions", *Corrosion*, **52**, 109-114 (1996).
55. G. Ruijini, S. C. Srivastava, M. B. Ives, "Pitting Corrosion Behavior of UNS N08904 Stainless Steel in a Chloride/Sulfate Solution", *Corrosion*, **45**, 874-882 (1989).
56. H. P. Leckie, "A Contribution to the Applicability of Critical Pitting Potentials", *J. Electrochem. Soc.*, **117**, 1152-1153 (1970).
57. R. C. Newman, "Pitting of Stainless Alloys in Sulfate Solutions Containing Thiosulfate Ions", *Corrosion*, **41**, 450-453 (1985).
58. A. Rossi, R. Tulifero, B. Elsener, "Surface Analytical and Electrochemical Study on the Role of Adsorbed Chloride Ions in Corrosion of Stainless Steel", *Materials and Corrosion*, **52**, 175-180 (2001).

59. Harry C. Gatos, "Acceleration of the Dissolution of Iron in Sulfuric Acid by Ferric Ions", *J. Electrochem. Soc.*, **103**, 286-291 (1956).
60. Joseph R. Cobb, Herbert H. Uhlig, "Resistance of Titanium to Sulfuric and Hydrochloric Acids Inhibited by Ferric and Cupric Ions", *J. Electrochem. Soc.*, **99**, 13-15 (1952).
61. Herbert H. Uhlig, Arthur Geary, "Potential of Iron, 18-8 and Titanium in passivating Solutions", *J. Electrochem. Soc.*, **101**, 215-223 (1954).
62. Michael A. Streicher, "Corrosion of Stainless Steels in Boiling Acids and its Suppression by Ferric Salts", *Corrosion*, **14**, 19-30 (1958).
63. J. R. Davis, (editor) *Stainless Steels*, "ASM Specialty Handbook", ASM International, Metals Park, Ohio (1994).
64. N. Alonso-Falleiros, A. Hakim, S. Wolyneec, "Comparison Between Potentiodynamic and Potentiostatic Tests for Pitting Potential Measurement of Duplex Stainless Steels", *Corrosion*, **55**, 443-448 (1999).
65. D. Pulino-Sagradi, N. Alonso-Falleiros, "The Effects of Small Amounts of Elements on Shapes of Potentiodynamic and Potentiostatic Curves of AISI 304 L and 316 L Stainless Steels in Chloride Media", *Braz. J. Chem. Eng.*, **14**, 1-12 (1997).
66. R. Winston Revie, (editor) *Uhlig's Corrosion Handbook, 2nd edition*, John Wiley & Sons Inc., New York (2000).
67. M. P. Ryan, N. J. Laycock, R. C. Newman, H. S. Isaacs, "The Pitting Behavior of Iron-Chromium Thin Film Alloys in Hydrochloric Acid", *J. Electrochem. Soc.*, **145**, 1566-1570 (1998).
68. E. Bardal, *Corrosion and Protection*, Springer-Verlag, London Ltd., (2004).

Appendix A

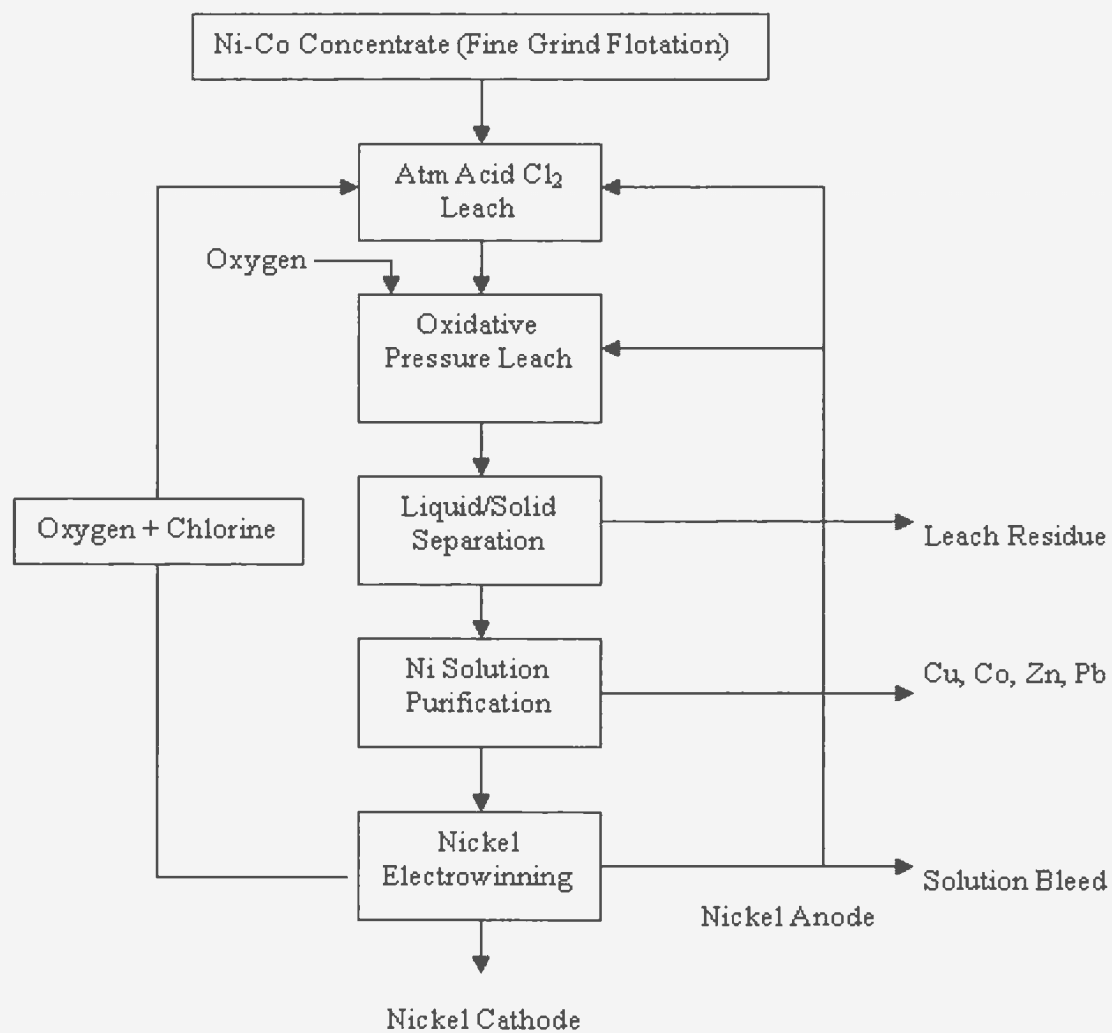


Figure 46. Proposed extraction process

Appendix B



Figure 47. Oxide penetration-90 minute Anneal

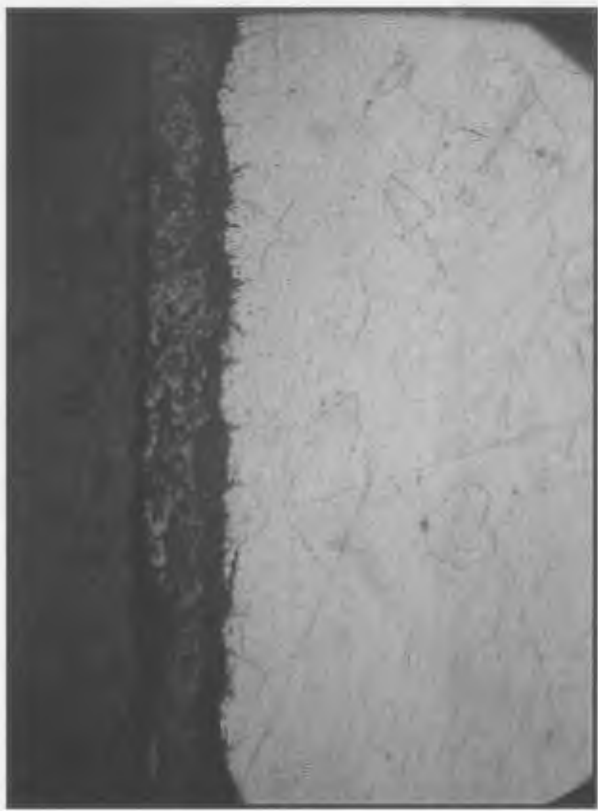


Figure 48. Oxide penetration-120 minute Anneal

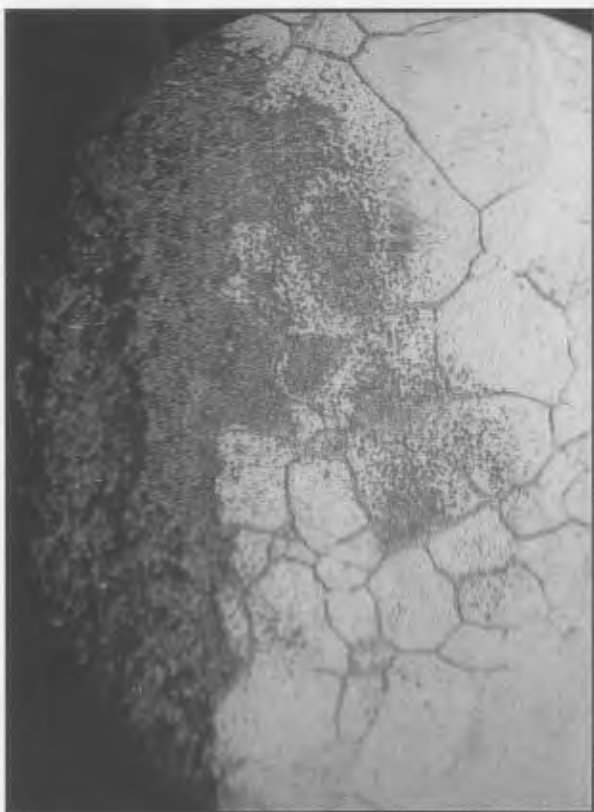


Figure 49. Oxide penetration-180 minute Anneal

Appendix C

Table 18. Test Solution ion concentration (g/L)

Ion	Ion Conc. (g/L)	Mass of Compound (g)	
		Ferric Sulfate	
Ferric	30	7.31	
0 g/L Chloride			
		Nickel Sulfate	Nickel Chloride
Nickel	20	4.478	0
10 g/L Chloride			
		Nickel Sulfate	Nickel Chloride
Nickel	20	2.624	1.676
20g/L Chloride			
		Nickel Sulfate	Nickel Chloride
Nickel	20	0.771	3.352

Table 19. Specific compound mixtures for Test Solution 1

Electrolyte	Solution 1
Batch Number	4
Mass of Nickel Sulfate (g)	0.0
Mass of Nickel Chloride (g)	0.0
Mass of Water (g)	200
Mass of Acid (g)	11.21
Total Mass (g)	211.21
% Acid	10.00

Table 20. Specific compound mixtures for Test Solution 2

Electrolyte	Solution 2
Batch Number	12
Mass of Nickel Sulfate (g)	53.736
Mass of Nickel Chloride (g)	0.000
Mass of Water (g)	600.000
Mass of Acid (g)	72.551
Total Mass (g)	726.287
% Acid	10.00

Table 21. Specific compound mixtures for Test Solution 3

Electrolyte	Solution 3
Batch Number	10
Mass of Nickel Sulfate (g)	26.244
Mass of Nickel Chloride (g)	16.762
Mass of Water (g)	500.000
Mass of Acid (g)	60.300
Total Mass (g)	603.307
% Acid	10.00

Table 22. Specific compound mixtures for Test Solution 4

Electrolyte	Solution 4
Batch Number	15
Mass of Nickel Sulfate (g)	11.565
Mass of Nickel Chloride (g)	50.287
Mass of Water (g)	750.000
Mass of Acid (g)	90.203
Total Mass (g)	902.055
% Acid	10.00

Table 23. Specific compound mixtures for Test Solution 5

Electrolyte	Solution 5
Batch Number	15
Mass of Nickel Sulfate (g)	11.565
Mass of Nickel Chloride (g)	50.287
Mass of Ferric Sulfate (g)	109.592
Mass of Water (g)	750.000
Mass of Acid (g)	101.572
Total Mass	1023.016
% Acid	10.00

Table 24. Micro-hardness values for potentiodynamic polarization tests

Oxygen				
Solution	d1	d2	d Average	Hardness (VHN)
1	41.50	42.00	41.75	213
2	44.00	44.50	44.25	190
3	41.75	42.75	42.25	208
4	42.000	42.500	42.25	208.00
5	41.750	42.000	41.88	211.00

Argon				
Solution	d1	d2	d Average	Hardness (VHN)
1	42.75	41.00	41.88	211
2	41.00	42.00	41.50	215
3	42.00	42.00	42.00	210
4	42.500	41.500	42.00	210
5	41.000	41.750	41.38	216

Table 25. Micro-hardness values for potentiostatic polarization tests – Solution 2

Oxygen						
Run #	Potential (V)	Time (s)	d1	d2	d Average	Hardness (VHN)
1	1.2	7200	43.75	42.75	43.25	198.5
2	1.15	7200	43.5	43.5	43.5	196
3	1.12	7200	42.25	42.75	42.5	212
4	1.1	7200	42.75	43.5	43.125	200
5	1.075	7200	43.75	43.25	43.5	196

Argon						
Run #	Potential (V)	Time (s)	d1	d2	d Average	Hardness (VHN)
1	1.15	7200	42.5	42.75	42.625	204
2	1.125	7200	42.00	42.00	42	210
3	1.1	7200	42.50	42.50	42.5	212
4	1.05	7200	42.75	43	42.875	201

Table 26. Micro hardness values for potentiostatic polarization tests – Solution 3

Oxygen						
Run #	Potential (V)	Time (s)	d1	d2	d Average	Hardness (VHN)
1	1.2	7200	41	42	41.5	215
2	1.1	7200	42	42	42	210
3	1.1	7200	42.00	42.50	42.25	208
4	1	7200	42.50	42.75	42.625	204

Argon						
Run #	Potential (V)	Time (s)	d1	d2	d Average	Hardness (VHN)
1	1.125	7200	42.75	42.00	42.375	206
2	1.1	7200	41.5	41	41.25	218
3	1.075	7200	42	42.75	42.375	197
4	1.05	7200	43	42.5	42.75	202

Table 27. Micro hardness values for potentiostatic polarization tests – Solution 4

Oxygen						
Run #	Potential (V)	Time (s)	d1	d2	d Average	Hardness (VHN)
1	1	7200	41.50	42.00	41.75	212
2	0.95	7200	42.5	42.75	42.625	204
3	0.9	7200	42.50	42.25	42.38	206
4	0.8	7200	42.5	42	42.25	208
5	0.7	7200	41.5	41.75	41.625	214
6	0.6	7200	43	42.25	42.63	204

Argon						
Run #	Potential (V)	Time (s)	d1	d2	d Average	Hardness (VHN)
1	1.1	7200	42.5	42	42.25	208
2	1	7200	42.50	42.25	42.375	206
3	1	7200	43.00	43.50	43.25	198
4	0.9	7200	41.5	42	41.75	212
5	0.8	7200	41.5	42	41.75	212
6	0.7	7200	41.75	41.5	41.625	214

Table 28. Micro hardness values for potentiostatic polarization tests – Solution 5

Oxygen						
Run #	Potential (V)	Time (s)	d1	d2	d Average	Hardness (VHN)
1	1.15	7200	42.5	42.25	42.375	206
2	1.1	7200	42.25	42.50	42.375	206
3	1.05	7200	41.75	42.00	41.875	211
4	1	7200	42	41.75	41.875	211
5	0.8	7200	42.25	42	42.125	208
6	0.6	7200	41.25	41	41.125	219

Argon						
Run #	Potential (V)	Time (s)	d1	d2	d Average	Hardness (VHN)
1	1.15	7200	41.75	41.5	41.625	214
2	1.1	7200	42.50	43.00	42.75	202
3	1.05	7200	41.00	41.50	41.25	217
4	0.95	7200	41	41.75	41.375	216
5	0.9	7200	41.5	41.75	41.625	214
6	0.7	7200	42	41.75	41.875	211

Appendix D



Figure 50. Test Cell

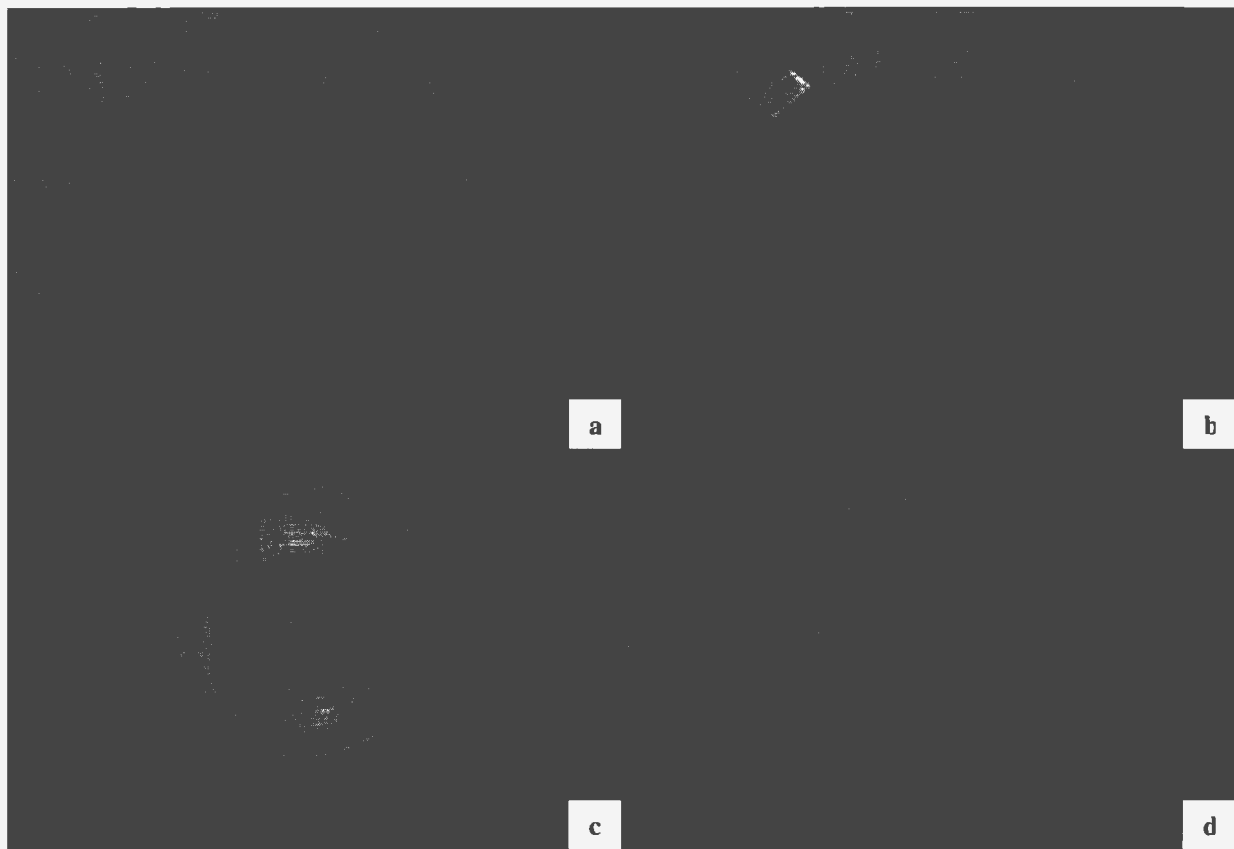


Figure 51. Pictures of Test Cell (a) Cover (b) Top view of Holder showing Pd auxiliary electrode (c) Stainless Steel Base (d) Bottom view of Holder showing removable sealing washer

Appendix E

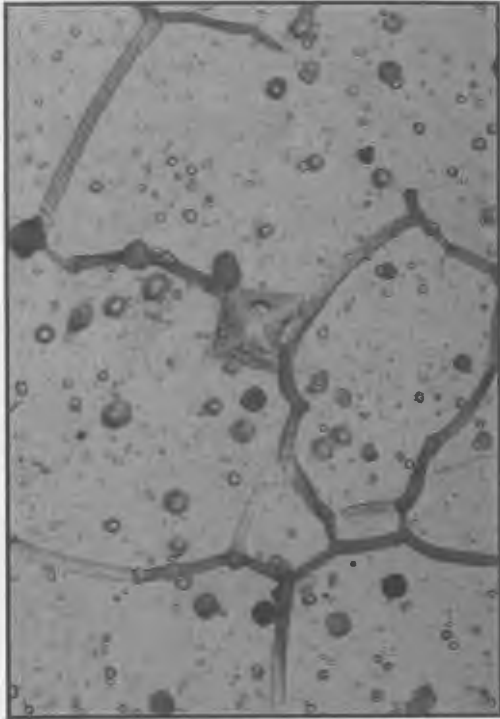


Figure 52. Type A Pits

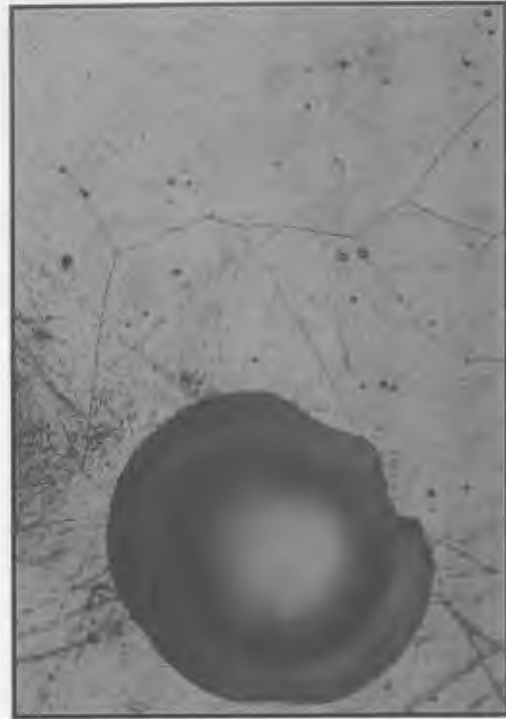


Figure 53. Type B Pits

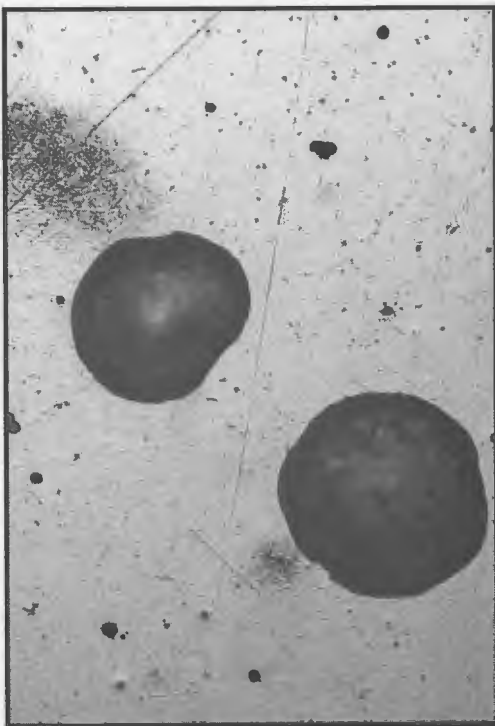


Figure 54. Type C Pits

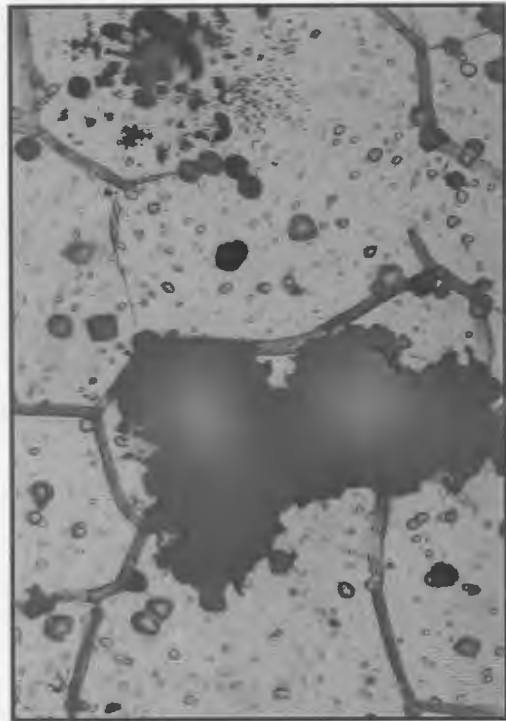


Figure 55. Type D Pits



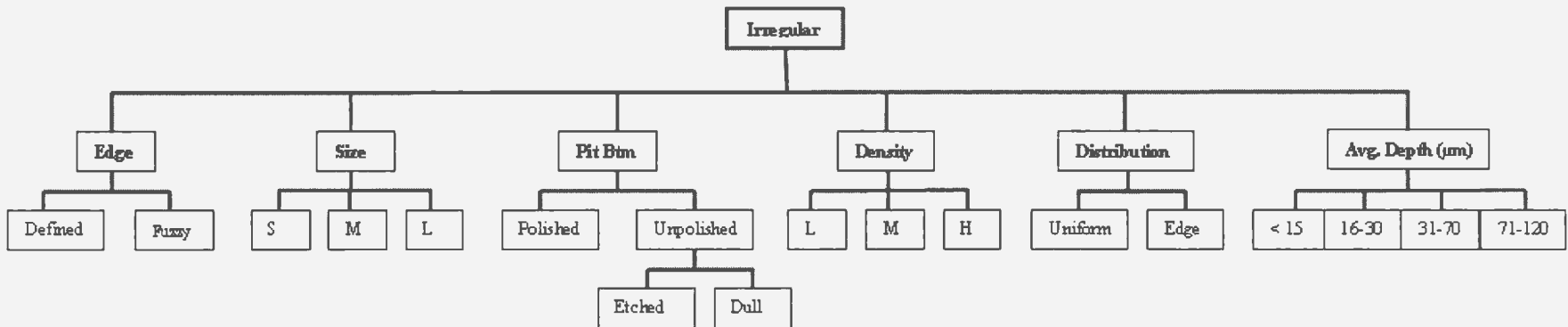
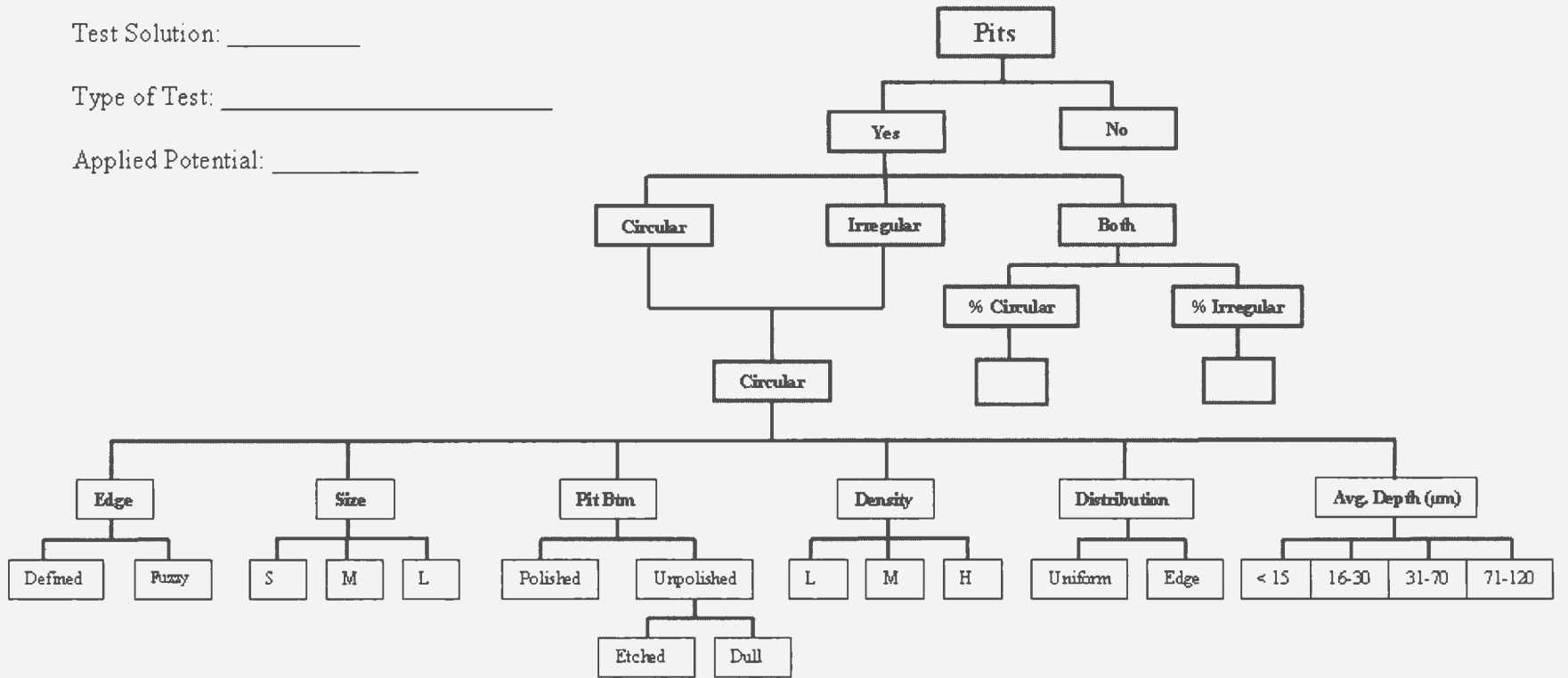
Figure 56. Type E Pits

Appendix F

Test Solution: _____

Type of Test: _____

Applied Potential: _____



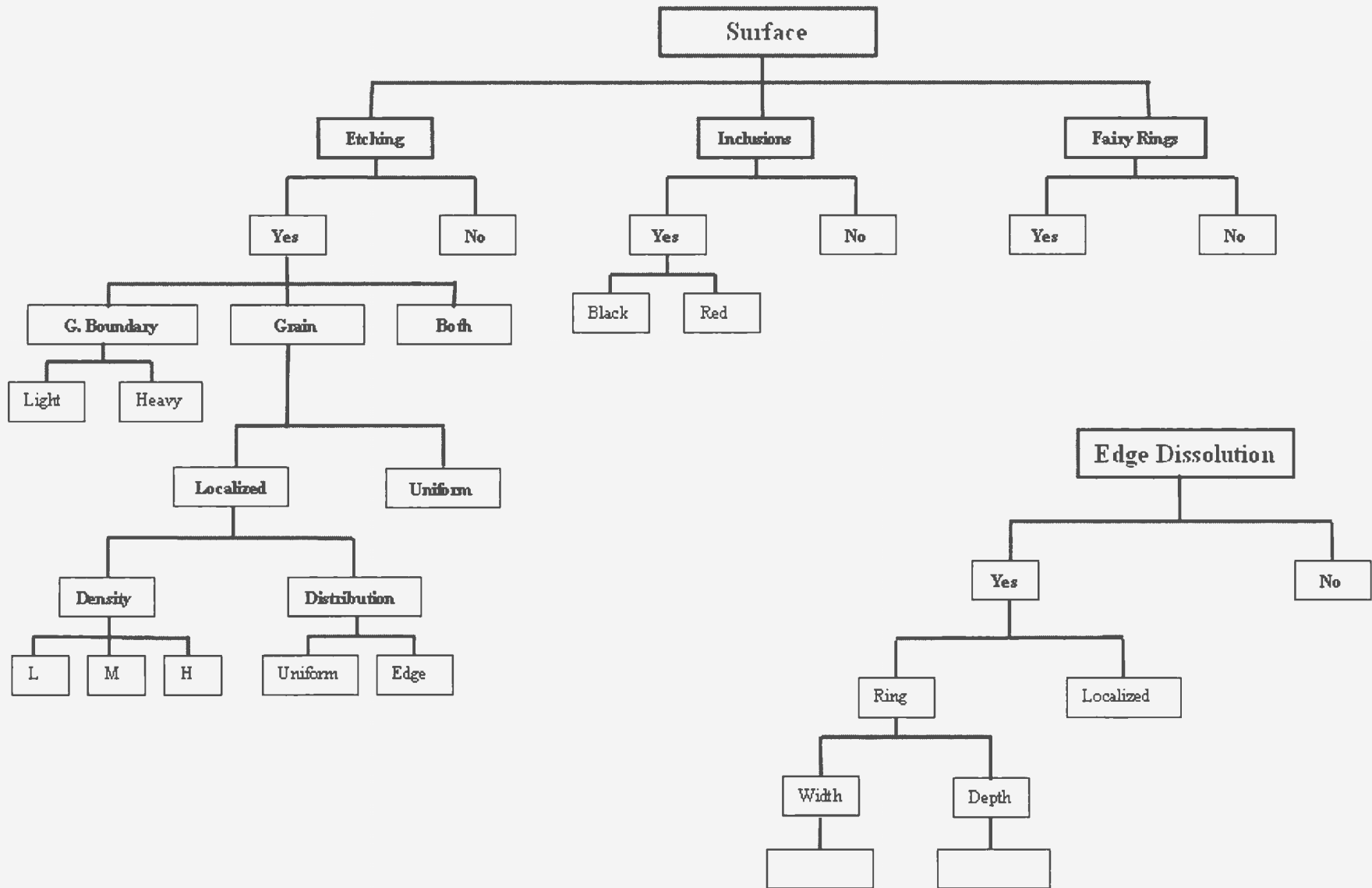


Figure 57. Classification Tree

Appendix G

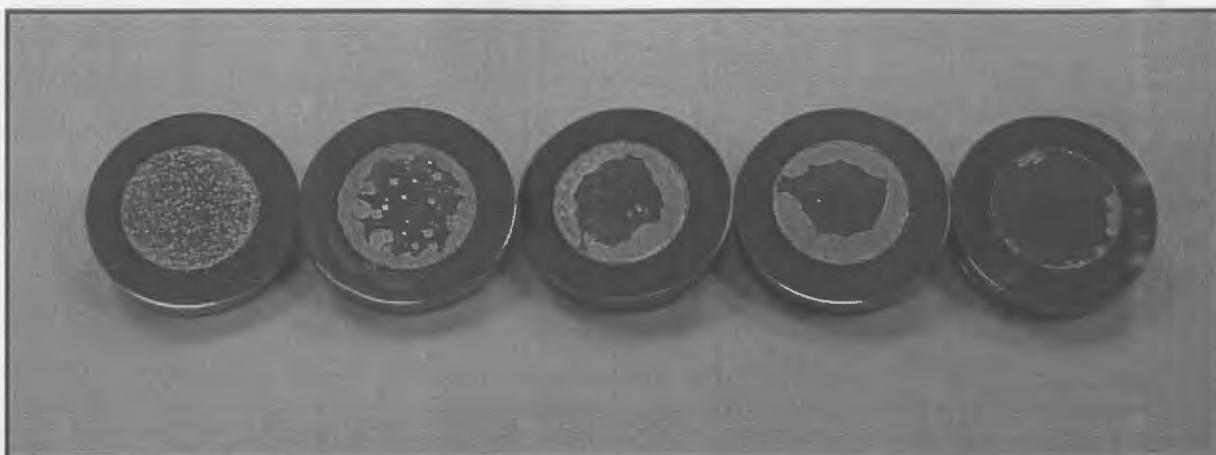


Figure 58. Pictures of samples potentiostatically polarized using Test Solution 4 (deaerated). From L-R, 1.1 V, 1.0 V, 0.9 V, 0.8 V and 0.7 V respectively



Figure 59. Pictures of samples potentiostatically polarized using Test Solution 4 (aerated). From L-R, 0.95 V, 0.9 V, 0.8 V, 0.7 V and 0.6 V respectively



Figure 60. Pictures of samples potentiostatically polarized. From L-R, Test Solution 4-Deaerated (0.9V) Aerated (0.9V), Test Solution 5 Deaerated (0.9V), Aerated (1.0V) respectively

Appendix H

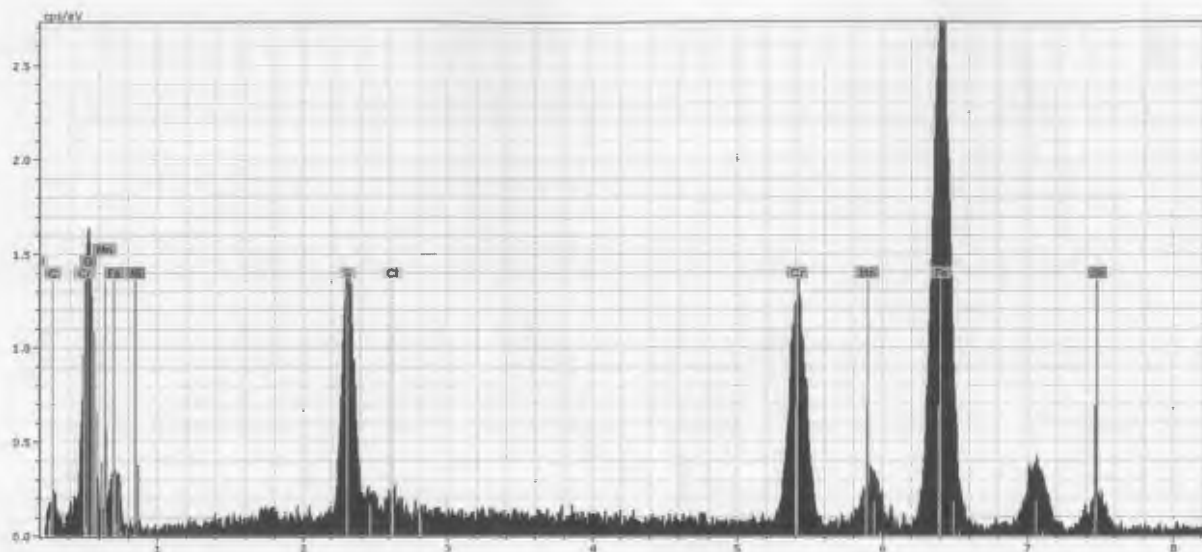


Figure 61. EDS Spectra of a sample polarized in Solution 5-Aerated-0.6V

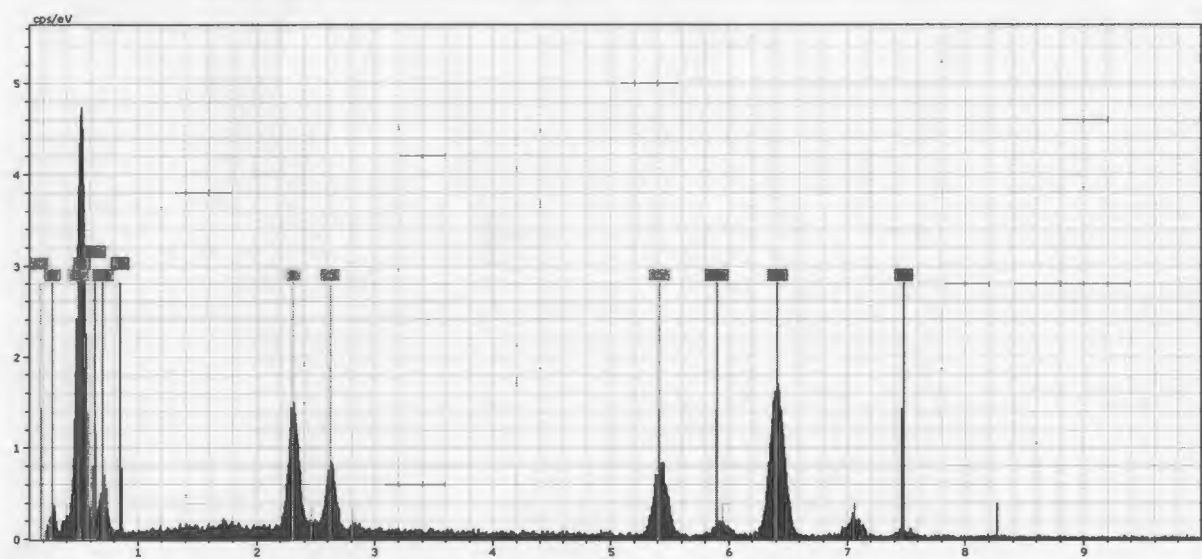


Figure 62. EDS Spectra of a sample polarized in Solution 5-Aerated-1.05V-1-A

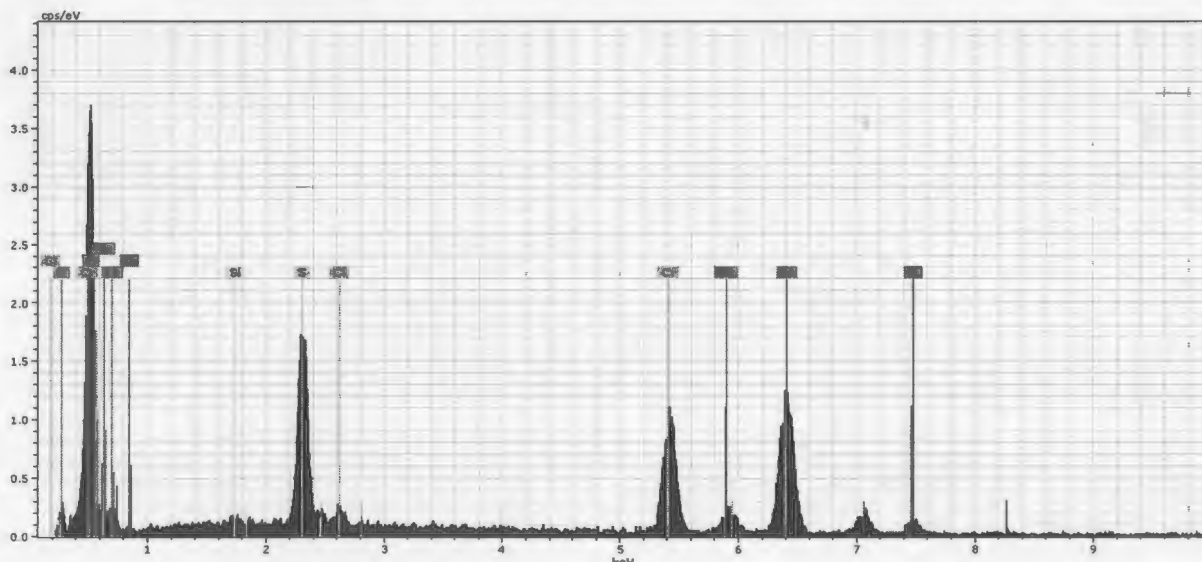


Figure 63. EDS Spectra of a sample polarized in Solution 5-Aerated-1.05V-1-B

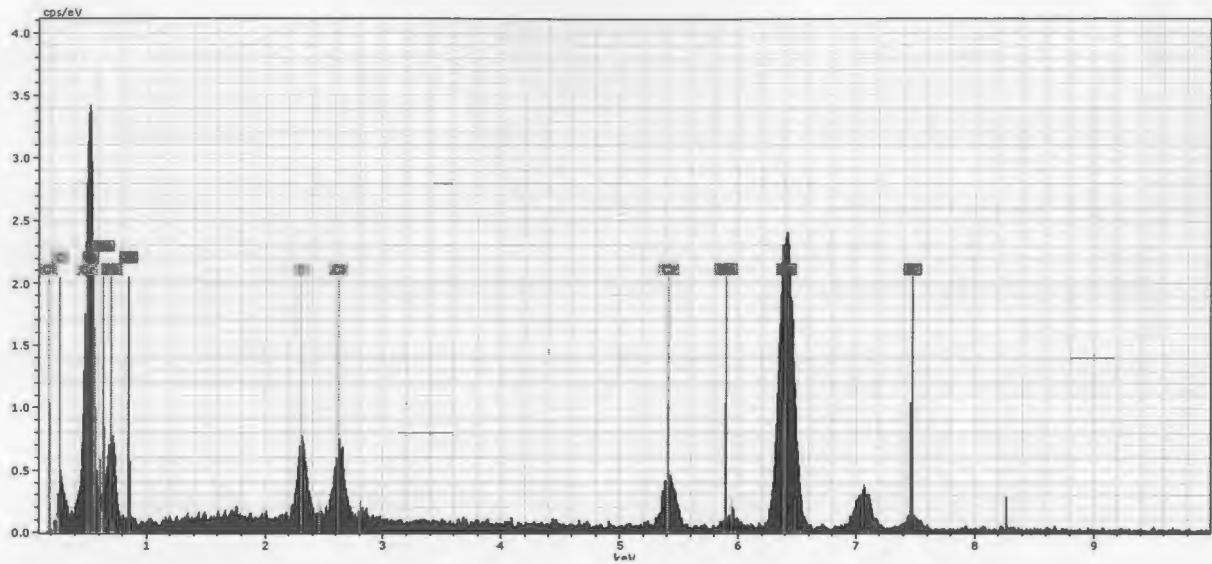


Figure 64. EDS Spectra of a sample polarized in Solution 5-Aerated-1.05V-2-A

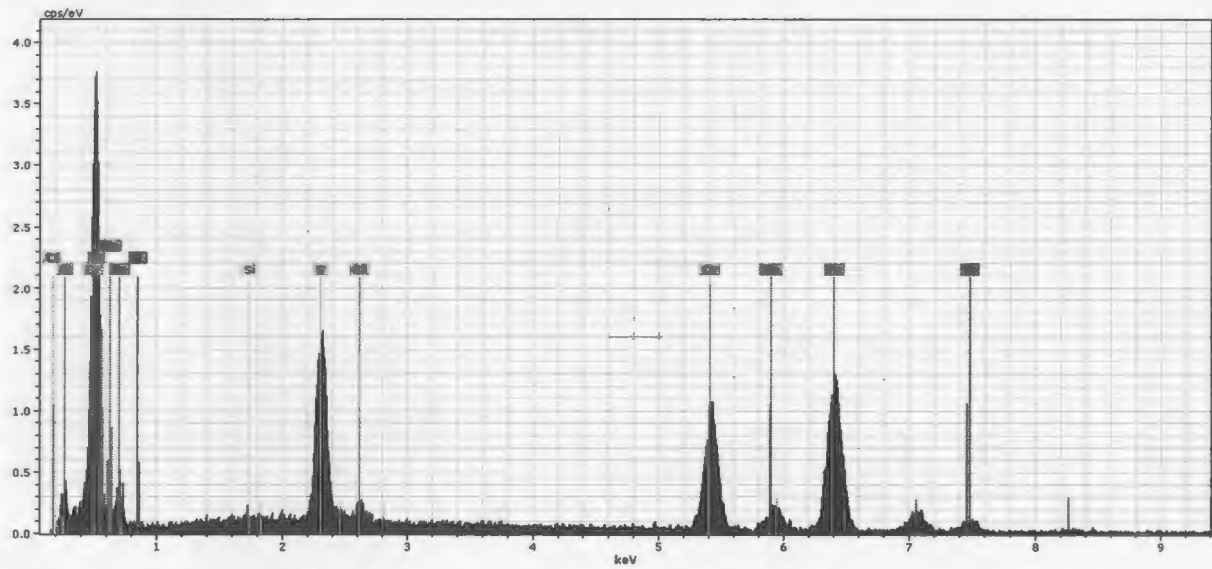


Figure 65. EDS Spectra of a sample polarized in Solution 5-Aerated-1.05V-2-B

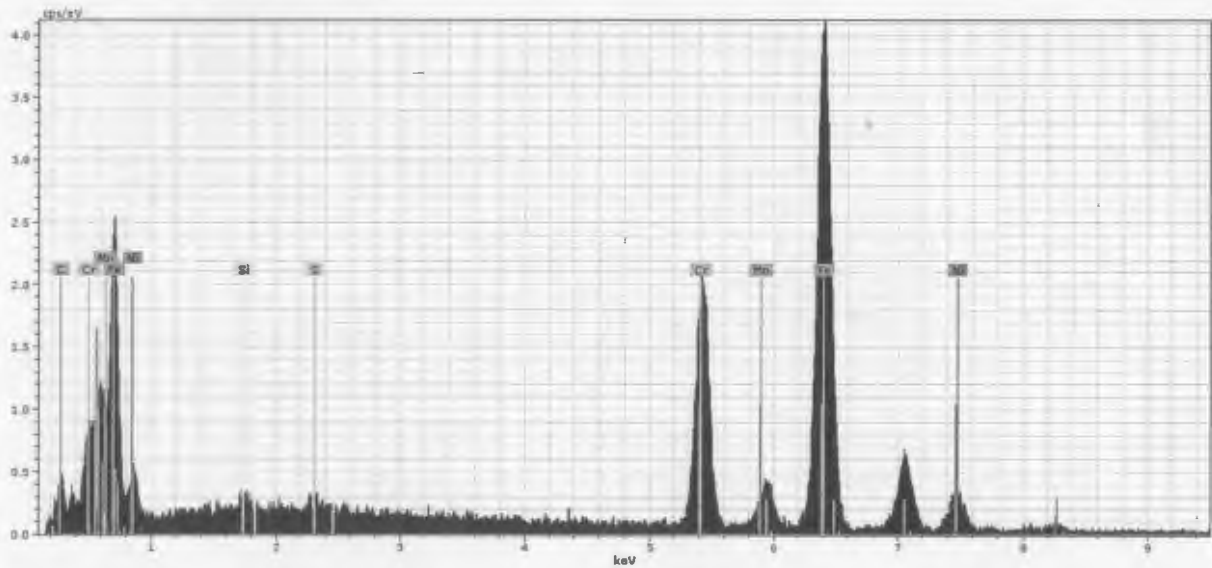


Figure 66. EDS Spectra of a sample polarized in Solution 4-Aerated-0.95V-1-A

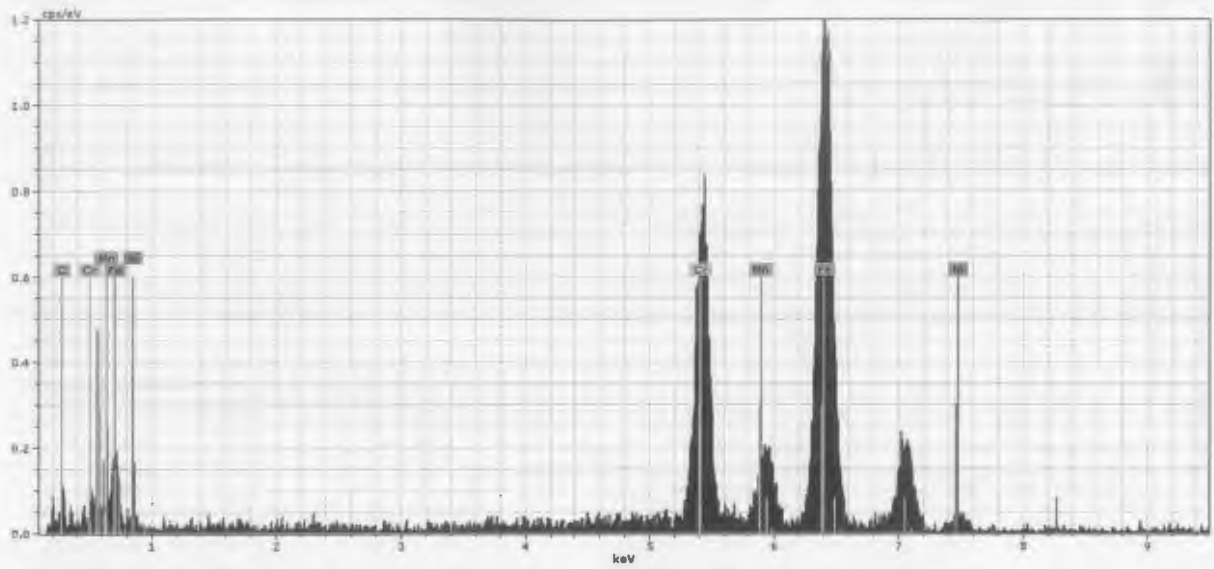


Figure 67. EDS Spectra of a sample polarized in Solution 4-Aerated-0.95V-1-B

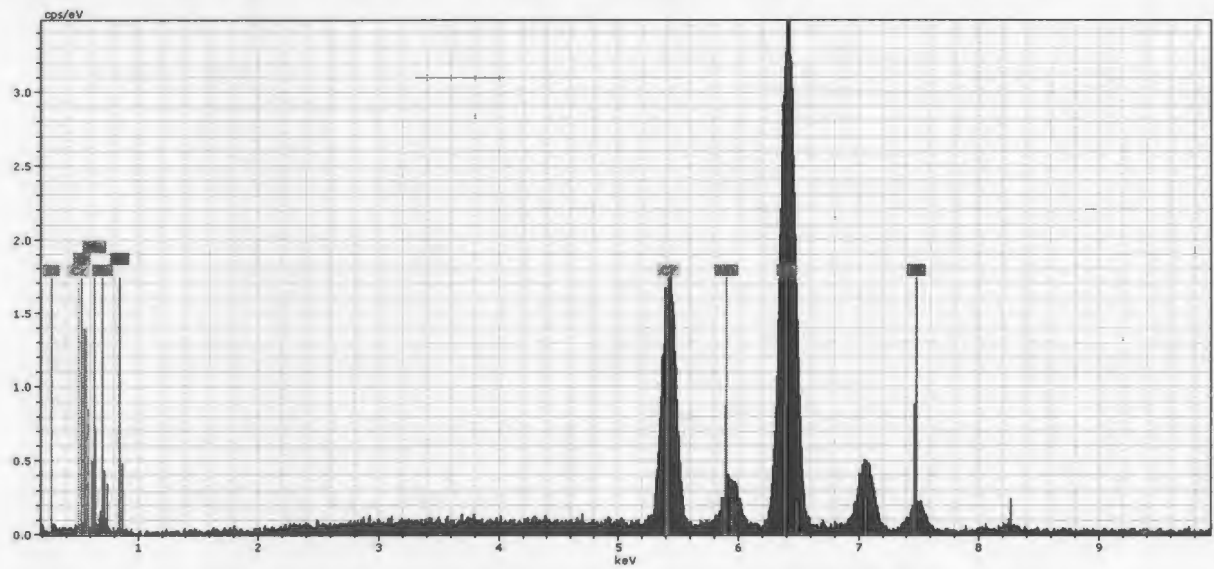


Figure 68. EDS Spectra of a sample polarized in Solution 4-Aerated-0.95V-2-A

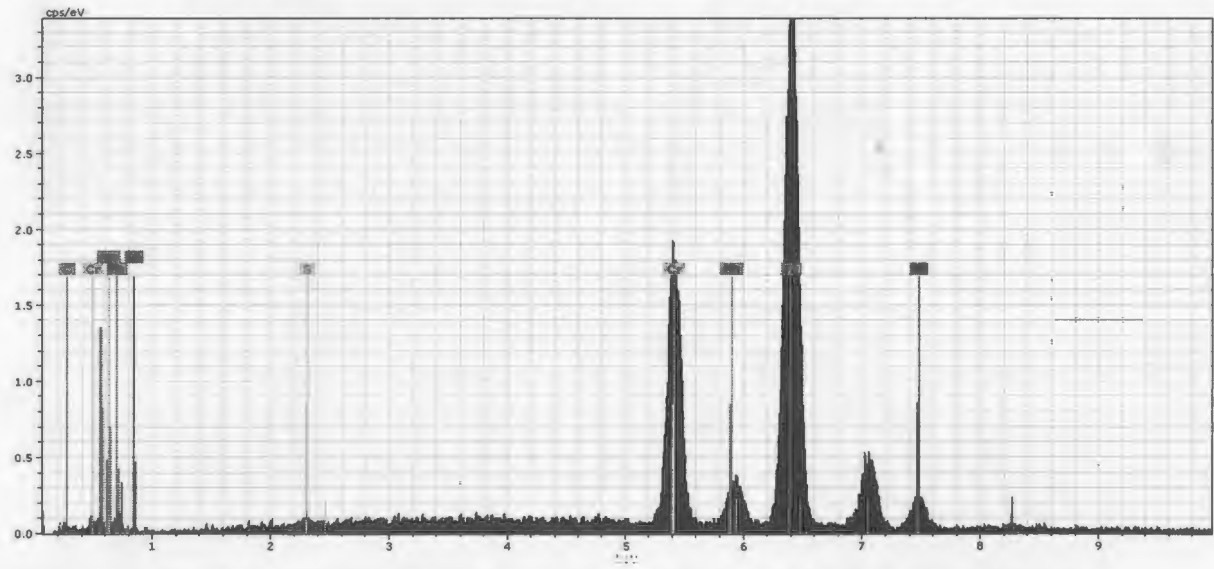


Figure 69. EDS Spectra of a sample polarized in Solution 4-Deaerated-1.1V-2-A

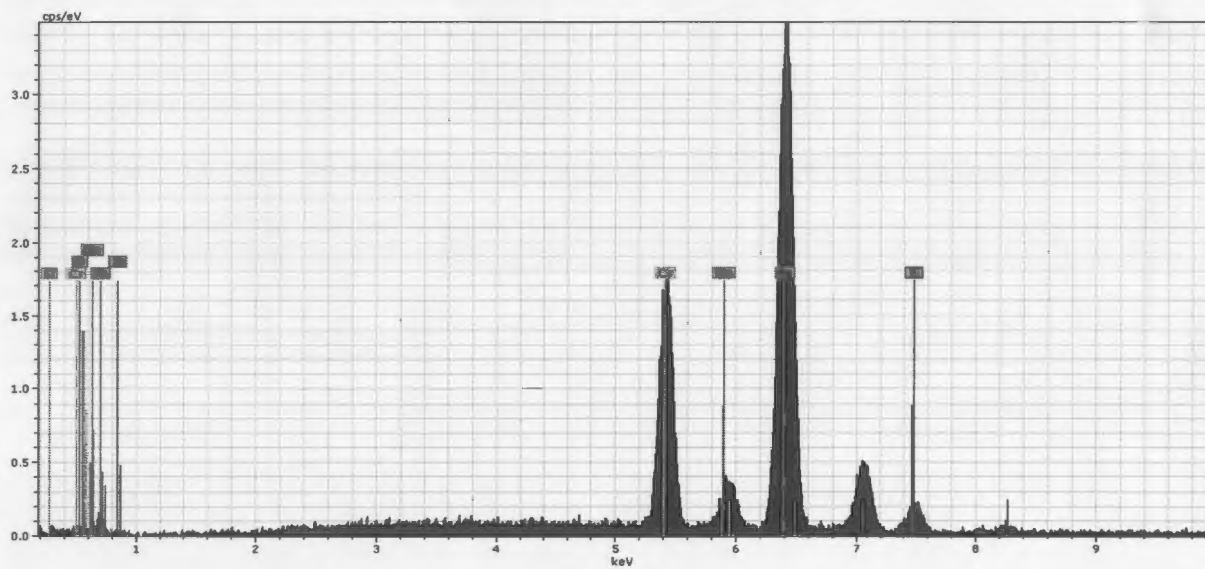


Figure 70. EDS Spectra of Stock 1-A

Appendix I

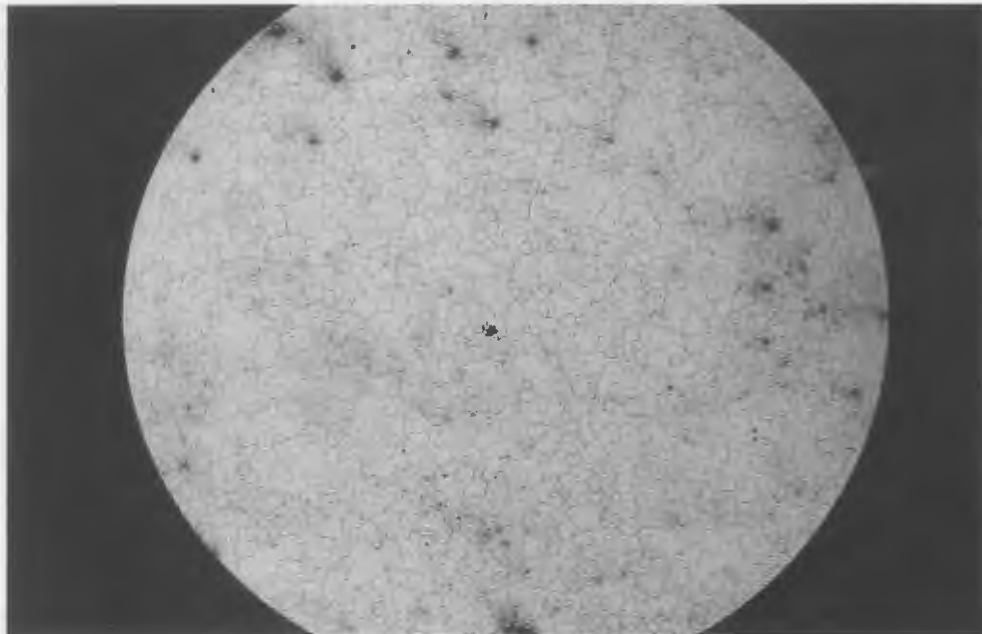


Figure 71. Localized Etching – Center

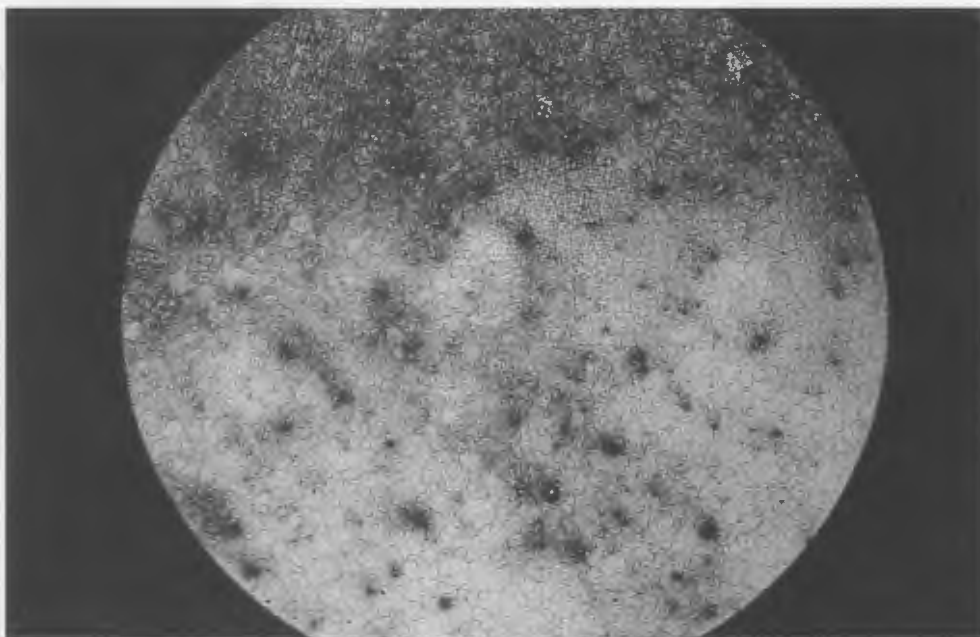


Figure 72. Localized Etching – Edge

